

FIRST-PRINCIPLES THEORETICAL STUDY OF LATTICE THERMAL CONDUCTIVITY OF
CRYSTALS AND EARTH MINERALS AT HIGH TEMPERATURES AND PRESSURES.

Moses Chou Ntam

A Dissertation

Submitted to

the Graduate Faculty of

Auburn University

in Partial Fulfillment of the

Requirements for the

Degree of

Doctor of Philosophy

Auburn, Alabama
August 4, 2012

DISSERTATION ABSTRACT

FIRST-PRINCIPLES THEORETICAL STUDY OF LATTICE THERMAL CONDUCTIVITY OF
CRYSTALS AND EARTH MINERALS AT HIGH TEMPERATURES AND PRESSURES.

Moses Chou Ntam

Doctor of Philosophy, August 4, 2012

173 Typed Pages

Directed by Jianjun Dong

The focus of this dissertation is the first-principles calculation of lattice thermal conductivity, a non-equilibrium thermal transport property, for a wide range of solid materials including both ideal crystals and iron (Fe)-bearing mineral solid solutions at high temperatures and pressures. Our computational technique combines first-principles density functional theory (DFT), quantum scattering theory, and the Peirls-Boltzmann transport theory (PBTT) within the single mode excitation approximation (SMEA). Lifetimes of individual phonon modes have been directly evaluated over a wide range of temperature-pressure conditions, including those relevant to the Earth's deep interior, without any empirical extrapolation. Our first-principles calculated lattice thermal conductivity is directly derived from the lifetimes, group velocities, and heat capacities of individual phonon modes.

An important input of our computational technique is the DFT-predicted microscopic inter-atomic potentials. In this study, inter-atomic potentials of solid materials were calculated up to third order using an efficient real-space super cell finite displacement (RSSFD) algorithm that we developed recently. This computational technique has predictive

capability over the range of validity of the DFT calculated atomic energy and forces. The robustness of the predicted density dependence of harmonic force constants and third order lattice anharmonicity tensors governs the reliability of the derived pressure dependence of phonon lifetimes, group velocities and heat capacities. To study iron-bearing mineral solid solutions, the vibrational virtual crystal approximation (vVCA) was implemented to calculate the configurationally averaged harmonic force constant matrices.

The most computationally intensive step of our calculation involves the evaluation of phonon scattering rates due to third order lattice anharmonicity. We have optimized our algorithm for speed, efficiency and massive parallelization on supercomputers. Our algorithm has been successfully tested on our PRISM computer cluster, the dense memory cluster (DMC) of the Alabama super computer authority (ASA) and the Ranger super computer at the Texas super computer center. Based on group symmetry theory, we only directly evaluate the phonon scattering rates at the irreducible q-points in the first Brillouin zone and rest are reconstructed from symmetry. For now our computational technique can handle systems as large as 20-atoms per unit cell.

Our newly developed computational techniques have been successfully adopted to study the two most abundant lower mantle minerals: silicate perovskite $\text{Mg}_{(1-x)}\text{Fe}_x\text{SiO}_3$ (20-atoms per orthorhombic unit cell) with $x = 0$ and $x = 12.50\%$, and ferropericlase $\text{Mg}_{(1-x)}\text{Fe}_x\text{O}$ (2-atoms per face centered cubic unit cell) with $x = 0$ and $x = 12.50\%$, as well as corundum structured Al_2O_3 (10-atoms per rhombohedral unit cell).

Our calculation shows that the low frequency acoustic modes are more effective carriers of heat compared to the optical phonon modes. In MgO and $\text{Mg}_{(1-x)}\text{Fe}_x\text{O}$ the acoustic phonon modes are seen to account for nearly 95% of the overall lattice thermal conductivity. The effect of Fe-substitution on the thermal conductivity of Fe-free periclase has been discussed. Fe is observed to lower the thermal conductivity of ferropericlase by significantly reducing the phonon lifetimes of the effective heat carrying phonon modes. The behavior

of κ_{MgO} and κ_{MgSiO_3} have been studied. Both follow a T^{-1} dependence typical of insulating materials however, the pressure increase of κ_{MgSiO_3} is substantially weaker than κ_{MgO} . For example, the normalized thermal conductivity $\frac{\kappa}{\kappa_0}$ at 300 K from 0 to 135 GPa is seen to increase from 1 to 3 for MgSiO_3 , while the same value goes from 1 to 8 for MgO . Implications for heat flow in the Earth's lower mantle have been discussed.

ACKNOWLEDGMENTS

I would like to begin by acknowledging the blessings of health, strength and a sound mind from God without which this work would not be possible. I dedicate this dissertation to my parents Joseph Ntam (of blessed memory) and Comfort Ntam who never had any formal education but invested their lives in raising me and my seven siblings and laid a solid foundation which made it possible for me to reach this far in my academic journey.

I hereby express my profound gratitude to Prof. JJ. Dong, who supervised this work, for his time and dedication and for constantly giving me new challenges throughout this work. His understanding and flexibility in allowing me to maintain my own schedule is appreciated.

I am grateful for the following persons: Mr Philip Forrest (physics department IT-specialist) who maintained the PRISM computing cluster that enabled me to carry out most of the computations reported in this dissertation. I remember times when Phil had to work overnight and sometimes for days, to bring the computing cluster back online when there was an outage. Without his dedication and sacrifice, this work might not have been completed. Dr A.B. Chen who interviewed me and introduced me to the physics program at Auburn University, Dr J.D. Perez (Physics department chair) for his support, generosity, and encouragement throughout my studies at Auburn University, Dr Marlin Simon for advice on teaching and who was always available to share his wisdom on future faculty career related questions, Dr Chin-Che Tin my teaching supervisor while I taught Engineering Physics II, for all the useful discussions we had on teaching, Dr Hinata who supervised me while I taught general physics II for all the advice I received from him. Dr Overtoun Jenda (assistant provost for diversity and multi-cultural affairs), for professional advice and mentoring, Dr Florence Holland for useful discussions and career advice while I was pondering what to

do after my Ph.D degree. Dr Bin Xu and Dr Tang Xiaoli former members of our research group for useful research discussions. Dr Eddy Kwessi for useful discussions on latex which I used to typeset and compile this dissertation. Besides those mentioned here, I gratefully acknowledge the support and prayers from all my friends during the course of this work.

Special thanks to My siblings (Mary Ewei Buh, Magaret Ndum Kah, John Mai Ntam, Godlove Nji Ntam, Denis Beng Ntam, Elvis Cheghe Ntam and James Mueghe Ntam), for their affection, unconditional support and prayers from Cameroon throughout the duration of my graduate studies at Auburn University.

I am indebted to my secondary and high school physics teachers Mr Chetambong John and Mr Mbenga Isaac for inspiring me and laying a solid foundation that enabled me to pursue a career in physics.

Finally I would like to acknowledge financial support for my Ph.D research from the National Science Foundation (NSF grant # EAR 075784) and the teaching assistantship program of the Physics Department at Auburn University. I am most grateful to the physics department at AU for the opportunity to hone my teaching skills while serving as teaching assistant and instructor.

Style manual or journal used Bibliography follows Institute of Physics (IOP) style

Computer software used The document preparation package T_EX (specifically L^AT_EX)
together with the departmental style-file auphd.sty.

TABLE OF CONTENTS

Abstract	ii
Acknowledgments	v
List of Figures	x
List of Tables	xvii
List of Abbreviations	xix
1 INTRODUCTION	1
1.1 Lower Mantle Heat Flow	1
1.2 Lower Mantle Minerals	3
1.3 Lattice Thermal Conductivity of Lower Mantle Minerals	4
1.4 Challenges of Measuring κ at High Temperatures and Pressures	8
1.5 First-principles Calculations of Lattice Thermal Conductivity: Motivations and Recent Progress	9
1.6 Outline of Dissertation	13
2 FIRST-PRINCIPLES CALCULATION OF HARMONIC AND ANHARMONIC LATTICE DYNAMICS	14
2.1 Interatomic Potentials	14
2.2 Harmonic Lattice Dynamics	16
2.2.1 Harmonic Approximation	16
2.2.2 Second Quantization	20
2.3 Third Order Lattice Anharmonicity	22
2.4 Real Space Super Cell Calculation of Lattice Dynamics	24
2.5 Quasi-harmonic Approximation (QHA) and Mode Grüneisen Parameter	27
2.6 Vibrational Virtual Crystal Approximation(vVCA)	29
3 PEIRLS-BOLTZMANN TRANSPORT THEORY	31
3.1 Peierls-Boltzmann Transport Theory (PBTT)	31
3.2 Phonon Lifetime (τ): Fermi’s Golden Rule, Single Mode Excitation Approximation (SMEA), and Scattering Rates Due to Mass Disorder	34
3.3 Numerical Recipe for τ_{anh} Calculation	37
4 Lattice Thermal Conductivity of α -Al ₂ O ₃ Crystal	40
4.1 Introduction	40
4.2 Lattice Dynamics and Equilibrium Thermal Properties	41
4.2.1 Symmetry Analysis and First-principles Calculation of Total Energies	41
4.2.2 Quasi-harmonic Phonons	44
4.3 Phonon Lifetimes	50
4.4 Lattice Thermal Conductivity κ	51
4.5 Conclusion	55

5	LATTICE THERMAL CONDUCTIVITY OF PV-MgSiO ₃ AT LOWER MANTLE CONDITIONS	56
5.1	Introduction	56
5.2	First-principles Calculation of Total Energies, Vibrational Properties and Phonon Lifetimes	58
5.3	Results	59
5.3.1	Lattice Dynamics and Related Thermal Properties	59
5.3.2	Phonon Lifetimes	63
5.3.3	Pressure Dependence of Thermal Conductivity	64
5.4	Discussion	67
5.4.1	Comparison of the Behavior of κ_{MgO} and κ_{MgSiO_3}	67
5.5	Conclusions	68
6	LATTICE THERMAL CONDUCTIVITY OF FERROPERICLASE	70
6.1	Introduction	70
6.2	Static Equation of State	70
6.3	Vibrational Virtual Crystal Approximation of Lattice Dynamics of Ferroperricase	72
6.4	Phonon Lifetimes	74
6.5	Lattice Thermal Conductivity of fp-Mg _(1-x) Fe _x O	75
6.6	Conclusions	80
7	Implications for Heat Flow Across the Core-Mantle Boundary (CMB)	81
7.1	Introduction	81
7.2	Results	83
7.3	Discussion	91
7.4	Conclusions	92
8	CONCLUSIONS AND FUTURE WORK	94
	Appendices	109
A	Finite Difference Method For Harmonic Force Constants	110
A.1	Symmetry Analysis	110
A.2	Calculation of Harmonic Force Constants	111
B	Interpolation of Irreducible Inter-atomic Potentials (IIIP)	113
B.1	Introduction	113
B.2	Interpolation of Independent Force Constants	114
B.3	Volume Dependence of Harmonic Force Constants Φ_{ij}	115
C	Thermal Equation of State of Al ₂ O ₃	124
D	Equations of State (EOS) PV-MgSiO ₃ and Lattice Dynamics of PPV-MgSiO ₃	127
D.1	Static Equation of State	127
D.2	Thermal EOS of PV-MgSiO ₃	129
D.3	Lattice Dynamics of PPV-MgSiO ₃	131
E	Density Dependence of Phonon Lifetimes in PV-MgSiO ₃	134

LIST OF FIGURES

1.1	Isobaric κ_{latt} of MgO derived based on our LDA calculated thermal equation of state. Discrete symbols represent experimental measurements. Inset: Normalized κ_{latt} v.s. pressure. For the seven isotherms (300K, 500K, 1000K, 1500K, 2000K, 2500K, 3000K), κ_0 is the lattice thermal conductivity at 0 GPa. Our new calculation shows a slight improvement over the previously published results thanks to the optimization of our computational technique, for speed and accuracy.	12
2.1	Mode Grüneisen Parameter(γ_i) derived from harmonic force constant matrix and third order lattice anharmonicity tensor in MgO compared. Blue circles represent mode Grüneisen parameter (γ) from third order lattice anharmonicity tensor (A_{ijk}), orange circles represent γ from harmonic force constants matrix (φ_{ij}). Both γ s follow the same trend, showing that our calculated A_{ijk} are indeed reliable.	29
2.2	Vibrational Virtual Crystal Approximation (vVCA)	30
3.1	Energy and momentum conservation for 3-phonon processes	35
4.1	LDA calculated density dependent harmonic force constants of Al_2O_3 based on a 120-atom super cell model. A total of 1441 independent Φ_{ij} were extracted from the HF forces from VASP calculation. Majority of the Φ_{ij} terms are small and insensitive to volume change. Less than 20 inter-atomic force constants have magnitudes exceeding $5 \text{ eV}/\text{\AA}^2$ and show an almost linearly increasing pressure dependence with increasing pressure.	45
4.2	Vibrational phonon frequencies and density of states. Our LDA calculated phonon spectrum (solid lines) agree well with measurements from experiment (discrete symbols). Low frequency(acoustic) phonon modes have steeper slopes (group velocities) compared to the high frequency (optical) modes which are mostly flat.	46
4.3	Pressure dependence of anharmonicity tensor elements (A_{ijk}). A_{ijk} elements are observed to vary linearly with volume/density. From 0 GPa ($\sim 84 \text{ \AA}^3$) to 50 GPa ($\sim 75 \text{ \AA}^3$), A_{ijk} increases linearly from $40 \text{ eV}/\text{\AA}^3$ to $60 \text{ eV}/\text{\AA}^3$, representing a 50% increase, $\sim 1\%$ per GPa.	47

4.4	Mode Grüneisen Parameters calculated from the force constants matrix(blue circles) and from the third order anharmonicity tensors(orange circles) compared . We use this information to independently test the reliability of our calculated third order anharmonicity tensors. The extraction of Grüneisen Parameters from third order lattice anharmonicity is described in section 2.5	48
4.5	Volume dependence of mode heat capacity. Lines represent the heat capacity of individual phonon modes at the sampled at the irreducible K-points in Brillouin zone at 6 different densities/unit cell volumes.	49
4.6	Volume/density dependence of square of phonon mode group velocities. Vg^2 shows a mild volume dependence. Remember that according to kinetic transport theory, lattice thermal conductivity is given by ($\kappa = \frac{1}{3} \sum C_v v_g^2 \tau$)	49
4.7	Density Dependence of phonon lifetimes in α -Al ₂ O ₃ the at 300K (a) & (b) Transverse acoustic modes (c) Longitudinal acoustic phonon mode; (d)Optical phonon modes. Lifetimes of optical phonon modes are almost pressure insensitive. Acoustic modes increase almost linearly with decreasing volume (increasing pressure). The optical phonon mode with the longest lifetime is only about half the lifetime of the longest acoustic mode. This singles out acoustic phonons as the dominant carriers of heat in α -Al ₂ O ₃	50
4.8	Density dependence of mode- κ from acoustic phonon modes at T= 300K. Acoustic modes thermal conductivity follows a volume dependence identical to that of the acoustic modes phonon lifetimes shown in figure 4.7 a, b & c. This is expected as the other determining variables in the thermal conductivity equation C_v and V_g^2 , figures 4.5 and 4.6 are almost flat(volume insensitive)	51
4.9	Density dependence of mode- thermal conductivity from optical phonon modes at T= 300K. $\kappa_{optical}$ is almost pressure insensitive, consistent with the pressure dependence of $\tau_{optical}$, figure 4.7 d, and C_v and V_g^2 , (figures 4.5 and 4.6)	52
4.10	Density dependence of κ^{-1} . We have directly calculated the lattice thermal conductivity of α -Al ₂ O ₃ at six densities ranging from 3.98 gcc ⁻¹ to 4.51 gcc ⁻¹ and at 10 different temperature points from 300K to 2500K. κ^{-1} shows a linear temperature dependence at constant density. At constant temperature κ^{-1} increases almost linearly with increasing density.	52
4.11	Pressure dependence of isothermal κ . Based on the V(T,T) dependence from our LDA calculated thermal EOS we have derived the pressure dependence of κ . The numbers 1-6 represent the six unit cell volumes (densities) for which κ was calculated. κ isotherms show a linear pressure dependence. From this pressure dependence, we can derive the temperature dependence of isobaric κ shown in figure 4.12. From the labels 1-6 one can preview the temperature dependence of κ at conditions of constant pressure.	53
4.12	Isobaric κ of α -Al ₂ O ₃ at 0 GPa and 50 GPa. We show a comparison between our calculated thermal conductivity and experiment at 0GPa. Discrete symbols denote experiment data while solid continuous line represent our first-principles calculation.	53

4.13	Pressure dependence of κ . At 0 GPa, we predict nearly 3 %/GPa and 4.6 %/GPa increase in κ at 300 K and 2500K respectively.	54
5.1	Density dependence of harmonic force constants in PV-MgSiO ₃ . Independent force constants shown for 160-atom periodic supercells of PV.	59
5.2	LDA calculated phonon mode frequencies in PV-MgSiO ₃ and MgO at 0 GPa.	60
5.3	LDA calculated phonon mode frequencies in PV-MgSiO ₃ at 120 GPa	60
5.4	LDA calculated phonon mode group velocities in PV-MgSiO ₃ at four different densities shown. Group velocities measured along the Z-direction are more sensitive to pressure. From a density of 5.465 g/cm ³ (\sim 120 GPa) to 4.141g/cm ³ (\sim 0 GPa)the phonon group velocity in the Γ -Z direction decreases from around 15 km/s to 11 Km/s. Velocities measured in the other high symmetry directions X and Y are almost insensitive to pressure.	61
5.5	Density dependence of 3 rd order lattice anharmonicity tensor (A_{ijk}) elements in PV-MgSiO ₃ . Most A_{ijk} elements vary nearly linearly with volume/density. Most of the elements are very small.	61
5.6	Mode Grüneisin parameters in PV-MgSiO ₃ . Blue circles represent the Mode Grüneisin parameters calculated from the second order force constants while the orange circles show the same parameters calculated via our LDA calculated third order lattice anharmonicity tensors. This step is used to independently test the reliability of our lattice anharmonicity data since A_{ijk} is not known to have measured counterparts to which we can compare our calculated data.	62
5.7	Volume/density dependence of phonon lifetimes in PV-MgSiO ₃ all 60 modes at two high symmetry points: X ($\frac{\pi}{a}$, 0, 0) and Z (0, 0, $\frac{\pi}{c}$) in the Brillouin Zone	63
5.8	Temperature dependence of κ^{-1} in PV-MgSiO ₃ . κ is calculated at 4 distinct densities corresponding to unit cell volumes shown on the figure, at 9 different temperatures ranging from 300 K to 4000K, for a total of 36 density-temperature configurations. κ is seen to follow the T ⁻¹ dependence typical of lattice thermal conductivity in insulating materials.	64
5.9	Pressure dependence of κ^{-1} in PV-MgSiO ₃ at isothermal conditions. This is derived based on the P-V-T relations obtained from our LDA calculated thermal EOS.	65
5.10	Main: Temperature dependence of isobaric κ in PV-MgSiO ₃ . Inset: Pressure variation of normalized lattice thermal conductivity. Using the coefficients from $\kappa = a_0 + a_1P + a_2P^2$ the isobaric lattice thermal conductivity was derived. Four isobars 0, 50, 100 and 135 GPa are shown. Inset: Pressure variation of normalized κ . κ_0 represents the thermal conductivity at 0 GPa for each isotherm. From 300 K to 4000K, κ/κ_0 increases from 3 to 9 at 135 GPa.	66
6.1	Static EOS of ferropericlasite fitted to 3 rd order BM EOS	71

6.2	Phonon dispersion relations and mode group velocities in $\text{Mg}_{0.875}\text{Fe}_{0.125}\text{O}$ The black line/symbols shows the result obtained by replacing the mass of Mg in the MgO calculation by the weighted mass $\text{Mg}_{0.875}\text{Fe}_{0.125}$. The blue lines/symbols show the result obtained from the vVCA approach where the interatomic force constants are directly calculated as described in section 2.6. Fe substitution is seen to have the effect of softening phonon frequencies and mode group velocities.	73
6.3	Mode Grüneisen parameter	73
6.4	Volume/density dependence of phonon lifetimes of acoustic and optical phonon modes in fp as predicted by vVCA compared to corresponding modes in MgO. Panels under a) show the density dependence of the lifetimes for acoustic modes and b) shows the lifetimes of optical modes. The longest optical lifetime is nearly a factor of 10 lower than the longest acoustic mode, confirming the notion that acoustic modes are more effective heat transporters than the optical modes.	74
6.5	Thermal conductivity associated with anharmonicity	75
6.6	Temperature dependence of κ^{-1} in MgO. κ was calculated at 5 distinct densities corresponding to unit cell volumes shown on the figure, at 12 different temperatures ranging from 300 K to 3000K. Our calculated κ follows a T^{-1} dependence.	76
6.7	Temperature dependence of κ^{-1} in fp calculated at the corresponding unit cell volumes for the Fe-free MgO results presented in figure 6.6. κ does not quite follow the T^{-1} dependence seen in MgO.	77
6.8	Pressure dependence of isothermal κ in MgO derived from our LDA calculated thermal EOS. For each isotherm, we used our calculated thermal EOS to determine the pressure corresponding to the unit cell volumes 12, 13, 14, 16 & 18 \AA^3 labeled 1, 2, 3, 4 & 5 along the isotherms: 300 K - 3000 K. Only seven of the 12 isotherms are shown, for clarity. By fitting this to a second order polynomial in P ($\kappa = a_0 + a_1P + a_2P^2$) we used the coefficients a_0, a_1, a_2 from the 12 isotherms to predict κ at isobaric conditions.	78
6.9	Pressure dependence of κ at isothermal conditions in fp. This pressure dependence was derived using the same approach described under figure 6.8	78
6.10	Main: Temperature dependence of isobaric κ in MgO. Using the coefficients from $\kappa = a_0 + a_1P + a_2P^2$ we derived the isobaric thermal conductivity. Four isobars 0, 50, 100 and 150 GPa are shown. Inset: Pressure variation of normalized κ . κ_0 represents the thermal conductivity at 0 GPa for each isotherm. From 300 K to 3000K, κ/κ_0 increases from 8 to 25 at 135 GPa.	79
6.11	Main: Temperature dependence of isobaric κ in $\text{Mg}_{(1-x)}\text{Fe}_x\text{O}$; Inset: Pressure dependence of $\frac{\kappa}{\kappa_0}$ from 0GPa to 135 GPa. κ_0 is the thermal conductivity at 0GPa for each isotherm. From 300 K to 3000K, κ/κ_0 increases from 2.4 to 5 at 135 GPa. This is almost a factor of 5 lower than in MgO.	79

7.1	Vibrational phonon frequencies of $(\text{Mg}_{1-x}\text{Fe}_x)\text{O}$ (a) and $(\text{Mg}_{1-x}\text{Fe}_x)\text{SiO}_3$ -perovskite (b) with iron concentration $x=12.5\%$ at deep mantle pressure	84
7.2	Calculated lattice thermal conductivity for MgSiO_3 perovskite as a function of pressure and temperature. Calculations are shown for Fe-free crystal (translucent symbols and lines) and mineral solid solution including 12.5% Fe (bold color symbols and lines). Also plotted are experimental data from Osaka & Ito, 1991 on MgSiO_3 and from Manthilake et al., 2011 on $(\text{Mg,Fe})\text{SiO}_3$ at temperatures from 473 to 1073 K.	86
7.3	Isobaric thermal conductivity as a function of temperature. Computed lattice conductivity (solid purple line) and calculated contribution from radiative heat flow (red dashed and dotted lines, from optical absorption values provided by Goncharov et al., 2008 and Keppler et al., 2008 respectively, as a function of temperature at constant mid-mantle pressure of 80 GPa. The total thermal conductivity of perovskite is given by the sum of $\kappa_{rad} + \kappa_{latt}$ (purple dotted and dashed lines, corresponding to the two estimates for radiative contributions to the thermal conductivity)	87
7.4	Thermal conductivity calculated down a sample lower mantle geotherm (Jeanloz) and thermal boundary layer. Lattice thermal conductivity calculated from first principles estimates for MgO (solid blue line, Tang & Dong, 2010), and MgSiO_3 perovskite (solid purple line, this study). Thin red lines show calculated radiative contribution to thermal conductivity from two optical absorption estimates (dashed line: Goncharov et al., 2008;	88
7.5	A plot summarizing the observational tradeoffs used to determine the total heat flow across the core-mantle boundary (contoured, labels in terawatts). Commonly assumed values from Lay et al., 2008 for the thermal boundary thickness, the temperature at the bottom of the mantle, and the temperature at the top of the core are shown on the right axis. Vertical solid green lines delineate our newly-determined range of estimates for lower mantle thermal conductivity.	89
B.1	Volume dependence of one inter-atomic Force constant calculated using different finite atomic displacements ($\Delta = 0.02, 0.04, 0.06, 0.08$)Å	115
B.2	Discrete symbols represent directly calculated values of irreducible interatomic force constants, solid lines are the values of force constants predicted using the fitting parameters from the calculated values according to equation B.1. Predicted force constants coincide with those from direct calculation.	117
B.3	Main: The dominant irreducible harmonic force constants corresponding to inter-atomic forces $\Phi_{Ca^{+2}-Ca^{+2}}, \Phi_{O^{-2}-Ca^{+2}}, \Phi_{O^{-2}-O^{-2}}$. Inset: Minor inter-atomic force constants (IFC). The major inter-atomic force constants are clearly volume dependent implying that the associated phonon frequencies are volume dependent. The mode Grüneisen parameter gives the volume dependence according to QHA theory. Most minor IFCs are volume independent.	120

B.4	Volume dependence of Force constants in SrO. Discrete symbols in the main graph are force constants between Sr-Sr, O-Sr and O-O. The inset shows the density dependence of the remaining IFCs	121
B.5	Volume dependence of Force constants in MgO. Main: IFCs between Mg-Mg, O-Mg and O-O. Inset: Rest of the IFCs.	122
C.1	Main: Volume-pressure relationship in α -Alumina at five temperature points: 300K, 500K, 100K, 1500K, 2000K. Inset: Static EOS fitted to 3 rd order Birch Murnaghan EOS	125
C.2	Thermal EOS from first-principles theoretical calculation(LDA +PAW) compared with measurements. Discreet symbols represent measurements done by Wachtman et al., 1962; Schauer, 1965; Amatuni et al., 1976; Adelber & Traverse, 1984; Fiquet et al., 1999 and White & Roberts, 1983. Red solid line represents a reproduction of LDA+PAW calculation previously done by Bin Xu, 2009(former member of our research team)	126
D.1	Main: Static EOS of MgSiO ₃ fitted to 3 rd order Birch-Murnaghan EOS. Inset: Difference in enthalpies of PV and PPV phases plotted as a function of pressure. Our calculation predicts that at ambient temperature, the PV→PPV transition occurs at 101 GPa which is consistent other theoretical predictions for example Tsuchiya et al. (2004).	128
D.2	P-V-T isotherms in PV-MgSiO ₃ derived within the QHA. Solid lines represent our LDA calculation, dashed lines represent previous calculation by Oganov et al. (2000), circles denote Experimental measurement by Knittle et al. (1987)	130
D.3	Thermal EOS of PV-MgSiO ₃ derived within the QHA. Solid lines represent our LDA calculation, dashed lines represent previous calculation by Karki et al. (2000), Discrete symbols are experimental measurement by Wang et al. (1994)	130
D.4	Density dependence of harmonic force constants (eV/Å ²) in PPV-MgSiO ₃ . Independent force constants shown for 160-atom periodic supercells of PPV.	131
D.5	LDA calculated phonon mode frequencies in PPV-MgSiO ₃ at 118 GPa . . .	132
D.6	LDA calculated phonon mode group velocities in PPV-MgSiO ₃ at 118GPa. Mode group velocities in PPV are of the same order of magnitude as those in PV at corresponding pressure.	132
D.7	Density dependence of 3 rd order lattice anharmonicity tensor elements (eV/Å ³) in PPV-MgSiO ₃ . Most third order lattice anharmonicity tensors are insensitive to the change in volume/density. A few terms show a decreasing trend with compression.	133
E.1	Density dependence of phonon lifetimes for 60 phonon modes at irreducible K-points #1-6 in BZ	135
E.2	Density dependence of phonon lifetimes for 60 phonon modes at irreducible K-points #7-12 in BZ	136
E.3	Density dependence of phonon lifetimes for 60 phonon modes at irreducible K-points #13-18 in BZ	137

E.4	Density dependence of phonon lifetimes for 60 phonon modes at irreducible K-points #19-24 in BZ	138
E.5	Density dependence of phonon lifetimes for 60 phonon modes at irreducible K-points #25-30 in BZ	139
E.6	Density dependence of phonon lifetimes for 60 phonon modes at irreducible K-points #31-36 in BZ	140
E.7	Density dependence of phonon lifetimes for 60 phonon modes at irreducible K-points #37-42 in BZ	141
E.8	Density dependence of phonon lifetimes for 60 phonon modes at irreducible K-points #43-48 in BZ	142
E.9	Density dependence of phonon lifetimes for 60 phonon modes at irreducible K-points #49-54 in BZ	143
E.10	Density dependence of phonon lifetimes for 60 phonon modes at irreducible K-points #55-60 in BZ	144
E.11	Density dependence of phonon lifetimes for 60 phonon modes at irreducible K-points #61-66 in BZ	145
E.12	Density dependence of phonon lifetimes for 60 phonon modes at irreducible K-points #67-72 in BZ	146
E.13	Density dependence of phonon lifetimes for 60 phonon modes at irreducible K-points #73-78 in BZ	147
E.14	Density dependence of phonon lifetimes for 60 phonon modes at irreducible K-points #79-84 in BZ	148
E.15	Density dependence of phonon lifetimes for 60 phonon modes at irreducible K-points #85-90 in BZ	149
E.16	Density dependence of phonon lifetimes for 60 phonon modes at irreducible K-points #91-96 in BZ	150
E.17	Density dependence of phonon lifetimes for 60 phonon modes at irreducible K-points #97-100 in BZ	151

LIST OF TABLES

1.1	Layered structure of the Earth and composition	1
4.1	Space groups, formula units per primitive unit cell Z and Wyckoff sites of $\alpha\text{-Al}_2\text{O}_3$:	40
4.2	Irreducible atomic displacements (number of total energy calculations required), Independent and dependent Φ_{ij} and A_{ijk} terms from crystal symmetry.	42
4.3	Calculated lattice thermal conductivity fitted to second order in pressure at 10 different temperatures: $\kappa = a_0 + a_1P + a_2P^2$. The parameters a_0, a_1, a_2 are then used in conjunction with the calculated thermal EOS to predict the isobaric lattice thermal conductivity at different temperatures as shown in figure 4.12	54
5.1	Space groups, formula units per primitive unit cell Z and Wyckoff sites of 2 polymorphs of MgSiO_3 : perovskite and post-perovskite.	56
5.2	Irreducible representation of the mode symmetries at Γ -point for the 2 polymorphs of MgSiO_3 : perovskite and post-perovskite.	57
5.3	Simulation cell volumes and corresponding pressures for PV- MgSiO_3 calculation T=300 K.	59
6.1	Static Equation of state of fp- $\text{Mg}_{(1-x)}\text{Fe}_x\text{O}$	71
8.1	Contributions to overall κ_{latt} from acoustic and optical phonon modes in MgO , $\alpha\text{-Al}_2\text{O}_3$ and PV- MgSiO_3	95
B.1	Fitting parameters a_0, a_1, a_2, a_3 for the 52 independent harmonic force constants of MgO fitted to third order according to equation B.1. The original LDA calculated harmonic force constants were extracted based on a 128-atom supercell and a finite atomic displacement $\Delta = 0.04 \text{ \AA}$. $ii = (ia - 1) * Ns + idir$, $jj = (ja - 1) * Ns + jdir$. Where $(ia, ja) = 1$ to 128 and $Ns = 3$	123
C.1	Third-order BM-EOS parameters for $\alpha\text{-Al}_2\text{O}_3$	124
C.2	Gibbs Free energy (F_0), Volume per unit cell (V_0), Bulk modulus (B_0) and derivative of bulk modulus (B'_0) at 0 GPa	124
D.1	Static EOS parameters of MgSiO_3 PV and PPV fitted to 3 rd order BM EOS at ambient conditions	128
D.2	LDA calculated thermal EOS parameters for PV- MgSiO_3 at 0 GPa. Values in parentheses are from Tsuchiya et al. (2005)	129

E.1 Simulation cell volumes and corresponding pressures for PV-MgSiO₃ at 300 K. 134

LIST OF ABBREVIATIONS

BM	Birch-Murnaghan
BZ	Brillouin zone
CMB	Core-mantle boundary
cond	Conduction
conv	Convection
CPU	Central processing unit
DFT	Density functional theory
e.m	electromagnetic
EOS	Equation of State
f.c.c.	face centered cubic
GGA	Generalized gradient approximation
H-F	Hellmann-Feynman
IFC	Inter-atomic Force Constants
IIP	Interpolation of Irreducible Inter-atomic Potentials
IPAD	Irreducible paired atom displacement
ISAD	Irreducible single atom displacement

LD	lattice dynamics
LDA	Local density approximation
LM	Lower mantle
LO-TO	Longitudinal Optic-Transverse Optic
LTC	Lattice Thermal Conductivity
MD	molecular dynamics
NEMD	Non-equilibrium molecular dynamics
PAW	Plane augmented waves
PBTT	Peirels-Boltzmann Transport Theory
QHA	Quasi-harmonic approximation
rad	radiation, radiative
RSSF	Real space supercell finite displacement
RT	Relaxation time
RTA	Relaxation time approximation
SMEA	Single mode excitation approximation
TC	Thermal Conductivity
TCBL	Thermo-chemical boundary layer
VASP	Vienna ab initio simulation package
vVCA	vibrational Virtual Crystal Approximation

List of Acronyms

α	thermal expansivity
ω	phonon frequency
ω_i	phonon frequencies
Δ	atomic displacement
τ	phonon lifetime
γ	mode Grüneisen parameter
κ	thermal conductivity
ν	kinematic viscosity
D	thermal diffusivity
κ_{latt}	lattice thermal conductivity
κ_{rad}	radiative thermal conductivity
φ_{ij}	harmonic force constants matrix
A_{ijk}	third order lattice anharmonicity tensor
J	heat flux
PV	perovskite
PPV	post-perovskite
fp	ferropericlaase
$ModeVg$	mode group velocity

ModeCv mode heat capacity

T temperature

P pressure

T – P temperature-pressure

ρ density

PBTT Peierls-Boltzmann transport theory

RSSFD real space supercell finite displacement

IIP Interpolation of irreducible inter-atomic potentials

CHAPTER 1

INTRODUCTION

1.1 Lower Mantle Heat Flow

The Earth has a layered internal structure¹. Right beneath the surface, is the crust (about 200-300 km thick), usually categorized into continental and oceanic crust. Under the crust, is Earth's mantle which is conventionally divided into three regions associated with the phase transitions of mantle minerals revealed by the seismic discontinuity. The upper mantle is mainly made of olivine $(\text{Mg,Fe})_2\text{SiO}_4$, pyroxenes $(\text{Mg,Fe})\text{SiO}_3$ and garnet (Al-bearing silicates). The transition zone is mainly made of spinel $(\text{MgFeAl}_2\text{O}_4)$ and majorite $(\text{Mg}_3(\text{Fe,Al,Si})_2(\text{SiO}_4)_3)$ minerals. The lower mantle consists of perovskite $(\text{Mg,Fe})\text{SiO}_3$ and ferropericlase $((\text{Mg,Fe})\text{O})$. Between the lower mantle and the Earth's core (innermost layer), is the D'' layer. This layer is thought to contain the recently discovered post-perovskite² phase of $(\text{Mg,Fe})\text{SiO}_3$. The core has two sub-layers, the liquid outer core made of iron-nickel alloy, and the solid inner core made of iron. The layers, chemical composition and depth are summarized³ in table 1.1

Table 1.1: Layered structure of the Earth and composition

Layer	Depth (Km)	Chemical Composition	T(K)	P(GPa)
crust	0-10	low density crystalline rocks	300	0
Upper mantle	10-410	olivine + pyroxene + garnet	600	0-13
Transition	410-660	spinel + majorite		13-23
Lower mantle	660-2600	perovskite + ferropericlase	1200	23-125
D'' layer	2600-2900	post-perovskite + ferropericlase	2200	125-135
Outer core	2900-5100	liquid iron alloy	4000	330
Inner core	5100-6400	solid iron	5000	364

Both temperature and pressure increase with the depth. At the surface, the Earth's pressure is 1 atm and 300 K. It is currently estimated that the pressure and temperature reach to 364 GPa and 5000 K respectively at the center of core. Governed by the second law of thermodynamics, heat spontaneously flows from Earth's hot core to its cool surface, through radiation, convection, and conduction. The total heat loss at the Earth's surface is relatively well-constrained (about 46 Terawatts)⁴. However, because the rates of radiogenic heat generation and secular cooling remain poorly constrained for the mantle region, independent evaluations of the amount of heat flowing from the core into the lower mantle are much needed to understand the global heat balance. The lower mantle heat flow is one of most important geophysical processes, because of its close relevance to the outer core convection⁵ and the generation of the Earth's magnetic field⁶. The knowledge of this process is essential to our understanding of the origin, evolution, and present-day state of the Earth's physical system.

The amount of heat from the core is largely regulated by thermal conduction at the thermo-chemical boundary layer (TCBL) above the core-mantle boundary (CMB). As defined by Fourier's law of heat conduction,

$$\mathbf{J} = \kappa \nabla T \tag{1.1}$$

determination of the CMB heat flow relies on knowledge of both the temperature profile around the CMB and thermal conductivity (κ) of the lowermost mantle. Thermal conductivity (κ) also plays a crucial role in mantle dynamics. For example, κ dictates the amount of heat absorbed by the cold subducted slabs from the hot surrounding mantle. As κ appears in the Rayleigh number (R_a , equation 1.2), a measurement of the convective vigor of a system, the associated effect of lower mantle viscosity controls the structure,

thickness and dynamics of CMB⁷, the style and structure of mantle convection⁸.

$$R_a = \frac{g_0 \alpha \Delta T d^3}{\kappa v} \quad (1.2)$$

Here g is acceleration due to gravity, α is the thermal expansion coefficient, ΔT is the temperature difference between the reference mantle temperature and the Core mantle boundary, v is the kinematic viscosity, κ is the thermal conductivity. Although the effect of strongly varying viscosity is paramount, recent geodynamic simulations have clearly demonstrated that (1) the value of assumed average lower mantle conductivity is of close relevance to the strength of mantle upwellings⁹, and (2) moreover the temperature derivatives of thermal conductivity impact even more significantly the development of lower mantle plumes^{10,11}. Gubbins and Willis et al.⁶ have shown that lower mantle thermal conductivity is correlated to Earth's magnetic field generation.

Determination of thermal conductivity of Earth minerals at relevant high pressure and temperature conditions is clearly a subject of solid state physics research. The output of the solid state physics study will help earth scientists to develop interlocked deep-Earth evolution models. For example, the current estimates of Q_{CMB} are widely scattered, ranging from 5 to 15 terawatts (TW)⁵. The lower-bound-estimates suggest that additional sources of heat in the mantle such as enhanced internal heating or an additional thermal boundary layer are required to accommodate the observed budget of 47 ± 3 terawatts from the surface of the Earth^{1,5}. The upper-bound-estimates suggest a recent evolution of the inner core/outer core system and high internal temperatures for early Earth conditions¹².

1.2 Lower Mantle Minerals

The Earth's lower mantle is composed predominantly of magnesium oxides and silicates. Understanding and predicting the behavior of these compounds is key to understanding

the behavior and evolution of the Earth’s lower mantle. The most abundant mineral in the Earth’s lower mantle is magnesium silicate MgSiO_3 , comprising more than 70% of the lower mantle volume¹³. Fe^{2+} and/or Fe^{3+} distributed in these phases¹ however the exact oxidation and spin state of Fe are subject of current scientific debate. The distribution of Fe is believed to be around 10%. Perovskite PV- MgSiO_3 is the stable phase of magnesium silicate (MgSiO_3). Above 120GPa, PV- MgSiO_3 transforms into a post-perovskite phase. PPV- MgSiO_3 The PV \rightarrow PPV transition is thought to explain seismic discontinuities in the Earth’s D” layer.

Ferropericlase-(Mg,Fe)O is known to be the second most abundant mineral in the Earth’s lower mantle constituting about 20% of lower mantle volume. It is the result of substitution of Mg in Fe-free MgO by Fe^{2+} . Understanding the behaviour of (Mg,Fe)O is key to understanding the dynamics of the Earth’s lower mantle. Moreover the high-spin to low-spin transition in (Mg,Fe)O, has been the focus of recent studies^{14–16}.

1.3 Lattice Thermal Conductivity of Lower Mantle Minerals

Heat is a nonmechanical means of energy transfer between a system and its environment. In the presence of a temperature difference, heat flows spontaneously from high to low temperature regions. The heat flux \mathbf{J} , defines the rate of heat energy transfer through a given surface. Heat is transmitted via three mechanisms: conduction(cond), convection(conv) and radiation(rad). As a result, the total heat flux \mathbf{J} , has three components as shown in equation 1.3, and heat transfer via these three mechanisms often occurs simultaneously.

$$\mathbf{J} = \mathbf{J}_{conv} + \mathbf{J}_{rad} + \mathbf{J}_{cond} \tag{1.3}$$

Convective heat transfer is important in all situations where there is bulk flow of matter, carrying heat along with the mass flow. Thus \mathbf{J}_{conv} is the dominant heat transfer mechanism

in liquid media. The Earth’s lower mantle is not liquid, therefore \mathbf{J}_{conv} is not important in this region.

Heat transfer by radiation is ballistic in nature and it occurs via electromagnetic (e.m) waves and does not require a material medium. According to the Stefan-Boltzmann law for black body radiation,

$$\mathbf{J}_{rad} \propto T^4 \tag{1.4}$$

Due to this T^4 dependence, the ballistic \mathbf{J}_{rad} is a very important component of the total heat flux in all high temperature laboratory experiments that have steep temperature gradients and involve direct (or boundary-to-boundary or ballistic) radiative transfer wherein light from the source warms the thermocouple with little to no participation of the medium. Corruption of measurements intended to probe \mathbf{J}_{cond} by spurious radiative transfer and misinterpretation of this process as diffusive has led to incorrect forms for the diffusive thermal conductivity. Hofmeister also suggests that radiative transfer exists at lower T because (1) direct radiative transfer increases gradually with T, i.e., no abrupt onset exists, (2) a small radiative component is clearly seen by 350 K in laser flash analysis (LFA) experiments, even when samples are coated with metal and/or graphite. A small amount of radiative transfer at 298 K probably exists in most experiments^{17–20} Hofmeister also argues that the ballistic radiative transfer may be large in DAC experiments²¹ because thermal losses at sample interfaces provide an error in the opposite direction. In contrast, it is widely assumed that the ballistic radiative heat transfer is not important inside Earth’s mantle because mantle minerals are grainy²². The temperature gradient inside the Earth is only about several kelvins over a kilometer. It is reasonable to approximate that minerals reach thermal equilibrium within its grains, and radiative heat will be absorbed and randomly scattered from grain-to-grain. At the geological length scale, the radiative heat transfer contributes to an effective diffusive thermal conductivity. This indirect/diffusive thermal conductivity due to radiative photons can not be directly measured in laboratory. Instead

they are modeled based on the optical properties of minerals, equation 1.5 The Rosseland mean approximation for an optically thick medium conducting heat by radiative transport is:

$$Q_{rad} = -\frac{16\sigma n^2 T^3}{3\beta_R} \nabla T = -\kappa_{rad} \nabla T \quad (1.5)$$

$$\text{with } \frac{n^2}{\langle \beta_R \rangle} = \frac{\pi}{4\sigma T^3} \int_0^\infty \frac{n_\lambda^2}{\beta_\lambda} \frac{dI_{b,\lambda}}{dT} d\lambda.$$

Here n is the index of refraction, σ is the Stefan-Boltzmann constant, β_R is the Rosseland mean extinction coefficient, λ is wavelength, n_λ is the spectral index of refraction, β_λ is the spectral extinction coefficient, and $I_{b,\lambda}$ is the Planck black body intensity function.

Heat transfer by conduction is diffusive in nature, without a bulk flow of matter and is usually driven by a temperature gradient. \mathbf{J}_{cond} is the dominant mechanism of heat transfer in solids and is achieved via electrons, phonons (lattice vibrations) and other thermal excitations (quasi-particles). In metallic solids, heat is conducted mainly by electrons. According to Wiedemann-Franz (W-F) law equation 1.6 the ratio of thermal conductivity to the electrical conductivity of a metal is proportional to the temperature(T).

$$\frac{\kappa}{\sigma} = LT \quad (1.6)$$

Where κ is the thermal conductivity, and σ is the electrical conductivity. L is the Lorentz number²³. We can see from W-F law that as temperature increases, the thermal conductivity increases while the electrical conductivity decreases.

In non-metallic solids the dominant mechanism of heat transfer is via lattice vibrations (phonons). The conduction of heat via the propagation of vibrations in a solid in response to a temperature gradient is often referred to as lattice thermal conductivity (LTC). At low temperatures and in grainy(optically thick) and insulating media, the dominant mechanism of heat transfer is conduction by phonons. In such media, lattice thermal conductivity lattice thermal conductivity (κ_{latt}), is the fundamental property that regulates the flow of heat in

response to a temperature difference. According to Fourier's law κ relates the heat flux \mathbf{J} , through a material to the temperature gradient ∇T according to equation 1.1 Even though heat transfer is often associated with macroscopic objects, the physical properties that constrain the flow of heat in a material are ultimately tied to the microscopic constituents of the material. Inside crystal solids, phonons can be scattered by crystalline defects, grain boundaries and lattice anharmonicity. The phonon lifetime (τ), which characterizes the length of time that elapses before a phonon mode is scattered, is key to determining the thermal conductivity of a material. Other factors necessary to determine the thermal conductivity of a material include the phonon mode group velocities, and heat capacities. While temperature is known to strongly affect the phonon lifetime (τ) and heat capacity, high pressures significantly alter the elastic constants, phonon group velocities and densities of states. As a result, first-principles study of temperature and pressure dependence of thermal conductivity can advance our understanding of thermal transport in solid media.

The work presented in this thesis is focused on the conduction of heat in non metallic crystal solids and Earth minerals via lattice waves (phonons). Detail treatment of the other mechanisms of heat conduction can be found elsewhere²⁴⁻²⁹. The study of thermal conductivity is of great technological interest because of the importance of both very high and low thermal conductivity materials in various heat management technologies. High thermal conductivity materials have potential applications in heat management in electronics³⁰⁻³². Low thermal conductivity materials on the other hand are the focus of recent studies in the search for high efficient thermoelectric materials³³⁻³⁸ and materials for thermal-barrier coating applications³⁹⁻⁴². The study of thermal conductivity provides useful guidelines to the design of novel materials with unique applications in heat management.

LTC of the lower mantle κ_{LM} regulates the heat flux across the core mantle boundary (CMB) and impacts convection throughout the mantle. κ_{LM} is crucial in determining the total heat budget of the Earth. Despite its importance, κ_{LM} is poorly constrained due to the

challenges in carrying out measurements at temperature and pressure conditions relevant to the Earth's interior.

Understanding and constraining the thermal conductivity of a material, is an example of a material science problem with importance in Earth science and at the heart of solid state physics. First-principles calculations offer us new insights to material properties at extreme conditions, yet are very challenging.

1.4 Challenges of Measuring κ at High Temperatures and Pressures

Conventional measurements of thermal conductivity (κ), involve determining a temperature gradient across a sample subjected to steady heat flow^{43–46}. Other approaches involve transient heating of the sample and then a study of the temperature evolution with time. These techniques measure the thermal diffusivity (D), which is related to the κ by equation 1.7:

$$D = \frac{\kappa}{\rho C_p} \quad (1.7)$$

Where ρ is the density and C_p is the isobaric heat capacity. Over recent years, various new techniques have been developed and used to measure κ or D . Contact methods like Ångström's method^{47,48}, Transient hot-wire technique⁴⁹, and contact-free techniques like laser flash analysis (LFA)¹⁹, Optical thermal grating technique^{50–52}, Optical pulse transient heating method^{53–56}, and time-domain thermoreflectance (TDTR)⁵⁷ have been developed and used with great success to measure κ at various T,P conditions. Contrary to contact methods where the sample is in direct contact with the heating source or the thermocouple used to determine heat flow the sample has no direct contact in the contact-free techniques.

Measurements from contact methods are known to include systematic errors arising from thermal contact resistance and differential thermal expansion, leading to underestimation of κ_{latt} . Contact-free techniques like the LFA avoid these problems but are limited by

requirement of very large sample size. A comprehensive review of the strengths and weakness of these techniques is reported elsewhere¹⁹. Other challenges faced in accurately constraining κ or D in experiment include the instability of some samples at ambient conditions, dealing with unwanted direct radiative transfer in optically thin or partially transparent samples, and eliminating errors associated with surface roughness and presence of materials with P-T dependent thermophysical properties⁴³. All these challenges often limit the pressure range for which κ can be accurately determined in the laboratory. For instance, the lattice thermal conductivity of ferropericlase- $\text{Mg}_{(1-x)}\text{Fe}_x\text{O}$ and Fe-bearing silicate perovskite- $\text{Mg}_{(1-x)}\text{Fe}_x\text{SiO}_3$ has not been measured at lower mantle temperatures and pressures⁵⁸. Despite the success achieved in measuring equilibrium thermodynamic properties of solids, certain temperature and pressure (T-P) conditions relevant to studies of the Earth’s deep interior, remain inaccessible to experiments. Current geophysical estimates are based on long extrapolations from low-pressure data^{11,17,43}.

1.5 First-principles Calculations of Lattice Thermal Conductivity: Motivations and Recent Progress

First-principles calculations offer an invaluable alternative approach to experimental techniques. The terminology of first-principles or ab initio simulations is referred to simulations that are based on quantum and statistical mechanical theory to predict the behavior of matter at the atomistic scale and how it affects the macroscopic behavior of the material, without any inputs and/or fitting of experimental data. A fundamental challenge of material theory and simulation is the fact that each piece of solid material consists of around 10^{23} strongly interacting positively charged ions and negatively charged valence electrons. Due to their small masses and rapid speeds, electrons inside a solid have to be described with quantum mechanics, instead of classical Newtonian mechanics.

The density-functional theory (DFT) developed by Hohenberg, Kohn and Sham^{59,60} in the 1960s has profound influence in materials science and engineering. This theory adopts a series of systematical approximations to map a complicated many-electron problem into a relatively simple independent electron problem. More importantly, this formalism allows theorists to take advantage of fast computers and large storage space to calculate a wide range of complex quantum electronic structures (i.e. chemical bonding) using numerical methods, and then to predict atomic structures and atomic vibration from first-principles, i.e. without any a priori experimental knowledge. In the past twenty years, many efficient software packages like VASP^{61,62}, ABINIT^{63,64}, QUANTUM EXPRESSO⁶⁵ have been developed and widely adapted to study atomic structure and equilibrium thermodynamic properties of crystals⁶⁶.

These first-principles methods have been used to study a wide range of important material properties such as melting⁶⁷ electronic structure^{66,68,69}, phase transitions⁷⁰⁻⁷⁹, elasticity⁸⁰⁻⁸⁴, vibrational phonon spectra^{85,86}, structural stability⁸⁷⁻⁸⁹, Raman spectra^{90,91} and thermal equation of state^{29,92-98}. Recent advances in parallel computing technologies and declining cost of hardware and storage have made it possible to apply density functional theory (DFT) based first-principles methods⁹⁹ to study more complex material systems over a wide range of temperature and pressure conditions. Some advantages of predictive first-principles theoretical models include the selection of materials for important technological applications, the design of novel materials with promising properties¹⁰⁰ and understanding behavior of materials key to constraining heat flow in the Earth's deep interior.

Despite the successes recorded in the prediction of equilibrium thermal properties, first-principles calculations of non-equilibrium properties, such as lattice thermal conductivity or viscosity are limited due to significant increase in computational intensity. There are no software packages available and calculations rely on time-consuming in-house methodology development. To better constrain the heat flow in the Earth's deep interior,

robust theoretical models with predictive capability are much needed. The motivation of this work is to predict lattice thermal conductivity (κ_{latt}) for a wide range of materials at high temperatures and pressures relevant to the Earth’s lower mantle. Starting from simple cubic 2-atom MgO, our goal is to study more complex mineral compositions like 10-atom trigonal Al₂O₃, 20-atom orthorhombic MgSiO₃, and iron-bearing mineral solid solutions like (Mg,Fe)O.

In the last five years, several theoretical approaches^{58,101–108} for predicting lattice thermal conductivity reported in literature¹⁰⁹. These methods can be categorized into three types: (1) Green-kubo method^{110,111} based on the fluctuation-dissipation theorem and molecular dynamics simulations, (2) Non-equilibrium molecular dynamics(NEMD), (3) Peierls-Boltzmann transport theory.

The Green-Kubo method relates the lattice thermal conductivity of a system to the time required for temperature induced fluctuations in the instantaneous heat flux to dissipate equation 1.8.

$$\kappa_{ij} = \frac{V}{k_B T^2} \int_0^\infty \langle J_i(t) J_j(0) \rangle dt \tag{1.8}$$

where i, j are components of lattice thermal conductivity tensor, V is the volume of the system, k_B is the Boltzmann constant, T is the temperature, $J_i(t)$ is the instantaneous heat flux in the i^{th} direction at time t . One major advantage of the Green-Kubo formalism is that one can determine the entire lattice thermal conductivity tensor from one simulation. This is particularly important in calculations of non-isotropic materials. A serious limitation to this method is that it often requires a long time for the heat flux correlation to decay to zero and the need to identify the self energy terms of atoms¹⁰⁸.

Non-equilibrium molecular dynamics (NEMD) simulations impose a fixed temperature gradient on a supercell and the heat flux required to maintain it is calculated. NEMD

simulations require very large simulation cells and contain noticeable finite size effects, which sometimes are corrected with unreliable empirical models⁵⁸.

Peierls-Boltzmann transport theory describes thermal conductivity in terms of specific heat capacity (C_v), group velocities (V_g), and lifetimes τ of all the phonon modes: $\kappa = \frac{1}{3} \sum C_v v_g^2 \tau$. Both C_v and V_g are calculated based on harmonic lattice dynamics, while the phonon lifetime τ is estimated either using equilibrium molecular dynamics simulations¹⁰⁶, or quantum scattering theory¹⁰¹.

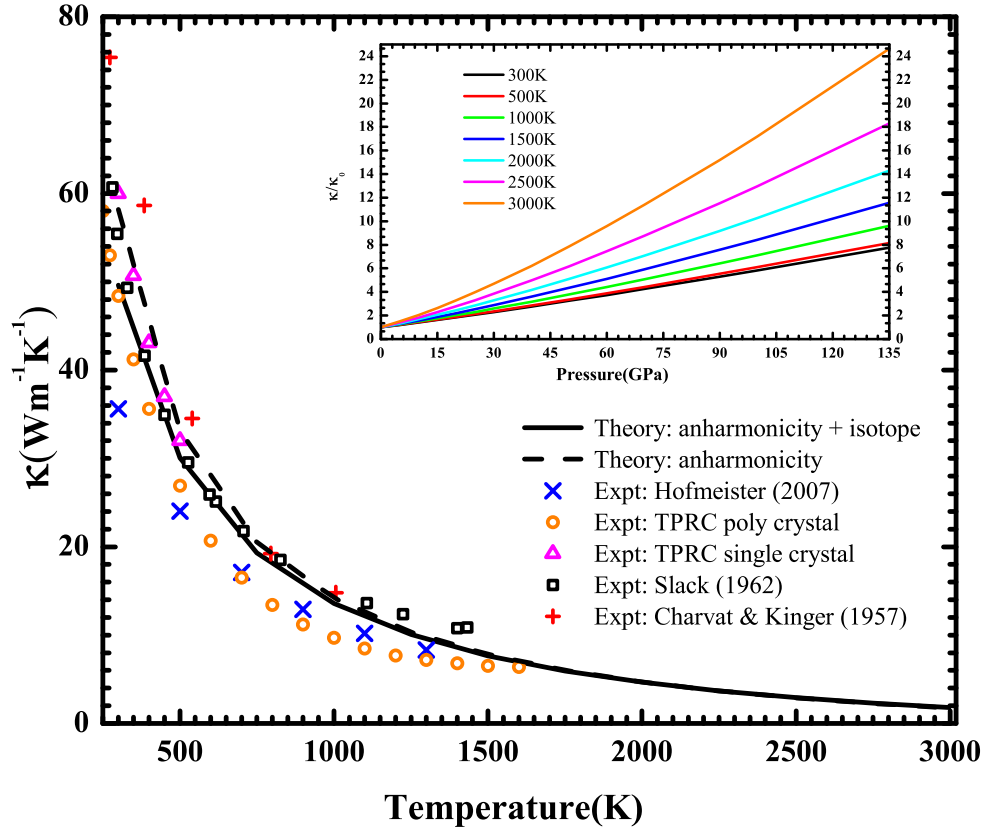


Figure 1.1: Isobaric κ_{latt} of MgO derived based on our LDA calculated thermal equation of state. Discrete symbols represent experimental measurements. Inset: Normalized κ_{latt} v.s. pressure. For the seven isotherms (300K, 500K, 1000K, 1500K, 2000K, 2500K, 3000K), κ_0 is the lattice thermal conductivity at 0 GPa. Our new calculation shows a slight improvement over the previously published results thanks to the optimization of our computational technique, for speed and accuracy.

All the first-principles calculations reported in this dissertation are based on our newly developed computational method that combines Peierls-Boltzmann transport theory, quantum scattering theory, and first-principles DFT methods^{101,112}. Figure 1.1 shows our first-principles predicted thermal conductivity of MgO over a wide temperature-pressure range. Our predicted values at 0 GPa are in excellent agreement with available measurements. Our techniques are ideal for massive parallelization. During the course of my Ph.D study, we have significantly improved the numerical efficiency of our techniques and adopted them to study of lattice thermal conductivity, for the following minerals: α -Al₂O₃ (10-atoms/unit cell), MgSiO₃ (20-atoms/unit cell) and ferropericlase-(Mg,Fe)O.

1.6 Outline of Dissertation

The rest of this dissertation is organized as follows: Chapter 2 covers the theory of lattice vibrations. Chapter 3 presents the Peierls-Boltzmann Transport Theory, in chapter 4 we report the lattice thermal conductivity of corundum structured Al₂O₃ crystal. In chapter 5, the lattice thermal conductivity of silicate perovskite is reported. Chapter 6 presents the vibrational virtual crystal approximation of lattice dynamics and lattice thermal conductivity in ferropericlase Mg_(1-x)Fe_xO with x=12.5%. In chapter 7, the implications for heat flow across the Core-Mantle Boundary (CMB) are discussed. Chapter 8 presents a summary of the dissertation, and recommendations for future work.

CHAPTER 2

FIRST-PRINCIPLES CALCULATION OF HARMONIC AND ANHARMONIC LATTICE DYNAMICS

2.1 Interatomic Potentials

In solids, the chemical bonds, which hold constituent atoms together, are strong yet not 100% rigid. Consequently the atoms oscillate about their equilibrium positions. When the amplitudes of these vibrations are small compared to the interatomic spacing, the interaction potential energy between atoms can be expanded as a function of the atomic displacements from their equilibrium positions. Under this assumption, the total interatomic potential energy of the crystal lattice can be expressed as follows:

$$\begin{aligned}
 V = & V_{static} + \sum_{\ell,i,\alpha} \left(\frac{\partial V}{\partial x_{\alpha,i}(\ell)} \right)_0 x_{\alpha,i}(\ell) \\
 & + \frac{1}{2} \sum_{\ell,i,\alpha} \sum_{\ell',j,\beta} \left(\frac{\partial^2 V}{\partial x_{\alpha,i}(\ell) \partial x_{\beta,j}(\ell')} \right)_0 x_{\alpha,i}(\ell) x_{\beta,j}(\ell') \\
 & + \frac{1}{6} \sum_{\ell,i,\alpha} \sum_{\ell',j,\beta} \sum_{\ell'',k,\gamma} \left(\frac{\partial^3 V}{\partial x_{\alpha,i}(\ell) \partial x_{\beta,j}(\ell') \partial x_{\gamma,k}(\ell'')} \right)_0 x_{\alpha,i}(\ell) x_{\beta,j}(\ell') x_{\gamma,k}(\ell'') \\
 & + \frac{1}{24} \sum_{\ell,i,\alpha} \sum_{\ell',j,\beta} \sum_{\ell'',k,\gamma} \sum_{\ell''',l,\lambda} \left(\frac{\partial^4 V}{\partial x_{\alpha,i}(\ell) \partial x_{\beta,j}(\ell') \partial x_{\gamma,k}(\ell'') \partial x_{\lambda,l}(\ell''')} \right)_0 \\
 & x_{\alpha,i}(\ell) x_{\beta,j}(\ell') x_{\gamma,k}(\ell'') x_{\lambda,l}(\ell''') \\
 & + \dots
 \end{aligned} \tag{2.1}$$

Here V represents the total interatomic potential energy, V_0 is the binding energy of the crystal when all the atoms are at their equilibrium positions. $x_{\alpha,i}(\ell)$ denotes the α cartesian component of the displacement of the i^{th} atom in the ℓ^{th} unit cell. The subscript 0 indicates that the derivatives are evaluated with atoms at the equilibrium positions. Consequently, the first order derivatives $\left(\frac{\partial V}{\partial x_{\alpha,i}(\ell)}\right)_0$, which represent the net forces on the atom F_i , at equilibrium vanish and the second term in equation 2.1 is zero. The second order derivatives of the total inter-atomic potential energy $\varphi_{\alpha i, \beta j}(\ell, \ell') = \left(\frac{\partial^2 V}{\partial x_{\alpha,i}(\ell) \partial x_{\beta,j}(\ell')}\right)_0$ can be interpreted as harmonic spring force constants. The elements of the harmonic force constants matrix have the translational symmetry:

$$\varphi_{\alpha i, \beta j}(\ell, \ell') = \varphi_{\alpha i, \beta j}(0, \ell - \ell') = \varphi_{\alpha i, \beta j}(\ell - \ell', 0) \quad (2.2)$$

Equation 2.1 can be re-written as follows:

$$\begin{aligned} V &= V_0 + \frac{1}{2} \sum_{\ell, i, \alpha} \sum_{\ell', j, \beta} \varphi_{\alpha i, \beta j}(\ell, \ell') x_{\alpha, i}(\ell) x_{\beta, j}(\ell') \\ &+ \frac{1}{6} \sum_{\ell, i, \alpha} \sum_{\ell', j, \beta} \sum_{\ell'', k, \gamma} A_{\alpha i, \beta j, \gamma k}(\ell, \ell', \ell'') x_{\alpha, i}(\ell) x_{\beta, j}(\ell') x_{\gamma, k}(\ell'') \\ &+ \frac{1}{24} \sum_{\ell, i, \alpha} \sum_{\ell', j, \beta} \sum_{\ell'', k, \gamma} \sum_{\ell''', l} B_{\alpha i, \beta j, \gamma k, \lambda l}(\ell, \ell', \ell'', \ell''') x_{\alpha, i}(\ell) x_{\beta, j}(\ell') x_{\gamma, k}(\ell'') x_{\lambda, l}(\ell''') \\ &+ \dots \end{aligned} \quad (2.3)$$

Where:

$$\begin{aligned} \varphi_{\alpha i, \beta j}(\ell, \ell') &= \left(\frac{\partial^2 V}{\partial x_{\alpha, i}(\ell) \partial x_{\beta, j}(\ell')} \right)_0 \\ A_{\alpha i, \beta j, \gamma k}(\ell, \ell', \ell'') &= \left(\frac{\partial^3 V}{\partial x_{\alpha, i}(\ell) \partial x_{\beta, j}(\ell') \partial x_{\gamma, k}(\ell'')} \right)_0 \\ B_{\alpha i, \beta j, \gamma k, \lambda l}(\ell, \ell', \ell'', \ell''') &= \left(\frac{\partial^4 V}{\partial x_{\alpha, i}(\ell) \partial x_{\beta, j}(\ell') \partial x_{\gamma, k}(\ell'') \partial x_{\lambda, l}(\ell''')} \right)_0 \end{aligned} \quad (2.4a)$$

2.2 Harmonic Lattice Dynamics

2.2.1 Harmonic Approximation

Within the harmonic approximation, third and higher order lattice anharmonicity are neglected, and the Hamiltonian of a vibrating lattice can be expressed as:

$$H = V_0 + KE + V_{harmonic} \quad (2.5)$$

Where KE is the kinetic energy defined as:

$$KE = \sum_{\ell, i, \alpha} \frac{p_{\alpha, i}^2(\ell)}{2m_i} \quad (2.6)$$

and

$$V_{harmonic} = \frac{1}{2} \sum_{\ell, i, \alpha} \sum_{\ell', j, \beta} \varphi_{\alpha i, \beta j}(\ell, \ell') x_{\alpha, i}(\ell) x_{\beta, j}(\ell') \quad (2.7)$$

Here $p_{\alpha, i}(\ell)$ and m_i are the α cartesian component of the momentum and mass of the i^{th} atom in the ℓ^{th} unit cell respectively. $\varphi_{\alpha i, \beta j}(\ell, \ell')$ is defined above.

Solving the Hamiltonian of an infinitely large periodic lattice in real space is not trivial. However, we can take advantage of the translational symmetry of the crystal and rewrite the Hamiltonian in the reciprocal (\vec{q}) space using Fourier transformations:

$$\begin{aligned} X_{\alpha, i}(\mathbf{q}) &= \frac{1}{\sqrt{N}} \sum_{\ell} x_{\alpha, i}(\ell) e^{-i\mathbf{q}\cdot\boldsymbol{\ell}} \\ P_{\alpha, i}(\mathbf{q}) &= \frac{1}{\sqrt{N}} \sum_{\ell} p_{\alpha, i}(\ell) e^{i\mathbf{q}\cdot\boldsymbol{\ell}} \end{aligned} \quad (2.8)$$

where $\alpha = 1, 2, \dots, 3N_a$ that labels the index of branch and N_a is the number of atoms in a primitive unit cell. N is the number of unit cells in the supercell model of the crystal, \mathbf{q} is

the wave vector in the reciprocal space.

Note that $X_{\alpha,i}(\mathbf{q})$ and $P_{\alpha,i}(\mathbf{q})$ also have translational symmetry in reciprocal space:

$$\begin{aligned} X_{\alpha,i}(\mathbf{q} + \mathbf{g}) &= X_{\alpha,i}(\mathbf{q}) \\ P_{\alpha,i}(\mathbf{q} + \mathbf{g}) &= P_{\alpha,i}(\mathbf{q}) \end{aligned} \tag{2.9}$$

Here \mathbf{g} is a reciprocal lattice point and $e^{i\mathbf{q}\cdot\boldsymbol{\ell}} = 1$. Since $x_{\alpha,i}(\boldsymbol{\ell})$ and $p_{\alpha,i}(\boldsymbol{\ell})$ are real, we can show that $X_{\alpha}^*(\mathbf{q}) = X_{\alpha}(-\mathbf{q})$ and $P_{\alpha}^*(\mathbf{q}) = P_{\alpha}(-\mathbf{q})$

Conversely, in real space,

$$\begin{aligned} x_{\alpha,i}(\boldsymbol{\ell}) &= \frac{1}{\sqrt{N}} \sum_{\mathbf{q}} X_{\alpha,i}(\mathbf{q}) e^{i\mathbf{q}\cdot\boldsymbol{\ell}} \\ p_{\alpha,i}(\boldsymbol{\ell}) &= \frac{1}{\sqrt{N}} \sum_{\mathbf{q}} P_{\alpha,i}(\mathbf{q}) e^{-i\mathbf{q}\cdot\boldsymbol{\ell}} \end{aligned} \tag{2.10}$$

With these transformations, the equation 2.6 becomes:

$$\begin{aligned} KE &= \frac{1}{2} \sum_{q,q',i,\alpha} \frac{1}{m_i} P_{\alpha,i}(\mathbf{q}) P_{\alpha,i}(\mathbf{q}') \frac{1}{N} \sum_{\boldsymbol{\ell}} e^{-i(\mathbf{q}+\mathbf{q}')\cdot\boldsymbol{\ell}} \\ &= \frac{1}{2} \sum_{q,q',i,\alpha} \frac{1}{m_i} P_{\alpha,i}(\mathbf{q}) P_{\alpha,i}(\mathbf{q}') \delta_{\mathbf{q}+\mathbf{q}',0} \\ &= \frac{1}{2} \sum_{q,i,\alpha} \frac{1}{m_i} P_{\alpha,i}(\mathbf{q}) P_{\alpha,i}(-\mathbf{q}) \\ &= \frac{1}{2} \sum_{q,i,\alpha} \frac{1}{m_i} P_{\alpha,i}(\mathbf{q}) P_{\alpha,i}^*(\mathbf{q}) \\ &= \frac{1}{2} \sum_{q,i,\alpha} \frac{|P_{\alpha,i}(\mathbf{q})|^2}{m_i} \end{aligned}$$

Letting $\mathbf{h} = \boldsymbol{\ell} - \boldsymbol{\ell}'$ i.e $\boldsymbol{\ell} = \boldsymbol{\ell}' + \mathbf{h}$

Equation 2.7 becomes

$$\begin{aligned}
V_{harmonic} &= \frac{1}{2} \sum_{i,\alpha} \sum_{j,\beta} \sum_h \varphi_{\alpha i, \beta j}(h, 0) \sum_{q, q'} X_{\alpha, i}(q) X_{\beta, j}(q') e^{i\mathbf{q} \cdot \mathbf{h}} \frac{1}{N} \sum_{\ell'} e^{i(\mathbf{q} + \mathbf{q}') \cdot \boldsymbol{\ell}'} \\
&= \frac{1}{2} \sum_{i,\alpha} \sum_{j,\beta} \sum_q \sum_h \varphi_{\alpha i, \beta j}(h, 0) X_{\alpha, i}(q) X_{\beta, j}(-q) e^{i\mathbf{q} \cdot \mathbf{h}}
\end{aligned} \tag{2.11}$$

We define

$$\varphi_{\alpha i, \beta j}(\mathbf{q}) = \sum_h \varphi_{\alpha i, \beta j}(h, 0) e^{i\mathbf{q} \cdot \mathbf{h}}$$

Note that,

$$\varphi_{\alpha i, \beta j}^*(\mathbf{q}) = \varphi_{\alpha i, \beta j}(-\mathbf{q}) = \varphi_{\beta j, \alpha i}(\mathbf{q}) \tag{2.12}$$

So the equation 2.11 becomes

$$V_{harmonic} = \frac{1}{2} \sum_{i,\alpha} \sum_{j,\beta} \sum_q \varphi_{\alpha i, \beta j}(\mathbf{q}) X_{\alpha, i}(q) X_{\beta, j}(-q) \tag{2.13}$$

The Hamiltonian can now be expressed as:

$$H = V_0 + \sum_{\mathbf{q}} H(\mathbf{q}) \tag{2.14}$$

Where

$$H(\mathbf{q}) = \frac{1}{2} \frac{|P_{\alpha, i}(\mathbf{q})|^2}{m_i} + \frac{1}{2} \sum_{j,\beta} \varphi_{\alpha i, \beta j}(\mathbf{q}) X_{\alpha, i}(q) X_{\beta, j}(-q) \tag{2.15}$$

We can solve the equation of motion of lattice vibration using the canonical equations:

$$\begin{aligned}\frac{\partial H}{\partial X_{\alpha,i}(\mathbf{q})} &= -\dot{P}_{\alpha,i}(\mathbf{q}) \\ \frac{\partial H}{\partial P_{\alpha,i}(\mathbf{q})} &= \dot{X}_{\alpha,i}(\mathbf{q})\end{aligned}\tag{2.16}$$

Now,

$$\frac{\partial H}{\partial X_{\alpha,i}(\mathbf{q})} = \frac{1}{2} \sum_{j,\beta} \varphi_{\alpha i, \beta j}(\mathbf{q}) X_{\beta,j}^*(q) + \frac{1}{2} \sum_{j,\beta} \varphi_{\beta j, \alpha i}(-\mathbf{q}) X_{\beta,j}^*(q)\tag{2.17}$$

Using equation 2.12, the first canonical equation becomes:

$$\frac{\partial H}{\partial X_{\alpha,i}(\mathbf{q})} = \sum_{j,\beta} \varphi_{\alpha i, \beta j}(\mathbf{q}) X_{\beta,j}^*(q) = -\dot{P}_{\alpha,i}(\mathbf{q})\tag{2.18}$$

Similarly, the second canonical equation becomes:

$$\frac{\partial H}{\partial P_{\alpha,i}(\mathbf{q})} = \frac{P_{\alpha,i}^*(\mathbf{q})}{m_{\alpha}} = \dot{X}_{\alpha,i}(\mathbf{q})\tag{2.19}$$

Using equation 2.12 we obtain,

$$\ddot{X}_{\alpha,i}(\mathbf{q}) + \frac{1}{m_{\alpha}} \sum_{j,\beta} \varphi_{\alpha i, \beta j}^*(\mathbf{q}) X_{\beta,j}(q) = 0\tag{2.20}$$

Let

$$X_{\alpha i}(\mathbf{q}) = \frac{1}{\sqrt{m_{\alpha}}} e^{i\omega(\mathbf{q})t} \hat{e}_{\alpha i}(\mathbf{q})\tag{2.21}$$

equation 2.20 becomes

$$\frac{-\omega^2}{\sqrt{m_\alpha}} \hat{e}_{\alpha,i}(\mathbf{q}) + \frac{1}{m_\alpha} \sum_{j,\beta} \varphi_{\alpha i, \beta j}^*(\mathbf{q}) \frac{1}{\sqrt{m_\beta}} \hat{e}_{\beta,j} = 0 \quad (2.22)$$

$$ie \sum_{j,\beta} \left[\frac{\varphi_{\alpha i, \beta j}^*(\mathbf{q})}{\sqrt{m_\alpha m_\beta}} - \omega^2 \delta_{\alpha\beta} \right] \hat{e}_{\beta,j} = 0 \quad (2.23)$$

Where $\hat{e}_{\alpha i}(\mathbf{q})$ and $\omega(\mathbf{q})$ are the eigenvectors and eigenfrequencies of the dynamic matrix $D(\mathbf{q})$ which is defined as:

$$D_{\alpha i, \beta j}(\mathbf{q}) = \frac{\varphi_{\alpha i, \beta j}^*(\mathbf{q})}{\sqrt{m_\alpha m_\beta}} = \sum_{\mathbf{h}} \frac{\varphi_{\alpha i, \beta j}(\mathbf{h}, 0)}{\sqrt{m_\alpha m_\beta}} e^{-i\mathbf{q} \cdot \mathbf{h}} \quad (2.24)$$

For each \mathbf{q} -point, a $D(\mathbf{q})$ matrix has $3N_a$ eigenvalues/eigenvectors. The eigenvalues represent the frequencies (ω) of normal modes of vibrations. The dependence of the vibration frequencies on the wave vectors is often referred to as phonon dispersion relation and the slope of a dispersion curve ($\nabla_{\mathbf{q}}\omega(\mathbf{q})$) represents the velocity of propagation of the phonon through the crystal lattice also known as the phonon group velocity $V_g(\mathbf{q})$. Of the $3N_a$ modes, three are usually the acoustic modes while the remaining $3N_a - 3$ are optical modes.

2.2.2 Second Quantization

I now introduce normal mode coordinates,

$$\begin{aligned} Q_\lambda(\mathbf{q}) &= \sum_{i,\alpha} \sqrt{m_i} e_{\alpha,i}^*(\mathbf{q}, \lambda) \cdot X_{\alpha,i}(\mathbf{q}) \\ P_\lambda(\mathbf{q}) &= \sum_{i,\alpha} \frac{1}{\sqrt{m_i}} e_{\alpha,i}(\mathbf{q}, \lambda) \cdot P_{\alpha,i}(\mathbf{q}) \end{aligned} \quad (2.25)$$

Conversely,

$$\begin{aligned} X_\alpha(\mathbf{q}) &= \sum_{i,\lambda} \frac{1}{\sqrt{m_i}} e_{\alpha,i}(\mathbf{q}, \lambda) \cdot Q_\lambda(\mathbf{q}) \\ P_\alpha(\mathbf{q}) &= \sum_{i,\lambda} \sqrt{m_i} e_{\alpha,i}^*(\mathbf{q}, \lambda) \cdot P_\lambda(\mathbf{q}) \end{aligned} \quad (2.26)$$

Note that $Q_i^*(\mathbf{q}) = Q_i(-\mathbf{q})$ and $P_i^*(\mathbf{q}) = P_i(-\mathbf{q})$.

$e_{\alpha,i}(\mathbf{q}, \lambda)$ is an eigenvector with the following property:

$$\sum_{i,\alpha} e_{\alpha,i}(\mathbf{q}, \lambda) \cdot e_{\alpha,i}^*(\mathbf{q}, \epsilon) = \delta_{\lambda\epsilon}$$

After some derivation it can be shown that within the harmonic approximation, the Hamiltonian takes the form:

$$H(\mathbf{q}) = \frac{1}{2} \sum_{\lambda} (|P_\lambda(\mathbf{q})|^2 + \omega_\lambda^2(\mathbf{q}) |Q_\lambda(\mathbf{q})|^2) \quad (2.27)$$

Under the second quantization, the creation and annihilation operators are defined in terms of the normal coordinates as follows:

$$\hat{a}_\lambda(\mathbf{q}) = \frac{1}{\sqrt{2\hbar\omega_\lambda(\mathbf{q})}} (\omega_\lambda(\mathbf{q}) \hat{Q}_\lambda(\mathbf{q}) + i\hat{P}_\lambda(-\mathbf{q})) \quad (2.28)$$

$$\hat{a}_\lambda^+(\mathbf{q}) = \frac{1}{\sqrt{2\hbar\omega_\lambda(\mathbf{q})}} (\omega_\lambda(\mathbf{q}) \hat{Q}_\lambda(-\mathbf{q}) - i\hat{P}_\lambda(\mathbf{q})) \quad (2.29)$$

Conversely

$$\begin{aligned} \hat{Q}_\lambda(\mathbf{q}) &= \frac{\hbar}{\sqrt{2\hbar\omega_\lambda(\mathbf{q})}} (\hat{a}_\lambda^+(-\mathbf{q}) + \hat{a}_\lambda(\mathbf{q})) \\ \hat{P}_\lambda(\mathbf{q}) &= i \frac{\sqrt{\hbar\omega_\lambda(\mathbf{q})}}{2} (\hat{a}_\lambda^+(\mathbf{q}) - \hat{a}_\lambda(-\mathbf{q})) \end{aligned} \quad (2.30)$$

Here

$$\begin{aligned} [\hat{Q}_\lambda(\mathbf{q}), \hat{P}_\epsilon(\mathbf{q})] &= i\hbar \cdot \delta_{\lambda\epsilon} \delta_{\mathbf{q}\mathbf{q}'} \\ [\hat{a}_\lambda(\mathbf{q}), \hat{a}_\epsilon^+(\mathbf{q})] &= \delta_{\lambda\epsilon} \delta_{\mathbf{q}\mathbf{q}'} \end{aligned} \quad (2.31)$$

In terms of $\hat{a}_\lambda(\mathbf{q})$ and $\hat{a}_\lambda^+(\mathbf{q})$ the Hamiltonian takes the form:

$$\hat{H}(\mathbf{q}) = \sum_\lambda \hbar\omega_\lambda(\mathbf{q}) \left(\hat{a}_\lambda^+(\mathbf{q}) \hat{a}_\lambda(\mathbf{q}) + \frac{1}{2} \right) \quad (2.32)$$

$$= \sum_\lambda \hbar\omega_\lambda(\mathbf{q}) \left(\hat{n}_\lambda(\mathbf{q}) + \frac{1}{2} \right) \quad (2.33)$$

$\hat{n}_\lambda(\mathbf{q})$ is the population of phonons with wave vector \mathbf{q} in the λ^{th} mode.

2.3 Third Order Lattice Anharmonicity

From the expansion of the total interatomic potential energy of a crystal in terms of atomic displacements, all terms of order 3 or higher are associated with the anharmonicity of the lattice. The third order lattice anharmonicity is the leading term that causes a perturbation to the harmonic lattice vibrations and anharmonicity induced phonon-phonon scattering.

Recall from 2.3 that we defined the third order lattice anharmonicity tensor as:

$$A_{\alpha i, \beta j, \gamma k}(\ell, \ell', \ell'') = \left(\frac{\partial^3 V}{\partial x_{\alpha, i}(\ell) \partial x_{\beta, j}(\ell') \partial x_{\gamma, k}(\ell'')} \right) \quad (2.34)$$

In reciprocal space the third term in equation 2.3 becomes

$$\begin{aligned}
H_{anh}^{(3)} &= \frac{1}{6} \sum_{\ell,i,\alpha} \sum_{\ell',j,\beta} \sum_{\ell'',k,\gamma} A_{\alpha i, \beta j, \gamma k}(\ell, \ell', \ell'') x_{\alpha, i}(\ell) x_{\beta, j}(\ell') x_{\gamma, k}(\ell'') \\
&= \frac{1}{6} \sum_{q,i,\alpha} \sum_{q',j,\beta} \sum_{q'',k,\gamma} A_{\alpha i, \beta j, \gamma k}(\ell, \ell', \ell'') X_{\alpha, i}(q) X_{\beta, j}(q') X_{\gamma, k}(q'') e^{i(q \cdot \ell + q' \cdot \ell' + q'' \cdot \ell'')}
\end{aligned} \tag{2.35}$$

Let $\mathbf{h} = \boldsymbol{\ell} - \boldsymbol{\ell}''$ ie $\boldsymbol{\ell} = \boldsymbol{\ell}'' + \mathbf{h}$

and $\mathbf{h}' = \boldsymbol{\ell}' - \boldsymbol{\ell}''$ ie $\boldsymbol{\ell}' = \boldsymbol{\ell}'' + \mathbf{h}'$

$$\begin{aligned}
H_{anh}^{(3)} &= \frac{1}{6} \sum_{q,i,\alpha} \sum_{q',j,\beta} \sum_{q'',k,\gamma} \sum_{\ell''} A_{\alpha i, \beta j, \gamma k}(q, q') X_{\alpha, i}(q) X_{\beta, j}(q') X_{\gamma, k}(q'') e^{i(q+q'+q'') \cdot \ell''} \\
&= \frac{1}{6} \sum_{q,i,\alpha} \sum_{q',j,\beta} \sum_{q'',k,\gamma} A_{\alpha i, \beta j, \gamma k}(q, q') X_{\alpha, i}(q) X_{\beta, j}(q') X_{\gamma, k}(q'') \delta_{q+q'+q'',g}
\end{aligned} \tag{2.36}$$

Where

$$A_{\alpha i, \beta j, \gamma k}(\mathbf{q}, \mathbf{q}') = \sum_{\mathbf{h}, \mathbf{h}'} A_{\alpha i, \beta j, \gamma k}(\mathbf{h}, \mathbf{h}', 0) e^{i(\mathbf{q} \cdot \mathbf{h} + \mathbf{q}' \cdot \mathbf{h}')} \tag{2.37}$$

We have $X_{\alpha}(q) X_{\beta}(q') X_{\gamma}(q'')$

$$\begin{aligned}
&= \frac{1}{\sqrt{m_{\alpha} m_{\beta} m_{\gamma}}} \sum_{\lambda, \epsilon, \eta} Q_{\lambda}(\mathbf{q}) Q_{\epsilon}(\mathbf{q}') Q_{\eta}(\mathbf{q}'') e_{\alpha, \lambda}(\mathbf{q}) \cdot e_{\beta, \epsilon}(\mathbf{q}') \cdot e_{\gamma, \eta}(\mathbf{q}'') \\
&= \frac{1}{\sqrt{m_{\alpha} m_{\beta} m_{\gamma}}} \left(\frac{\hbar}{2} \right)^{\frac{3}{2}} \sum_{\lambda, \epsilon, \eta} \frac{e_{\alpha, \lambda}(\mathbf{q}) \cdot e_{\beta, \epsilon}(\mathbf{q}') \cdot e_{\gamma, \eta}(\mathbf{q}'')}{\sqrt{\omega(\mathbf{q}) \omega(\mathbf{q}') \omega(\mathbf{q}'')}} Y_{\lambda \epsilon \eta}(\mathbf{q}, \mathbf{q}', \mathbf{q}'')
\end{aligned} \tag{2.38}$$

Here

$$Y_{\lambda\epsilon\eta} = (\hat{a}_\lambda^+(-\mathbf{q}) + \hat{a}_\lambda(\mathbf{q})) (\hat{a}_\epsilon^+(-\mathbf{q}') + \hat{a}_\epsilon(\mathbf{q}')) (\hat{a}_\eta^+(-\mathbf{q}'') + \hat{a}_\eta(\mathbf{q}'')) \quad (2.39)$$

Using equations 2.38 and 2.39, we have implemented an algorithm to calculate the phonon-phonon scattering rates due to lattice anharmonicity within the single mode excitation approximation (SMEA). The details of the SMEA are reported in chapter 3.

2.4 Real Space Super Cell Calculation of Lattice Dynamics

We developed a real space supercell finite displacement (RSSFD) method to evaluate interatomic potentials up to third order from first-principles. In the RSSFD approach, we displace atoms in a real space super cell by a series of finite displacements and then evaluate harmonic force constants and third order lattice anharmonicity tensor elements from forces obtained via the Hellmann-Feynman (H-F) theorem.

$$F_{\alpha,i}(\ell) = -\frac{\partial E}{\partial u_{\alpha,i}(\ell)} = -\left\langle \Psi \left| \frac{\partial H}{\partial u_{\alpha,i}(\ell)} \right| \Psi \right\rangle \quad (2.40)$$

where α, i is the component of the force and atom index respectively, ℓ is the unit cell index, H is the DFT hamiltonian and Ψ is the electronic ground-state wavefunction.

This technique has been successfully used to predict the full phonon spectrum of many materials^{78,79,85,101,112–117}. The computational cost of the RSSFC method depends on the size of supercell and the range of interatomic force constants. For ionic solids, the effect of induced Born effective charges due to lattice vibrations is often added as a correction to the phonon spectrum. Also referred to as LO-TO splitting, this often requires a separate calculation following a method proposed by Kunc and Martin¹¹⁸.

Our RSSFD technique involves two types displacement schemes: The first scheme which we call irreducible single atom displacement (ISAD) involves displacement of single atoms based on crystal symmetry, to determine the H-F forces needed to derive the harmonic force constants. The second algorithm called irreducible paired atom displacement (IPAD) involves the displacement of atoms in pairs, to determine the H-F forces needed to evaluate the third order lattice anharmonicity tensors. The details of the ISAD are reported here¹¹⁹. In this section I will describe the IPAD algorithm for the calculation of the third order lattice anharmonicity tensor $A_{\alpha i, \beta j, \gamma k}(\ell, \ell', \ell'')$.

In our IPAD scheme, we displace a pair of atoms simultaneously by a finite amount Δ which is much smaller than the interatomic distance. For example if we displace the j^{th} atom in β direction and the k^{th} atom in γ direction by (Δ, Δ) , $(\Delta, -\Delta)$, $(-\Delta, \Delta)$, and $(-\Delta, -\Delta)$,

respectively. The α component of the H-F forces on the i^{th} atom are:

$$\begin{aligned}
F_{\alpha,i}^{++}(\ell) &= -(\varphi_{\alpha i, \beta j}(\ell, \ell') + \varphi_{\alpha i, \gamma k}(\ell, \ell'')) \cdot \Delta \\
&\quad - \frac{1}{2}(A_{\alpha i, \beta j, \beta j}(\ell, \ell', \ell') + A_{\alpha i, \gamma k, \gamma k}(\ell, \ell'', \ell'') + 2A_{\alpha i, \beta j, \gamma k}(\ell, \ell', \ell'')) \cdot \Delta^2 \\
&\quad - \frac{1}{6} \left(\begin{aligned} &B_{\alpha i, \beta j, \beta j, \beta j}(\ell, \ell', \ell', \ell') + B_{\alpha i, \gamma k, \gamma k, \gamma k}(\ell, \ell'', \ell'', \ell'') \\ &+ 2B_{\alpha i, \beta j, \beta j, \gamma k}(\ell, \ell', \ell'', \ell''') + 2B_{\alpha i, \beta j, \gamma k, \gamma k}(\ell, \ell', \ell'', \ell''') \end{aligned} \right) \cdot \Delta^3
\end{aligned} \tag{2.41a}$$

$$\begin{aligned}
F_{\alpha,i}^{+-}(\ell) &= -(\varphi_{\alpha i, \beta j}(\ell, \ell') - \varphi_{\alpha i, \gamma k}(\ell, \ell'')) \cdot \Delta \\
&\quad - \frac{1}{2}(A_{\alpha i, \beta j, \beta j}(\ell, \ell', \ell') + A_{\alpha i, \gamma k, \gamma k}(\ell, \ell'', \ell'') - 2A_{\alpha i, \beta j, \gamma k}(\ell, \ell', \ell'')) \cdot \Delta^2 \\
&\quad - \frac{1}{6} \left(\begin{aligned} &B_{\alpha i, \beta j, \beta j, \beta j}(\ell, \ell', \ell', \ell') - B_{\alpha i, \gamma k, \gamma k, \gamma k}(\ell, \ell'', \ell'', \ell'') \\ &- 2B_{\alpha i, \beta j, \beta j, \gamma k}(\ell, \ell', \ell'', \ell''') + 2B_{\alpha i, \beta j, \gamma k, \gamma k}(\ell, \ell', \ell'', \ell''') \end{aligned} \right) \cdot \Delta^3
\end{aligned} \tag{2.41b}$$

$$\begin{aligned}
F_{\alpha,i}^{-+}(\ell) &= -(-\varphi_{\alpha i, \beta j}(\ell, \ell') + \varphi_{\alpha i, \gamma k}(\ell, \ell'')) \cdot \Delta \\
&\quad - \frac{1}{2}(A_{\alpha i, \beta j, \beta j}(\ell, \ell', \ell') + A_{\alpha i, \gamma k, \gamma k}(\ell, \ell'', \ell'') - 2A_{\alpha i, \beta j, \gamma k}(\ell, \ell', \ell'')) \cdot \Delta^2 \\
&\quad - \frac{1}{6} \left(\begin{aligned} &-B_{\alpha i, \beta j, \beta j, \beta j}(\ell, \ell', \ell', \ell') + B_{\alpha i, \gamma k, \gamma k, \gamma k}(\ell, \ell'', \ell'', \ell'') \\ &+ 2B_{\alpha i, \beta j, \beta j, \gamma k}(\ell, \ell', \ell'', \ell''') - 2B_{\alpha i, \beta j, \gamma k, \gamma k}(\ell, \ell', \ell'', \ell''') \end{aligned} \right) \cdot \Delta^3
\end{aligned} \tag{2.41c}$$

$$\begin{aligned}
F_{\alpha,i}^{--}(\ell) &= +(\varphi_{\alpha i, \beta j}(\ell, \ell') + \varphi_{\alpha i, \gamma k}(\ell, \ell'')) \cdot \Delta \\
&\quad - \frac{1}{2}(A_{\alpha i, \beta j, \beta j}(\ell, \ell', \ell') + A_{\alpha i, \gamma k, \gamma k}(\ell, \ell'', \ell'') + 2A_{\alpha i, \beta j, \gamma k}(\ell, \ell', \ell'')) \cdot \Delta^2 \\
&\quad + \frac{1}{6} \left(\begin{aligned} &B_{\alpha i, \beta j, \beta j, \beta j}(\ell, \ell', \ell', \ell') + B_{\alpha i, \gamma k, \gamma k, \gamma k}(\ell, \ell'', \ell'', \ell'') \\ &+ 2B_{\alpha i, \beta j, \beta j, \gamma k}(\ell, \ell', \ell'', \ell''') + 2B_{\alpha i, \beta j, \gamma k, \gamma k}(\ell, \ell', \ell'', \ell''') \end{aligned} \right) \cdot \Delta^3
\end{aligned} \tag{2.41d}$$

From equation 2.41, simple derivation yields

$$A_{\alpha i, \beta j, \gamma k}(\ell, \ell', \ell'') = \frac{-F_{\alpha,i}^{++}(\ell) + F_{\alpha,i}^{+-}(\ell) - F_{\alpha,i}^{-+}(\ell) + F_{\alpha,i}^{--}(\ell)}{4\Delta^2} \tag{2.42}$$

2.5 Quasi-harmonic Approximation (QHA) and Mode Grüneisen Parameter

Within the harmonic approximation, lattice vibrations are treated as a collection of independent harmonic oscillators. Phonons are quasi-particles that represent the quantized thermal excitations of harmonic lattice vibrations. According to this approximation, phonons do not interact with each other, and they have infinitely large lifetimes. Also, phonon frequencies do not depend on vibration amplitudes and unit cell volumes. i.e. they are temperature and pressure independent. This approximation however, cannot explain several material properties associated with lattice anharmonicity such as small yet finite thermal expansion and finite phonon lifetimes. When anharmonic contributions to the interatomic potentials is small, anharmonic effects in a crystal be evaluated within the framework of the quasi-harmonic approximation(QHA), which still describes inter-atomic potentials within the harmonic approximation, but at the same time, force constant matrices are treated as volume dependent. Consequently, phonon frequencies are volume dependent. The volume dependence of the vibrational frequencies is described by a parameter known as the mode Grüneisen parameter (γ). From QHA theory, γ is defined as follows:

$$\gamma_i(\vec{q}) = -\frac{d \ln \omega_i(\vec{q})}{d \ln V} = -\frac{V}{\omega_i(\vec{q})} \frac{d \omega_i(\vec{q})}{dV} \quad (2.43)$$

By invoking Hellman-Feynman theorem, γ can be expressed in terms of the logarithmic volume derivative of the dynamical matrix

$$\gamma_i(\vec{q}) = -\frac{V}{2\omega_i(\vec{q})^2} \langle \mathbf{e}_i(\vec{q}) | \frac{d\mathbf{D}(\vec{q})}{dV} | \mathbf{e}_i(\vec{q}) \rangle \quad (2.44)$$

Where the dynamical matrix $D(\vec{q})$ is defined in equation 2.24

This expression can be rewritten as follows:

$$\gamma_i(\vec{q}) = -\frac{1}{2\omega_i(\vec{q})^2} \sum_{\alpha\beta} \sum_{kk'} \frac{d\mathbf{D}_{\alpha\beta}(\vec{q})}{d\ln V} \frac{e_i^{*\alpha k}(\vec{q})e_i^{\beta k'}(\vec{q})}{\sqrt{M_k M_{k'}}} \quad (2.45)$$

The mode Grüneisen parameters (γ) are used to quantify the degree of lattice anharmonicity in a crystal because they are determined by the volume dependence of the dynamical matrix $D(\vec{q})$ in reciprocal space or force constants matrix $\varphi(0, \vec{h})$ in real space. According to perturbation theory^{120,121}, the logarithmic volume derivative of the force constants matrix $\varphi(0, \vec{h})$ is directly associated with third order lattice anharmonicity according to equation 2.46

$$\left(\frac{d\varphi(0, \vec{h})}{d\ln V} \right)_{\alpha\beta} = \frac{1}{3} \sum_{\delta} \sum_{\nu\nu'} A_{\alpha\beta\delta}(0, h, h') r_{\delta}(h') \quad (2.46)$$

By combining equations 2.46, 2.45 and 2.24, it is straight forward to show that the mode Grüneisen parameter can be derived from the third order lattice anharmonicity tensors according to equation 2.47

$$\gamma_i(\vec{q}) = -\frac{1}{6\omega_i^2(\vec{q})} \sum_k \sum_{k'h} \sum_{k''h'} \sum_{\alpha\beta\delta} A_{\alpha k 0, \beta k' h, \delta k'' h'}(0, h, h') \frac{e_i^{*\alpha k}(\vec{q})e_i^{\beta k'}(\vec{q})}{\sqrt{m_k m_{k'}}} e^{i\vec{q}\cdot\vec{h}} r_{\delta k'' h'} \quad (2.47)$$

In our first-principle calculation of interatomic potential energy of solids, γ serves as an important internal check on the robustness of our calculated third order lattice anharmonicity tensor (A_{ijk}). This is because unlike phonon frequencies and group velocities which have experimental measurements against which our calculated values can be compared, the third order lattice anharmonicity tensor do not have experimentally measured counterparts. To independently test the reliability of our calculated A_{ijk} data, we evaluate γ first from the calculated dynamic matrices which have been verified to be accurate by comparing with previous measurements and calculations where these exist. Next we evaluate γ_i via the

calculated third order lattice anharmonicity. By comparing γ independently evaluated from the two methods, we can establish the reliability of our A_{ijk} data. This is illustrated in Figure 2.1. Here γ from φ_{ij} and A_{ijk} for MgO are plotted on the same axes. It is observed that the two γ capture the same features. Generally, the quality of the agreement in the two sets of γ reflects the reliability of the calculated third order lattice anharmonicity tensors.

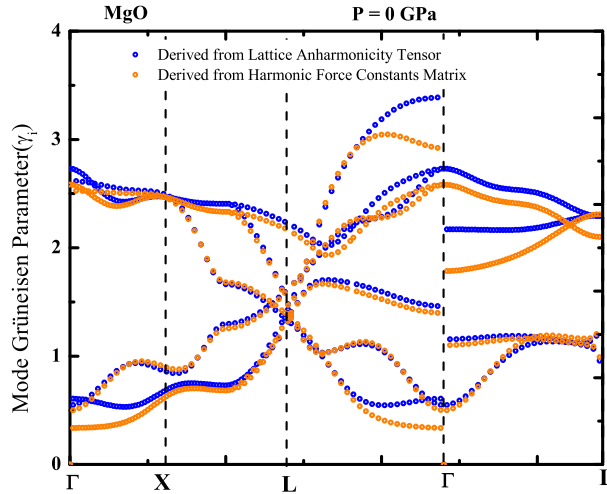


Figure 2.1: Mode Grüneisen Parameter(γ_i) derived from harmonic force constant matrix and third order lattice anharmonicity tensor in MgO compared. Blue circles represent γ from A_{ijk} , orange circles represent γ from φ_{ij} . Both γ s follow the same trend, showing that our calculated A_{ijk} are indeed reliable.

2.6 Vibrational Virtual Crystal Approximation(vVCA)

Lower mantle minerals are not pristine crystals but solid solutions that contain compositional disorder. For example, about 10% of Fe^{2+} or Fe^{3+} exist in perovskite and ferropericlase. Figure 2.2 shows a sketch of differences between 1-dimensional crystals (AO and BO) and 1-dimensional pseudo binary solid solutions, $(A_{1-x}, B_x)O$ where both A and B atoms are randomly distributed at the cation sites. In Figure 2.2, φ_{ij}^{AO} and φ_{ij}^{BO} represent the harmonic force constants in perfect crystals of AO and BO respectively. $\varphi_{ij}^{(SS)}$ represents

the force constants in the disordered mineral solid solution containing a random substitution of cation-A with cation-B. Both φ_{ij}^{AO} and φ_{ij}^{BO} have translational symmetry. But the A/B substitution disorder breaks the $\varphi_{ij}^{(SS)}$ translational symmetry.

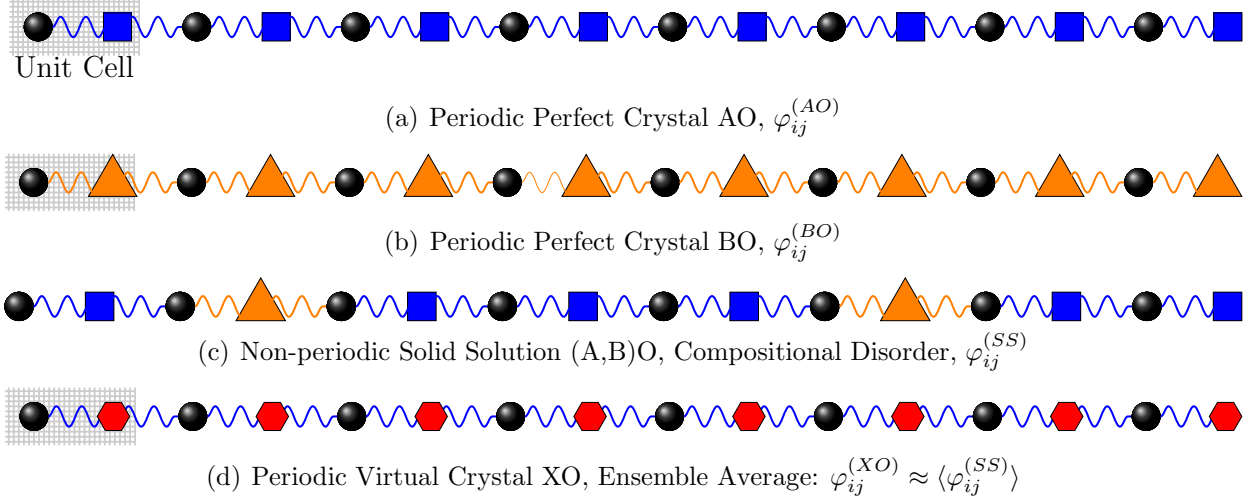


Figure 2.2: Vibrational Virtual Crystal Approximation (vVCA)

An exact solution for the lattice dynamics of mineral solid solutions requires large supercell models. As an approximation, we implemented a vibrational virtual crystal approximation (vVCA). Within the vVCA, we first generate a supercell model with a specific A/B substitution configuration $\varphi_{ij}^{(ss-1)}$. Then we generate all the symmetrically equivalent substitution configurations, and derive their force constant matrices with group theory. $\varphi_{ij}^{(ss-2)}, \varphi_{ij}^{(ss-3)}, \varphi_{ij}^{(ss-4)} \dots$ are derived with $\varphi_{ij}^{(A,B)O} = \varphi_{ij}^{(A_{(1-\delta)}B_{\delta})O}$. We perform a configurational average which represents the force constants in the virtual crystal of XO. Notice that crystalline periodicity is restored in $\langle \varphi_{ij}^{ss} \rangle_{vVCA}$. It is worth pointing out that $\langle \varphi_{ij}^{ss} \rangle_{vVCA}$ is not simply the arithmetic average: $(1-x)\varphi_{ij}^{AO} + x\varphi_{ij}^{BO}$. It includes a much more realistic description of A/B substitution.

This substitution is known to modify the interatomic forces especially in the vicinity of the substitution. In this study we find that the bond modification leads to a softening of phonon frequencies and group velocities, details reported in chapter 6.

CHAPTER 3

PEIRLS-BOLTZMANN TRANSPORT THEORY

3.1 Peierls-Boltzmann Transport Theory (PBTT)

All thermally excitable particles/quasi-particles contribute to heat conduction. In optically thick and electrically insulating solids, the main carriers of heat are phonons, i.e. the quasi-particles that represent quantization of lattice vibrations. At the microscopic level, the kinetic particle theory describes the heat flux according equation 3.1

$$\vec{J} = \frac{1}{N_{\vec{q}}} \sum_{\vec{q}, i} n(\vec{q}, i) \hbar \omega(\vec{q}, i) \vec{v}_g(\vec{q}, i) \quad (3.1)$$

Here, $n(\vec{q}, i)$ represents the phonon occupation (distribution) function of mode (\vec{q}, i) , $\vec{v}_g(\vec{q}, i)$ is the group velocity and $\omega(\vec{q}, i)$ is the phonon frequency. At thermal equilibrium, $n = n^o$, where n^o is the well-known Bose-Einstein equilibrium occupation (distribution) function for phonons:

$$n^o = \frac{1}{e^{\hbar\omega/k_B T} - 1} \quad (3.2)$$

The net heat flux at thermal equilibrium \vec{J}^o is zero:

$$\vec{J}^o = \frac{1}{N_{\vec{q}}} \sum_{\vec{q}, i} n^o(\vec{q}, i) \hbar \omega(\vec{q}, i) \vec{v}_g(\vec{q}, i) = 0 \quad (3.3)$$

According to the Peierls-Boltzmann thermal transport theory, the variation of the phonon distribution function with time can be expressed as:

$$\left(\frac{dn}{dt}\right) = \left(\frac{dn}{dt}\right)_{scattering} \quad (3.4)$$

The total derivative $\left(\frac{dn}{dt}\right)$ contains three terms:

$$\left(\frac{dn}{dt}\right) = \frac{\partial n}{\partial t} + \left(\frac{dn}{dt}\right)_{diffusion} + \left(\frac{dn}{dt}\right)_{field} \quad (3.5)$$

For heat conduction, an external field is absent, i.e. we have $\left(\frac{dn}{dt}\right)_{field} = 0$.

At steady state conditions, $\frac{\partial n}{\partial t} = 0$. Therefore,

$$\left(\frac{dn}{dt}\right)_{diffusion} = \left(\frac{dn}{dt}\right)_{scattering} \quad (3.6)$$

The diffusion term can be expressed as:

$$\begin{aligned} \left(\frac{dn}{dt}\right)_{diffusion} &= \vec{v}_g \cdot \vec{\nabla} n(\vec{r}, \vec{q}, t) \\ &\approx \left(\vec{v}_g \cdot \vec{\nabla} T\right) \frac{\partial n^0}{\partial T} \\ &= \frac{C_v}{\hbar\omega} \left(\vec{v}_g \cdot \vec{\nabla} T\right) \end{aligned} \quad (3.7)$$

where $C_v = \frac{\partial \varepsilon}{\partial T} = \frac{\partial}{\partial T} \left(n^0 + \frac{1}{2}\right) \hbar\omega = \hbar\omega \left(\frac{\partial n^0}{\partial T}\right)$ is the phonon mode heat capacity.

Within the relaxation time approximation (RTA), the scattering term in equation 3.6 can be approximated by equation 3.8

$$\left(\frac{dn}{dt}\right)_{scattering} \approx -\left(\frac{n - n^0}{\tau}\right) = -\frac{\Delta n}{\tau} \quad (3.8)$$

Consequently we have,

$$\frac{\Delta n(\vec{q}, i)}{\tau(\vec{q}, i)} = -\frac{C_v(\vec{q}, i)}{\hbar\omega(\vec{q}, i)} \left(\vec{v}_g(\vec{q}, i) \cdot \vec{\nabla}T \right) \quad (3.9)$$

The heat flux in equation 3.1 can be rewritten as:

$$\vec{J} = \frac{1}{N_{\vec{q}}} \sum_{\vec{q}, i} \left(n^0(\vec{q}, i) + \Delta n(\vec{q}, i) \right) \hbar\omega(\vec{q}, i) \vec{v}_g(\vec{q}, i) \quad (3.10)$$

Using equation 3.3, (where $\vec{J}^0 = 0$) in conjunction with equation 3.9, we can further simplify equation 3.10:

$$\begin{aligned} \vec{J} &= \frac{1}{N_{\vec{q}}} \sum_{\vec{q}, i} \left(-\tau(\vec{q}, i) \frac{C_v(\vec{q}, i)}{\hbar\omega(\vec{q}, i)} \left(\vec{v}_g(\vec{q}, i) \cdot \vec{\nabla}T \right) \right) \hbar\omega(\vec{q}, i) \vec{v}_g(\vec{q}, i) \\ &= -\frac{1}{N_{\vec{q}}} \sum_{\vec{q}, i} C_v(\vec{q}, i) \tau(\vec{q}, i) \left(\vec{v}_g(\vec{q}, i) \cdot \vec{\nabla}T \right) \vec{v}_g(\vec{q}, i) \end{aligned} \quad (3.11)$$

The thermal conductivity tensor κ of a single crystal is defined as:

$$\vec{J} = -\kappa \vec{\nabla}T \quad (3.12)$$

Comparing equation 3.12 with equation 3.10, we can clearly see that:

$$\kappa_{\alpha\beta} = \frac{1}{N_{\vec{q}}} \sum_{\vec{q}, i} C_v(\vec{q}, i) v_g^\alpha(\vec{q}, i) v_g^\beta(\vec{q}, i) \tau(\vec{q}, i) \quad (3.13)$$

We can show that the non-diagonal terms $\kappa_{\alpha\beta} = 0$ for $\alpha \neq \beta$.

The averaged thermal conductivity in a randomly oriented polycrystal is defined as:

$$\kappa = \frac{1}{3} (\kappa_{11} + \kappa_{22} + \kappa_{33}) = \frac{1}{3N_{\vec{q}}} \sum_{\vec{q}, i} C_v(\vec{q}, i) \vec{V}_g(\vec{q}, i)^2 \tau(\vec{q}, i) \quad (3.14)$$

The heat capacity and group velocity are both determined from the phonon spectrum and vibrational density of states of the solid. The challenge in determining κ lies with the evaluation of $\tau(\vec{q}, i)$ from first-principles.

3.2 Phonon Lifetime (τ): Fermi's Golden Rule, Single Mode Excitation Approximation (SMEA), and Scattering Rates Due to Mass Disorder

Phonon relaxation time (RT) is a quantity associated with non-equilibrium transport process. However, in practice, RT is often considered as equivalent to the phonon lifetime which is an equilibrium quantity, because both quantities are related to the rate of phonon scattering. In this dissertation, the phrases “phonon lifetime” and “phonon relaxation time” are used interchangeably.

Inside an insulating crystal, phonons can be scattered by crystalline defects (compositional disorder), grain boundaries or lattice anharmonicity. In the work reported in this dissertation, we considered two types of perturbations to the harmonic lattice dynamics namely: mass disorder (either isotope or Fe/Mg substitution) and intrinsic third order lattice anharmonicity. We neglect phonon scattering due to grain boundary since its contribution is comparably small at room temperature and above. The overall phonon lifetime is obtained from the sum of the scattering rates due to the individual scattering processes according to Matthiessen's rule.

$$(\tau^{-1})_{eff} = (\tau^{-1})_{3-phonon} + (\tau^{-1})_{mass} \quad (3.15)$$

According to Fermi's golden rule based on quantum time dependent perturbation theory, the transition rate (Γ_i^f) from an initial quantum state to the final state $|f\rangle$, under a perturbation ΔH is defined by equation 3.16.

$$\Gamma_i^f = \frac{2\pi}{\hbar} |\langle f | \Delta H | i \rangle|^2 \delta(\varepsilon_f - \varepsilon_i) \quad (3.16)$$

$|i\rangle$ and $|f\rangle$ are the initial and final quantum states with energies ε_i and ε_f respectively. In the case of third order lattice anharmonicity induced phonon scattering, ΔH is the same as $H_{anh}^{(3)}$ defined in equation 2.36. Considering only scattering due to 3-phonon processes, we can rewrite scattering rate equation as follows

$$\frac{\Delta n_i(\vec{q})}{\tau_i(\vec{q})} = - \left(\frac{dn_i(\vec{q})}{dt} \right)_{3-phonon} \quad (3.17)$$

Phonon-phonon scatterings due to third order lattice anharmonicity involves 2 phonons combining into one phonon or one phonon splitting up into two phonons as depicted in figure 3.1. These are commonly referred to as 3-phonon processes.

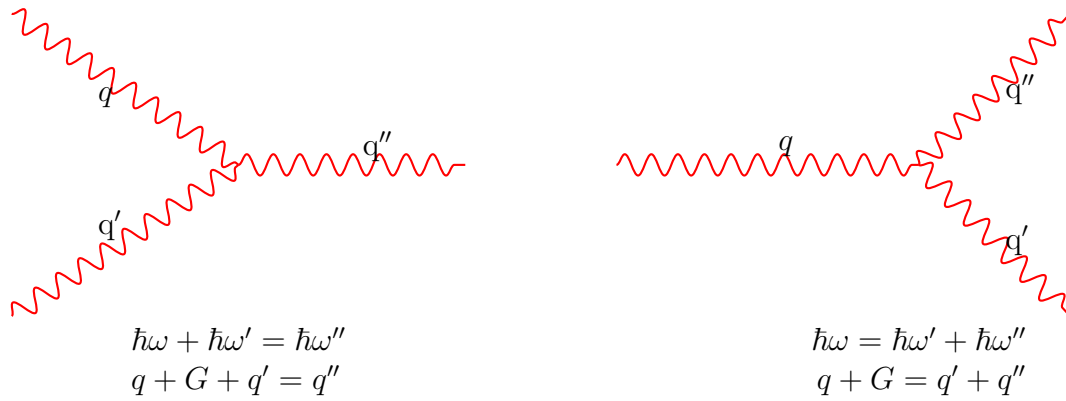


Figure 3.1: Energy and momentum conservation for 3-phonon processes

Based on equation 3.16, 2.36, 2.37, 2.38 and 2.39, we can derive that:

$$\left(\frac{dn_i(\vec{q})}{dt}\right)_{3\text{-phonon}} = \sum_{\vec{q}'} \sum_{\vec{q}''} \left\{ \begin{aligned} & \left[(n_i(\vec{q}) + 1) (n_j(\vec{q}') + 1) (n_k(\vec{q}'')) - (n_i(\vec{q})) (n_j(\vec{q}')) (n_k(\vec{q}'') + 1) \right] S_{\vec{q}, \vec{q}'}^{\vec{q}''} + \\ & \frac{1}{2} \left[(n_i(\vec{q}) + 1) (n_j(\vec{q}')) (n_k(\vec{q}'')) - (n_i(\vec{q})) (n_j(\vec{q}') + 1) (n_k(\vec{q}'') + 1) \right] S_{\vec{q}, \vec{q}''}^{\vec{q}'} \end{aligned} \right\} \quad (3.18)$$

Where $S_{\vec{q}, \vec{q}'}^{\vec{q}''}$ and $S_{\vec{q}}^{\vec{q}', \vec{q}''}$ relate the scattering rates to lattice anharmonicity and phonon spectrum, also enforcing the conservation of energy and momentum.

$$S_{\vec{q}}^{\vec{q}', \vec{q}''} = \frac{\hbar^2}{24^2 \pi N \omega(\vec{q}, i) \omega(\vec{q}', j) \omega(\vec{q}'', k)} \left| \sum_{\alpha\beta\gamma} \frac{A_{\alpha\beta\gamma}(\vec{q}, \vec{q}') e_{\alpha}^i(q) e_{\beta}^j(\vec{q}') e_{\gamma}^k(\vec{q}'')}{(m_{\alpha} m_{\beta} m_{\gamma})^{1/2}} \right|^2 \cdot \delta[\hbar\omega(\vec{q}, i) - \hbar\omega(\vec{q}', j) - \hbar\omega(\vec{q}'', k)] \delta_{\vec{q} - \vec{q}' - \vec{q}'', \vec{g}} \quad (3.19)$$

$$S_{\vec{q}}^{\vec{q}', \vec{q}''} = \frac{\hbar^2}{24^2 \pi N \omega(\vec{q}, i) \omega(\vec{q}', j) \omega(\vec{q}'', k)} \left| \sum_{\alpha\beta\gamma} \frac{A_{\alpha\beta\gamma}(\vec{q}, \vec{q}') e_{\alpha}^i(q) e_{\beta}^j(\vec{q}') e_{\gamma}^k(\vec{q}'')}{(m_{\alpha} m_{\beta} m_{\gamma})^{1/2}} \right|^2 \cdot \delta(\hbar\omega(\vec{q}, i) + \hbar\omega(\vec{q}', j) - \hbar\omega(\vec{q}'', k)) \delta_{\vec{q} + \vec{q}' - \vec{q}'', \vec{g}} \quad (3.20)$$

The single mode excitation approximation (SMEA) assumes that only one phonon mode is displaced out of equilibrium and its phonon occupation number relaxes back to equilibrium while phonon occupation numbers of all other modes maintain their equilibrium value. In terms of the phonon distribution functions, this can be illustrated by equation 3.21

$$\begin{aligned} n_i(\vec{q}) &= n_i^o(\vec{q}) + \Delta n_i(\vec{q}) \\ n_j(\vec{q}') &\approx n_j^o(\vec{q}') \\ n_k(\vec{q}'') &\approx n_k^o(\vec{q}'') \end{aligned} \quad (3.21)$$

After enforcing energy conservation and neglecting terms of order 2 and higher, equation 3.17 can be expressed as:

$$\left(\frac{dn_i(\vec{q})}{dt}\right)_{3\text{-phonon}} = \Delta n_i(\vec{q}) \cdot \sum_{\vec{q}'} \sum_{\vec{q}''} \left\{ \left(n_k^o(\vec{q}'') - n_j^o(\vec{q}') \right) S_{\vec{q}, \vec{q}'}^{\vec{q}''} - \frac{1}{2} \left(n_j^o(\vec{q}') + n_k^o(\vec{q}'') + 1 \right) S_{\vec{q}}^{\vec{q}', \vec{q}''} \right\} \quad (3.22)$$

The scattering rate (the inverse of phonon lifetime) associated with third order lattice anharmonicity can be expressed as:

$$\frac{1}{\tau_{anh}(\vec{q}, i)} = - \sum_{\vec{q}'} \sum_{\vec{q}''} \left\{ \left(n_k^o(\vec{q}'') - n_j^o(\vec{q}') \right) S_{\vec{q}, \vec{q}'}^{\vec{q}''} - \frac{1}{2} \left(n_j^o(\vec{q}') + n_k^o(\vec{q}'') + 1 \right) S_{\vec{q}}^{\vec{q}', \vec{q}''} \right\} \quad (3.23)$$

The temperature independent phonon scattering rate due to mass disorder is given by equation 3.24

$$\Gamma(\vec{q}, i)_{mass} = \frac{2\pi}{\hbar} \left(\frac{\hbar\omega(\vec{q}, i)}{2} \right) \frac{V_0}{8\pi^3} \sum_{i=1}^{3N} \int_{BZ} d\vec{q}' \cdot \left[\delta \left\{ \hbar\omega(\vec{q}, i) - \hbar\omega(\vec{q}', i') \right\} \sum_{\alpha} g_{\alpha} |e_{\alpha}^*(\vec{q}, i) \cdot e_{\alpha}(\vec{q}', i')|^2 \right] \quad (3.24)$$

Here $g_{\alpha} = \sum_k f_k(\alpha) [1 - m_k(\alpha)/\bar{m}(\alpha)]^2$, $f_k(\alpha)$ is the fraction of k^{th} isotope of atom α that has mass $m_k(\alpha)$, and $\bar{m}(\alpha)$ is the average mass of atom with index α . $e_{\alpha}(\vec{q}, i)$ and $\omega(\vec{q}', i')$ are respectively the eigenvector and frequency of the phonon mode (\vec{q}, i) .

3.3 Numerical Recipe for τ_{anh} Calculation

We outline here the steps for calculating the phonon lifetimes (τ_{anh}) associated with anharmonicity induced phonon scattering. The first step in the calculation of τ_{anh} is the calculation of the harmonic force constants matrix (φ_{ij}) and third order lattice

anharmonicity tensor (A_{ijk}). This is achieved via our recently developed RSSFD algorithm described in section 2.4. The harmonic force constants matrix is needed to determine the phonon frequencies which are necessary inputs together with the third order lattice anharmonicity tensor for the calculation of the 3-phonon coupling (TPC) terms ($S_{\vec{q}, \vec{q}'}^{\vec{q}''}$ and $S_{\vec{q}, \vec{q}''}^{\vec{q}'}$) equations 3.19 and 3.20. A fine sampling grid for the calculation of the phonon spectrum and TPC terms is adopted based on numerically converged results. Group symmetry analysis is next performed to determine which of the \vec{q} -points in the sampling grid are irreducible. We save this in a file called *Q-list*. The number of irreducible q-points based on $16 \times 16 \times 16$ and $8 \times 8 \times 6$ sampling grids for MgO and PV-MgSiO-3 calculation are 145 and 100 respectively. The phonon lifetime is then directly evaluated at these \vec{q} -points. To take advantage of parallel computing technology, we have divided our calculation of τ_{anh} into two steps that are embarrassingly parallel. First we calculate the TPC terms at the irreducible \vec{q} -points in the sampling grid are irreducible. We save this in a file called *Qlist*. The phonon lifetime is then directly evaluated at these \vec{q} -points, using our SMEA based code *TPC.f90*. The inputs to this code are:

- List of the irreducible \vec{q} -points in the sampling grid.
- third order lattice anharmonicity tensor
- phonon frequencies (ω_i)
- masses of constituent atoms

The next step is to read the precalculated TPC terms and evaluate the scattering rates at given temperatures, enforcing the conservation of energy and momentum over a finer sampling grid. This is accomplished by using a code named *TauSMEA.f90*. The inputs to this code are:

- List of the irreducible \vec{q} -points in the sampling grid.

- The number of temperature points
- The dimensions of the sampling grid adopted in TPC calculation
- The phonon frequencies calculated over the fine grid
- A finer grid parameter for enforcing energy and momentum conservations
- A file containing the temperature points

The phonon scattering rates in the whole Brillouin zone are then reconstructed using group theory based on the crystal symmetry. We combine this with the temperature independent scattering rates from mass disorder to obtain the overall phonon scattering rate.

CHAPTER 4

LATTICE THERMAL CONDUCTIVITY OF α - Al_2O_3 CRYSTAL

4.1 Introduction

Alumina (Al_2O_3) is a well-known ceramic material with a wide range of technological applications due to its outstanding mechanical and optical properties. Alumina constitutes nearly 15% of minerals in the Earth’s crust and is thus a material of geophysical interest. Its unique blend of low thermal expansion and high compressive strength makes it suitable for use in thermal shock applications. Few chemicals attack alumina making it a good candidate for chemical barrier coatings Alumina shows good electrical insulation at high temperatures, good wear resistance and is very hard At ambient conditions, Al_2O_3 crystallizes in the corundum structure (α - Al_2O_3 , space group $R\bar{3}C$). Experimental^{88,122–124} and theoretical^{71,73,76,125,126} studies show that α - Al_2O_3 is stable up to 90 GPa. The space group, formula units per primitive unit cell Z and Wyckoff sites of α - Al_2O_3 are summarized in table 4.1.

Table 4.1: Space groups, formula units per primitive unit cell Z and Wyckoff sites of α - Al_2O_3 :

Phase	Space group	Z	Species	Wyckoff site
α	$R\bar{3}c$	2	O	6e
			Al	4c

Thermal conductivity of Corundum-structured Al_2O_3 has been studied experimentally^{127–129} however experimental and theoretical data on the pressure and dependence of phonon lifetimes are lacking. We have developed a first-principles computational technique to calculate the lattice thermal conductivity of solids at extreme

pressure and temperature conditions. Our technique has been successfully adopted to study two-atom cubic MgO^{101,112}. We present here our first-principles calculation of lattice thermal conductivity of the trigonal corundum phase of Alumina (Al₂O₃) (Ten atoms per unit cell). We directly evaluated the phonon-phonon scattering rates using our calculated third order lattice anharmonicity tensors, within the framework of quantum scattering theory. Combining this with our calculated vibrational phonon frequencies and group velocities, within the framework of the Boltzmann transport theory we predict the lattice thermal conductivity of α -Al₂O₃ at six different densities and ten temperature points ranging from 300K- 2500K, corresponding to a total of 60 T-P configurations without any empirical fitting. The motivation of the current work is to test the applicability of our newly developed computational technique on a more complex material system like α -Al₂O₃ with 10 atoms per unit cell. To our knowledge this is the first ab initio study of the volume/density dependence of individual phonon mode lifetimes, mode group velocity and mode heat capacity. By combining this with the calculated thermal EOS of α -Al₂O₃, we derive the pressure dependence of lattice thermal conductivity in α -Al₂O₃ depicted in figures 4.12 and 4.13.

4.2 Lattice Dynamics and Equilibrium Thermal Properties

4.2.1 Symmetry Analysis and First-principles Calculation of Total Energies

Symmetry Analysis and Computational Time

To calculate the harmonic force constants and third order lattice anharmonicity tensors, 10-atom unit cells of volumes ranging from 75 -90 Å³ were first relaxed to their ground state. The independent interatomic force constants (Φ_{ij}) and third order lattice anharmonicity tensors (A_{ijk}) for 120-atom supercells were then determined based on group symmetry

analysis. The results of the symmetry analysis to determine the independent terms is summarised in the table 4.2.

Table 4.2: Irreducible atomic displacements (number of total energy calculations required), Independent and dependent Φ_{ij} and A_{ijk} terms from crystal symmetry.

	Irreducible moves	Independent terms	Dependent terms	Δ
Φ_{ij}	18 (ISAD)	1,441	63,348	0.06 Å
A_{ijk}	5,568 (IPAD)	163,267	7,668,135	0.06 Å

After performing group symmetry analysis, we find that a total of 18 irreducible single atom displacements (ISAD) and 5568 irreducible paired-atom displacement (IPAD) are needed to determine the Hellmann-Feynman (HF) forces required to extract Φ_{ij} and A_{ijk} based on 120-atom periodic supercells. These numbers translate directly into number of VASP^{114,130} calculations to be executed per atom. As you can see, computing the HF forces for the extraction of third order lattice anharmonicity is a formidable task, demanding a total of 5,568 N (N = number of atoms in per supercell) calculations, with N computations requiring $\sim 2,623s$. This is equivalent to 4,058 computational hours or 169 days (5months) if these computations were to be performed in series one after the other. Fortunately, this step is highly parallelised. As a result, depending on the number of available compute nodes, several computations can be performed concurrently. These computations were performed on the Auburn University physics department’s PRISM research cluster, a distributed memory computer system (Beowulf cluster). This cluster is comprised of 128 AMD Athlon MP CPUs. With 128 CPUs running in parallel, the 5568 computations can be distributed across the cluster with 44 computations assigned per CPU. This dramatically reduces the computational time from 5 months to 31 computer hours (~ 1.5 days) and makes the task feasible. HF forces were computed using the RSSFD method described in section 2.4.

Total Energy Calculations

Total energy calculations were performed within the framework of density functional theory (DFT) with a plane wave basis set and plane augmented waves (PAW) method which has been implemented in the VASP code^{114,131}. We adopted the local density approximation (LDA) to handle the exchange and correlation functional. Plane wave basis functions with energies up to 400.00 eV were used for the PAW method. A total energy convergence criterion of 10^{-9} eV was specified, for self-consistent iterations. Monkhorst-Park K-point sampling grids of $6 \times 6 \times 4$ were used for Brillouin zone integrations. The calculated static energy at various unit cell volumes was fitted to 3^{rd} order Birch-Murnaghan EOS. The static EOS parameters are presented in table C.1 in appendix C, together with previous calculations and experimental data for comparison.

Harmonic and Anharmonic Inter-atomic Potentials

Both harmonic and anharmonic inter-atomic potentials were obtained based on the HF forces that were computed for all the irreducible distorted 120-atom supercell models using a single Brillouin zone center q-point sampling grid. We next interpolated the calculated independent Φ_{ij} and A_{ijk} over the calculation volumes. Figures 4.1 and 4.3 show the irreducible LDA calculated density dependent harmonic and anharmonic lattice dynamics of Al_2O_3 based on a 120-atom super cell model. Harmonic force constants are obtained using a irreducible single-atom displacement (ISAD) algorithm. Third order lattice anharmonicity tensors are extracted using a irreducible paired-atom displacement (IPAD) scheme described in section 2.4. Both results suggest a nearly linear density dependence of harmonic force constants and third order lattice anharmonicity tensors. The volume dependence of the inter-atomic potentials enables us to predict the inter-atomic potentials for any arbitrary volume within our calculation range without the need to perform a separate VASP calculation as explained in appendix B.

4.2.2 Quasi-harmonic Phonons

Phonon frequencies are obtained by solving equation 2.23. To account for the correction to the dynamical matrix resulting from LO-TO splitting, we performed a separate calculation according to Kunc and Martin’s method¹¹⁸. In a purely harmonic system, the inter-atomic potentials are volume independent as well as the phonon frequencies. Figure 4.1 showing our LDA calculated 2^{nd} order inter-atomic force constants, clearly reveals a volume dependence. in the limit of small deviations from the equilibrium volume, this anharmonic behavior can be approximated via the quasi-harmonic approximation (QHA). Within the QHA, the crystal is considered harmonic at fixed volumes, while the phonon frequencies become volume dependent. This volume dependence is described via the mode Grüneisen parameter (γ) defined by equation 2.43 in section 2.5. In this calculation, the static energy was fitted to the 3^{rd} -order Birch-Murnaghan equation of state (BM-EOS) and the thermal free energy was fitted to the 2^{nd} -order BM-EOS. $F(T, V) = E_{static}(V) + F_{vib}(T, V)$. Our calculated zero pressure thermal expansion coefficient (TEC) of α -Al₂O₃ as a function of temperature using PAW method are compared with former measurements in figure C.2.

Figure 4.2 shows our calculated vibrational phonon frequencies, density of states and group velocities at 0 GPa and 300K. Experimental data (discrete symbols) is included for comparison. The overall agreements between our LDA + PAW calculated vibrational phonon frequencies and experiment, are good and within the typical accuracy of *ab initio* calculations. Among the calculated 30 phonon branches, the low-frequency (acoustic) ones have steeper slopes implying larger phonon mode group velocities ($V_g = \frac{d\omega}{dK}$). This suggests that acoustic phonon modes are more effective carriers of heat compared with the flat optical modes.

We believe that our LDA calculated phonon dispersions are reliable based on the excellent agreement with measurements from experiment as shown in figure 4.2. The calculated lattice anharmonicity tensors on the other hand are not known to have measured

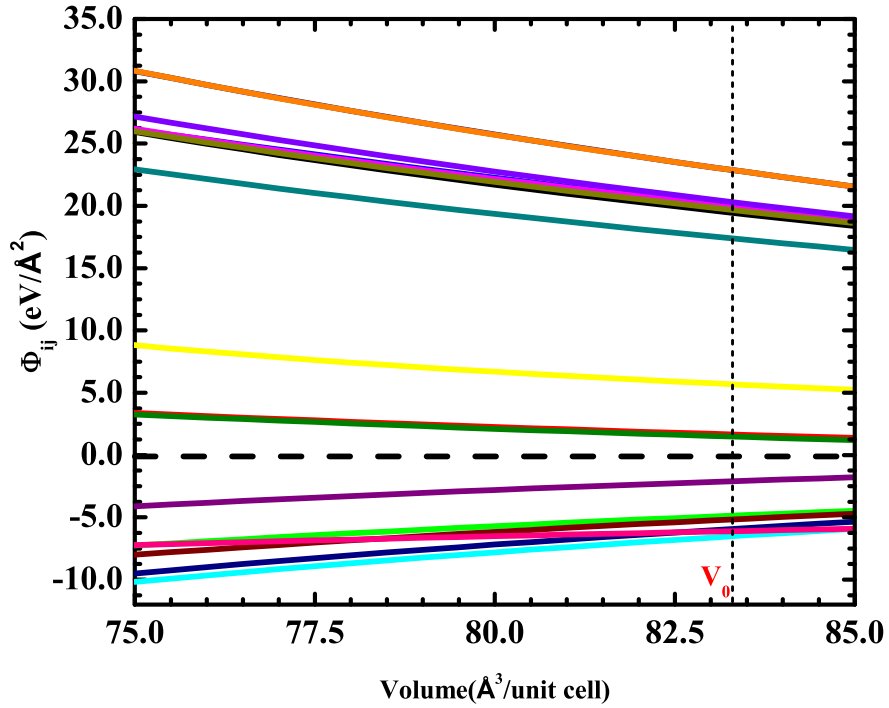


Figure 4.1: LDA calculated density dependent harmonic force constants of Al_2O_3 based on a 120-atom super cell model. A total of 1441 independent Φ_{ij} were extracted from the HF forces from VASP calculation. Majority of the Φ_{ij} terms are small and insensitive to volume change. Less than 20 inter-atomic force constants have magnitudes exceeding $5 \text{ eV}/\text{\AA}^2$ and show an almost linearly increasing pressure dependence with increasing pressure.

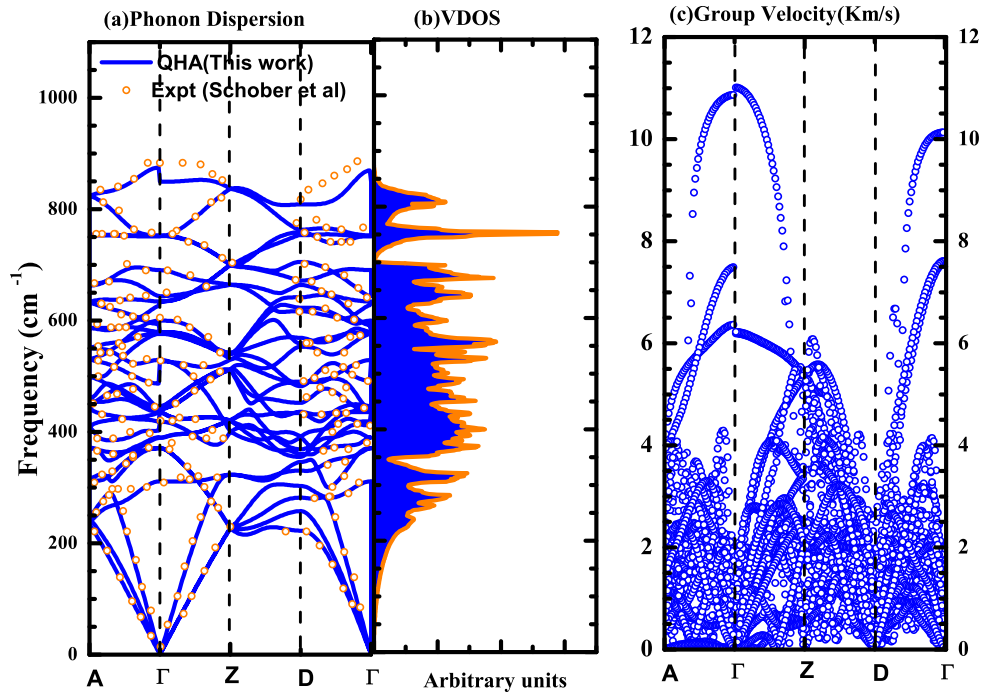


Figure 4.2: Vibrational phonon frequencies and density of states. Our LDA calculated phonon spectrum (solid lines) agree well with measurements from experiment (discrete symbols). Low frequency(acoustic) phonon modes have steeper slopes (group volocities) compared to the high frequency (optical) modes which are mostly flat.

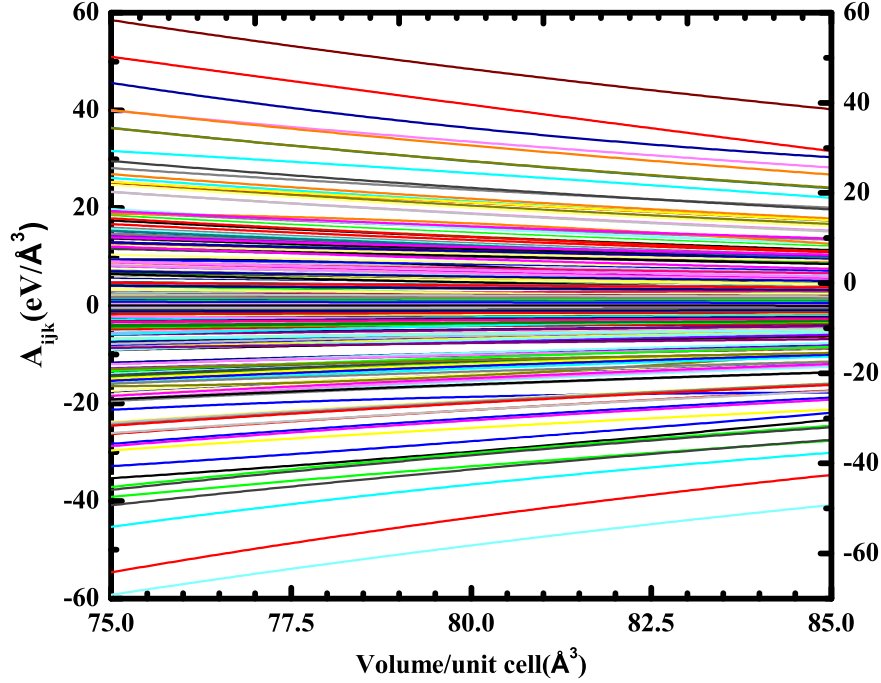


Figure 4.3: Pressure dependence of anharmonicity tensor elements (A_{ijk}). A_{ijk} elements are observed to vary linearly with volume/density. From 0 GPa ($\sim 84 \text{ \AA}^3$) to 50 GPa ($\sim 75 \text{ \AA}^3$), A_{ijk} increases linearly from 40 eV/\AA^3 to 60 eV/\AA^3 , representing a 50% increase, $\sim 1\%$ per GPa.

counterparts. To verify their robustness, we evaluate mode Grüneisen parameters using the extracted lattice anharmonicity and compared with the ones evaluated from the already verified harmonic force constants. The comparison of the mode Grüneisen parameters is shown in figure 4.4. Both mode Grüneisen dispersion plots capture the same features, showing that our calculated lattice anharmonicity tensors are indeed reliable. The process of extracting the mode Grüneisen parameters from Φ_{ij} and A_{ijk} is described in section 2.5

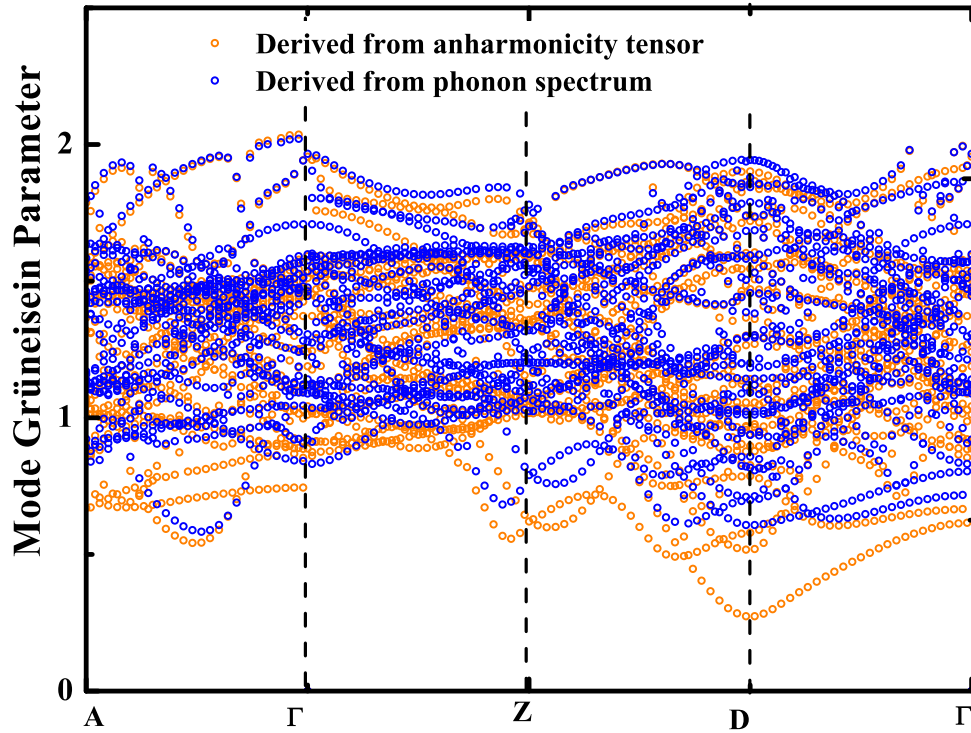


Figure 4.4: Mode Grüneisen Parameters calculated from the force constants matrix(blue circles) and from the third order anharmonicity tensors(orange circles) compared . We use this information to independently test the reliability of our calculated third order anharmonicity tensors. The extraction of Grüneisen Parameters from third order lattice anharmonicity is described in section 2.5

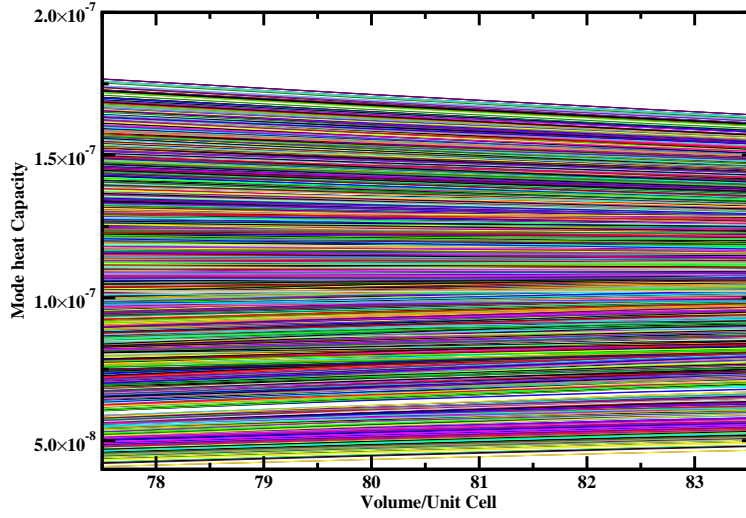


Figure 4.5: Volume dependence of mode heat capacity. Lines represent the heat capacity of individual phonon modes at the sampled at the irreducible K-points in Brillouin zone at 6 different densities/unit cell volumes.

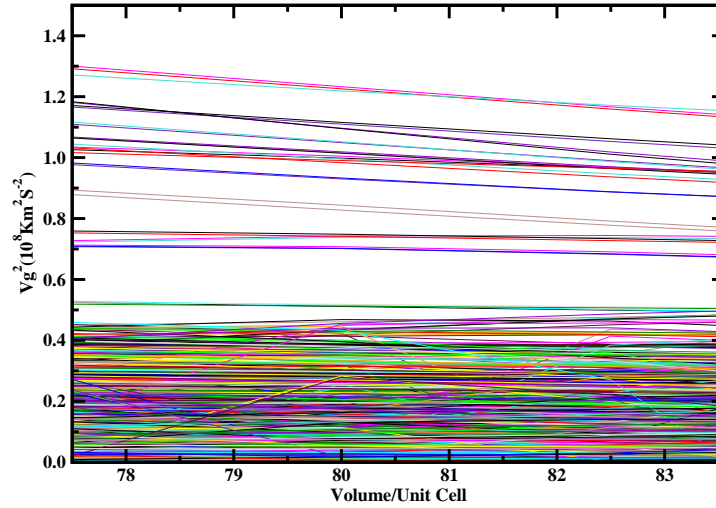


Figure 4.6: Volume/density dependence of square of phonon mode group velocities. Vg^2 shows a mild volume dependence. Remember that according to kinetic transport theory, lattice thermal conductivity is given by $(\kappa = \frac{1}{3} \sum C_v v_g^2 \tau)$

4.3 Phonon Lifetimes

Phonon lifetimes are evaluated based on an $8 \times 8 \times 8$ k-point grid for a total of 512 k-points, 150 of which are irreducible. Using a 10-atom unit cell, the life times of the 30 phonon modes are evaluated at each k-point using Fermis golden rule (equation 3.16). The full life times are obtained using the symmetry relations between the irreducible k-points and the dependent ones. Figure 4.7 shows the lifetimes of the phonon modes at all the 150 irreducible k-points in Brillouin zone.

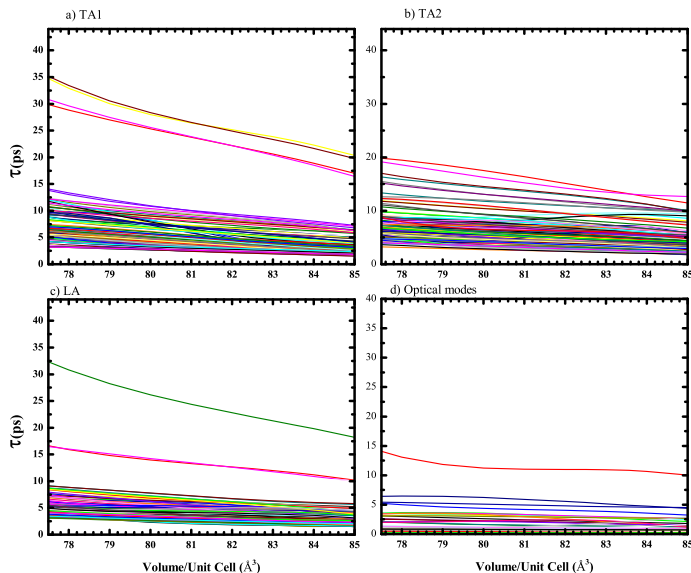


Figure 4.7: Density Dependence of phonon lifetimes in α - Al_2O_3 the at 300K (a) & (b) Transverse acoustic modes (c) Longitudinal acoustic phonon mode; (d)Optical phonon modes. Lifetimes of optical phonon modes are almost pressure insensitive. Acoustic modes increase almost linearly with decreasing volume (increasing pressure). The optical phonon mode with the longest lifetime is only about half the lifetime of the longest acoustic mode. This singles out acoustic phonons as the dominant carriers of heat in α - Al_2O_3 .

4.4 Lattice Thermal Conductivity κ

The inverse of thermal conductivity of Al_2O_3 scales linearly with temperature at constant density, figure 4.10. The thermal conductivity shown, includes the contributions from anharmonicity induced phonon scattering and isotope-induced phonon scattering up to lower mantle temperatures. Our calculated $\kappa(T)$ at ambient pressure figure 4.12, is in good agreement with measurements from experiment¹²⁷⁻¹²⁹. At 0 GPa and 300 K we predict κ as $\sim 23 \text{ Wm}^{-1}\text{K}^{-1}$ at and $56 \text{ Wm}^{-1}\text{K}^{-1}$ at 50 GPa and 300 K, representing a factor of 2.4 increase in κ per

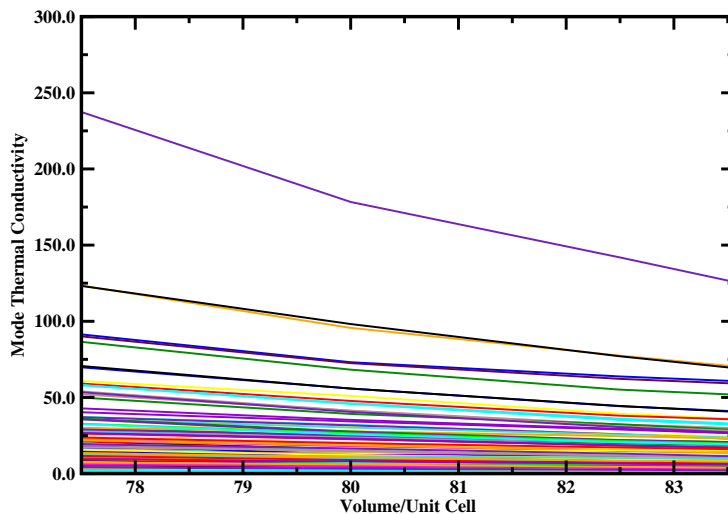


Figure 4.8: Density dependence of mode- κ from acoustic phonon modes at $T= 300\text{K}$. Acoustic modes thermal conductivity follows a volume dependence identical to that of the acoustic modes phonon lifetimes shown in figure 4.7 a, b & c. This is expected as the other determining variables in the thermal conductivity equation C_v and V_g^2 , figures 4.5 and 4.6 are almost flat(volume insensitive)

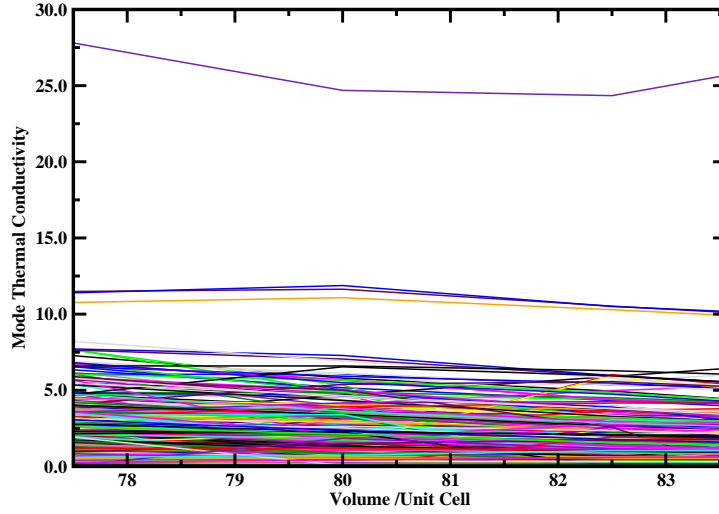


Figure 4.9: Density dependence of mode- thermal conductivity from optical phonon modes at $T= 300\text{K}$. $\kappa_{optical}$ is almost pressure insensitive, consistent with the pressure dependence of $\tau_{optical}$, figure 4.7 d, and C_v and V_g^2 , (figures 4.5 and 4.6)

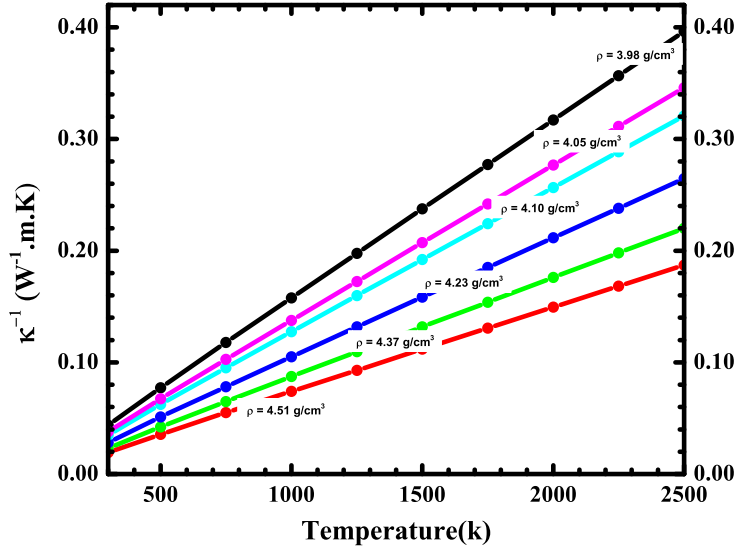


Figure 4.10: Density dependence of κ^{-1} . We have directly calculated the lattice thermal conductivity of $\alpha\text{-Al}_2\text{O}_3$ at six densities ranging from 3.98 gcc^{-1} to 4.51 gcc^{-1} and at 10 different temperature points from 300K to 2500K . κ^{-1} shows a linear temperature dependence at constant density. At constant temperature κ^{-1} increases almost linearly with increasing density.

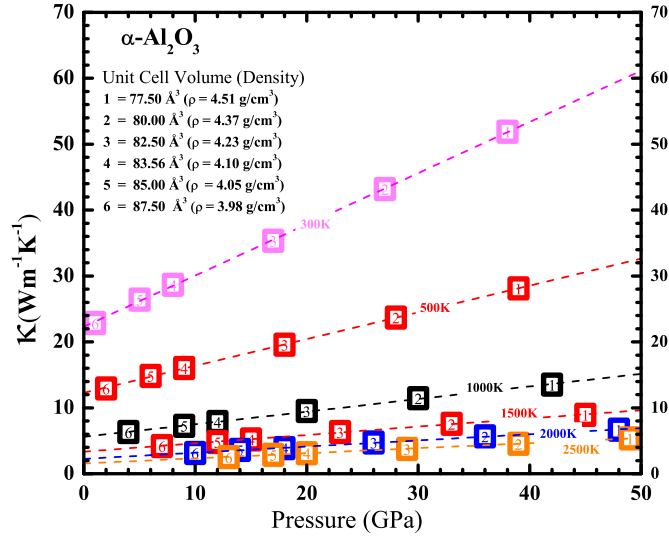


Figure 4.11: Pressure dependence of isothermal κ . Based on the $V(T, T)$ dependence from our LDA calculated thermal EOS we have derived the pressure dependence of κ . The numbers 1-6 represent the six unit cell volumes (densities) for which κ was calculated. κ isotherms show a linear pressure dependence. From this pressure dependence, we can derive the temperature dependence of isobaric κ shown in figure 4.12. From the labels 1-6 one can preview the temperature dependence of κ at conditions of constant pressure.

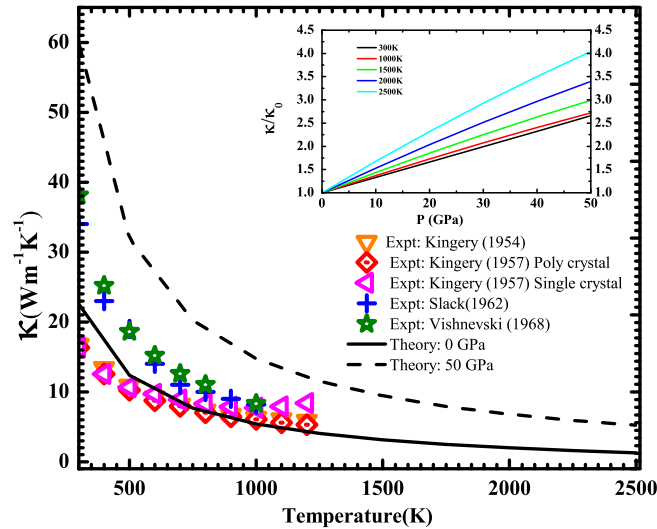


Figure 4.12: Isobaric κ of $\alpha\text{-Al}_2\text{O}_3$ at 0 GPa and 50 GPa. We show a comparison between our calculated thermal conductivity and experiment at 0GPa. Discrete symbols denote experiment data while solid continuous line represent our first-principles calculation.

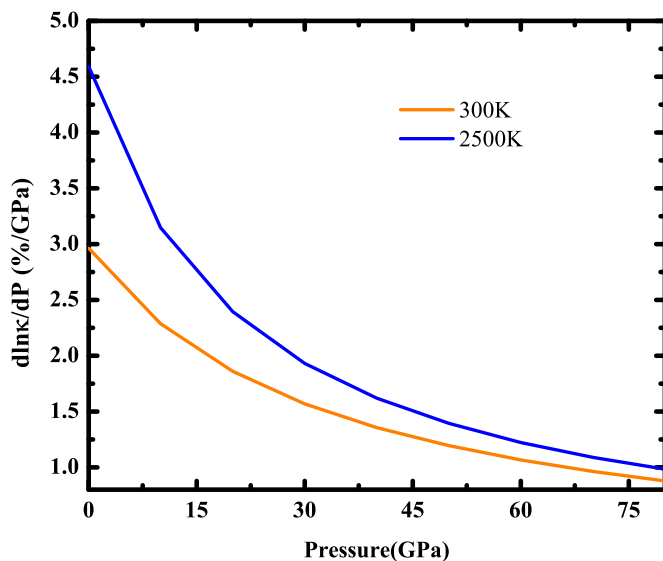


Figure 4.13: Pressure dependence of κ . At 0 GPa, we predict nearly 3 %/GPa and 4.6 %/GPa increase in κ at 300 K and 2500K respectively.

Table 4.3: Calculated lattice thermal conductivity fitted to second order in pressure at 10 different temperatures: $\kappa = a_0 + a_1P + a_2P^2$. The parameters a_0, a_1, a_2 are then used in conjunction with the calculated thermal EOS to predict the isobaric lattice thermal conductivity at different temperatures as shown in figure 4.12

T	a_0 ($\text{Wm}^{-1}\text{K}^{-1}$)	a_1 ($\text{Wm}^{-1}\text{K}^{-1}\text{GPa}^{-1}$)	a_2 ($\text{Wm}^{-1}\text{K}^{-1}\text{GPa}^{-2}$)
300K	22.544	0.74449	0.00004956
500K	12.372	0.40730	0.00034499
750K	7.6949	0.27119	0.00041005
1000K	5.4235	0.20468	0.00035945
1250K	4.0608	0.16568	0.00032107
1500K	3.1491	0.13990	0.00028940
1750K	2.4901	0.12191	0.00026943
2000K	1.9958	0.10818	0.00024826
2250K	1.6059	0.097737	0.00023343
2500K	1.2890	0.089519	0.00022246

4.5 Conclusion

The density dependent harmonic and anharmonic inter-atomic potentials in α -Al₂O₃ are calculated using our supercell finite-displacement algorithm. Phonon frequencies and the thermal equation of state derived from the harmonic force constants are in excellent agreement with experiment. Our LDA calculated 3rd order lattice anharmonicity has been independently tested to be reliable via the mode Grüneisen parameters. Phonon life times for individual phonon modes are directly evaluated based on quantum phonon scattering theory. Acoustic phonon modes are found to have noticeably longer lifetimes compared to the optical modes. Moreover the lifetimes of the acoustic modes increase almost linearly with pressure while the optical modes are almost insensitive to pressure change. In α -Al₂O₃ the acoustic phonon modes contribute about 60% of the total thermal conductivity at ambient conditions. Lattice thermal conductivity of 60 T-P conditions are derived without any empirical extrapolation for a material with 10-atoms per unit cell. Our predicted κ at ambient conditions is about 23 Wm⁻¹K⁻¹, in good agreement with available experiment. $\frac{d \ln \kappa}{dP}$, the pressure dependence of κ is around 3 and 5% per GPa at 0GPa for 300K and 2500K respectively.

CHAPTER 5

LATTICE THERMAL CONDUCTIVITY OF PV-MgSiO₃ AT LOWER MANTLE CONDITIONS

5.1 Introduction

MgSiO₃ is known to exist in two phases, the perovskite(PV) and post-perovskite (PPV) phases. The PV → PPV transition is reported to occur at 125GPa and 2500K¹³². The study of *MgSiO₃* has attracted much attention since the discovery of the PV → PPV transition which is believed to explain the seismic discontinuities observed in the Earth's D'' layer⁷². The raman spectrum of PV and PPV-MgSiO₃ has been studied theoretically¹³² and experimentally¹³³. PV-MgSiO₃ has an orthorhombic structure with the symmetry group #62 *Pnma* and is believed to be thermodynamically stable up to 110 GPa at 0K^{72,132}. PPV-MgSiO₃ the high pressure phase of MgSiO₃ belongs to the *Cmcm* symmetry group and has 2 formula units per unit cell. The Space groups, formula units per primitive unit cell Z and Wyckoff sites for the two phases are summarised in table 5.1

Table 5.1: Space groups, formula units per primitive unit cell Z and Wyckoff sites of 2 polymorphs of MgSiO₃: perovskite and post-perovskite.

Phase	Space group	Z	Species	Wyckoff site
Perovskite	<i>Pnma</i>	4	Mg	4a
			Si	4c
			O	4c, 8d
Post-perovskite	<i>Cmcm</i>	2	Mg	4a
			Si	4c
			O	4c, 8f

Table 5.2: Irreducible representation of the mode symmetries at Γ -point for the 2 polymorphs of MgSiO_3 : perovskite and post-perovskite.

Phase	Raman active	IR active	Silent
Perovskite	$7A_g + 5B_{1g} + 7B_{2g} + 5B_{3g}$	$10B_{1u} + 8B_{2u} + 10B_{3u}$	$8A_u$
Post-perovskite	$4A_g + 3B_{1g} + 1B_{2g}$	$6B_{1u} + 6B_{2u} + 4B_{3u}$	$2A_u$

Based on group symmetry, the sixty (3 acoustic + 57 optical) in PV and 30 (3+27) phonon modes have the following irreducible representation at the Γ - point summarised in table 5.2.

The Earths lower mantle is mostly composed of magnesium silicate in the perovskite structure (PV- MgSiO_3). A recently published measurement of the thermal conductivity of MgSiO_3 perovskite¹³⁴ disagrees significantly with the only other existent measurement¹⁰⁷ and the measured pressure dependence implies values of 9-12 W/m/K when extrapolated to the core/mantle boundary. The disagreement between the two measured values and the uncertainty in the long extrapolations required to estimate the value of silicate perovskite's thermal conductivity at the pressure and temperature conditions of the lower mantle motivates our first-principles calculations of the phonon behavior of perovskite which governs this materials thermal conductivity at the conditions of the lower mantle. The value of lower mantle thermal conductivity is important to to modeling the total budget inside the earth. Large uncertainties exist in our current estimates of lower mantle thermal conductivity because of the long extrapolations in both temperature (T) and pressure (P) of laboratory measured thermal conductivity of lower mantle minerals at relatively low temperatures and pressures.

5.2 First-principles Calculation of Total Energies, Vibrational Properties and Phonon Lifetimes

The VASP software package^{114,130} was used to calculate the relaxed equilibrium atomic structures, total energies, force constants, and 3rd order lattice anharmonicity tensors using Blöch’s projector augmented wave (PAW) pseudopotential^{135,136} and a plane-wave (PW) basis set within the local density approximation (LDA) to the density functional theory (DFT). The details of LDA-PW calculations are as follows: For the PV-MgSiO₃ phase, structures of 20-atom (10-atom for PPV phase) unit cells of different volumes were first relaxed to their ground state. Independent force constants for 160-atom periodic supercells were then identified by the crystal symmetry. Both harmonic and anharmonic force constants were obtained based on the atomic forces that were computed for all the irreducible distorted supercells using a single Brillouin zone (BZ) center q-point sampling grid. Next, for the PV phase only, the lifetime of each phonon mode was calculated based on the Fermis golden rule equation 3.16. This is the most computational intensive step because all the configurations of three-phonon scattering need to be properly counted. All the phonon modes, acoustic or optic, are calculated using the same numerical approach. No empirical approximations of the frequency or q-point dependence are assumed. In the current study of PV-MgSiO₃, the BZ integration was approximated by a summation over a discrete $8 \times 8 \times 6$ q-grid. A finer $64 \times 64 \times 48$ q-grid was used to interpolate the phonon energies (frequencies) based on the chosen $8 \times 8 \times 6$ q-grid to accurately account for the energy and momentum conservation. The lattice symmetry of the crystals was analyzed, and only the phonon lifetimes of an irreducible set of phonon modes are calculated directly and the rest are reconstructed using the group theory.

5.3 Results

5.3.1 Lattice Dynamics and Related Thermal Properties

Both harmonic and anharmonic force constants were obtained based on the HF forces that were computed for all the irreducible distorted supercells using a single Brillouin zone (BZ) centered q-point sampling grid. show the independent inter-atomic force constants in PV and PPV respectively. Independent force constants shown in figures 5.1 and D.4 for 160-atom periodic supercells were identified by the crystal symmetry and obtained based on the Hellmann-Feynman forces that were computed for all the irreducible distorted supercells using a single Brillouin zone (BZ) centered q-point sampling grid. An atomic displacement of $\Delta = 0.06 \text{ \AA}$ was adopted in our ISAD scheme

Table 5.3: Simulation cell volumes and corresponding pressures for PV-MgSiO₃ calculation T=300 K.

$V_0 (\text{\AA}^3)$	122	127	137	147	157
P (GPa)	119.684	95.264	57.100	29.45	9.211

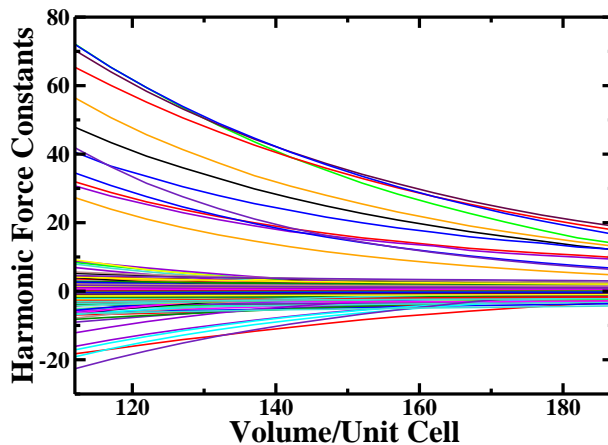


Figure 5.1: Density dependence of harmonic force constants in PV-MgSiO₃. Independent force constants shown for 160-atom periodic supercells of PV.

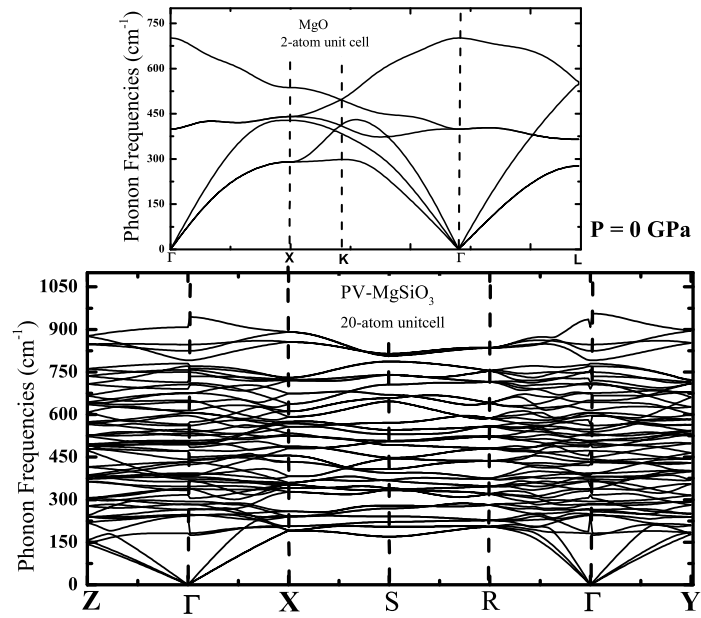


Figure 5.2: LDA calculated phonon mode frequencies in PV-MgSiO₃ and MgO at 0 GPa.

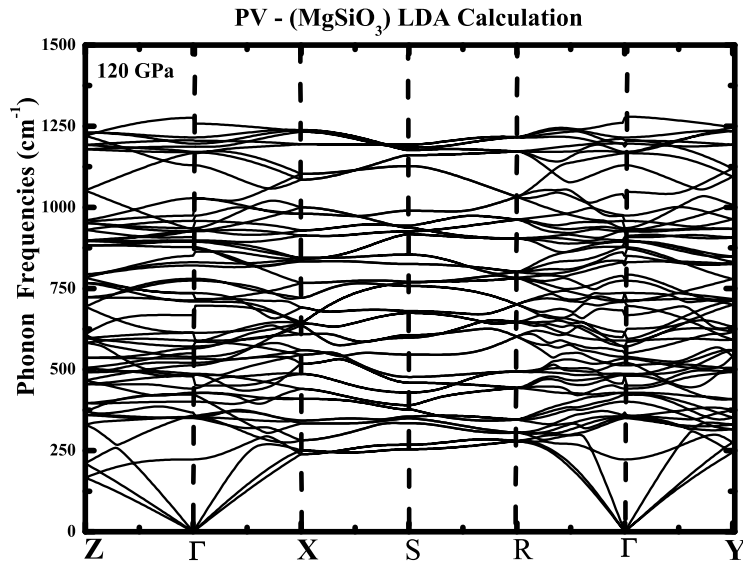


Figure 5.3: LDA calculated phonon mode frequencies in PV-MgSiO₃ at 120 GPa

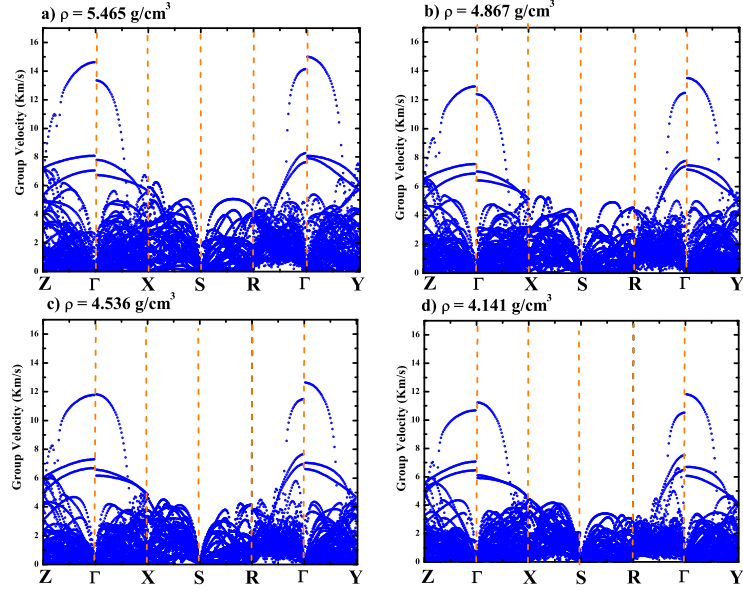


Figure 5.4: LDA calculated phonon mode group velocities in PV-MgSiO₃ at four different densities shown. Group velocities measured along the Z-direction are more sensitive to pressure. From a density of 5.465 g/cm³ (~ 120 GPa) to 4.141g/cm³ (~ 0 GPa) the phonon group velocity in the Γ –Z direction decreases from around 15 km/s to 11 Km/s. Velocities measured in the other high symmetry directions X and Y are almost insensitive to pressure.

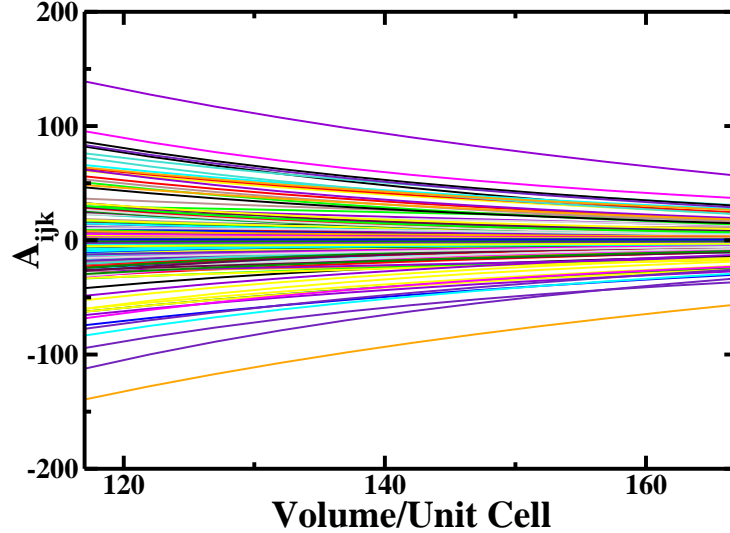


Figure 5.5: Density dependence of 3rd order lattice anharmonicity tensor (A_{ijk}) elements in PV-MgSiO₃. Most A_{ijk} elements vary nearly linearly with volume/density. Most of the elements are very small.

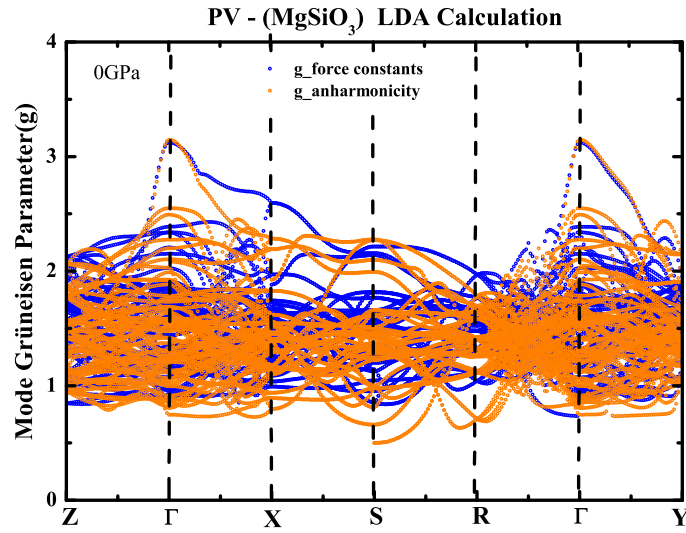


Figure 5.6: Mode Grüneisen parameters in PV-MgSiO₃. Blue circles represent the Mode Grüneisen parameters calculated from the second order force constants while the orange circles show the same parameters calculated via our LDA calculated third order lattice anharmonicity tensors. This step is used to independently test the reliability of our lattice anharmonicity data since A_{ijk} is not known to have measured counterparts to which we can compare our calculated data.

5.3.2 Phonon Lifetimes

The lifetime of each phonon mode was calculated based on the Fermis golden rule equation 3.16. All the phonon modes, acoustic or optic, are calculated using the same numerical approach described in section 5.2. No empirical approximations of the frequency or q-point dependence are assumed. Figures 5.7 show the volume/density dependence of phonon lifetimes of all 60 phonon modes in PV-MgSiO₃ sampled at three high symmetry points of the Brillouin Zone: X ($\frac{\pi}{a}, 0, 0$), Y ($0, \frac{\pi}{b}, 0$) and Z ($0, 0, \frac{\pi}{c}$). The volume dependence of the 60 modes at all the 100 irreducible directions (K-points) of the BZ is reported in appendix E in figures E.1 to E.17. Our calculation reveals a weak pressure dependence of phonon lifetimes. We also observe an almost linear volume dependence.

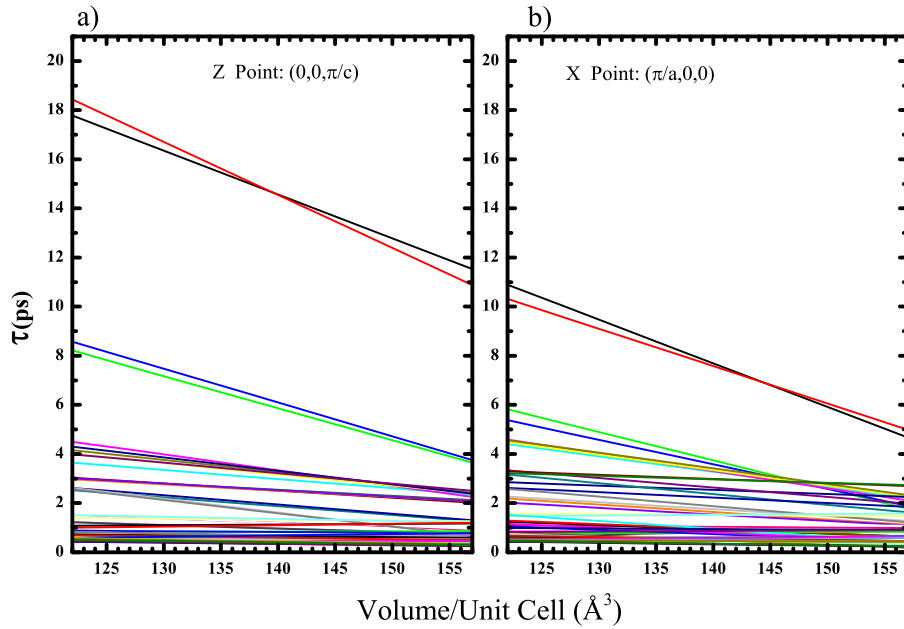


Figure 5.7: Volume/density dependence of phonon lifetimes in PV-MgSiO₃ all 60 modes at two high symmetry points: X ($\frac{\pi}{a}, 0, 0$) and Z ($0, 0, \frac{\pi}{c}$) in the Brillouin Zone

5.3.3 Pressure Dependence of Thermal Conductivity

To predict $\kappa_{Lattice}$ from ambient condition to the pressure-temperature conditions of CMB without extrapolation, we repeated our calculations for 4 density configurations from (5.465 gcm^{-3} to 4.141 gcm^{-3}) at 9 temperature conditions (from 300K to 4000K). The pressures of the studied 36 density-temperature configurations (as listed in Table below are then derived based on the thermal equations of state (EOS) predicted from the first-principles quasi-harmonic theory (QHA)¹¹⁷. Our calculated κ_{PV} at ambient conditions (300K, 0GPa), are 5.70 $\text{Wm}^{-1}\text{K}^{-1}$ and 5.46 $\text{Wm}^{-1}\text{K}^{-1}$ respectively for isotopically pure crystals and natural crystals that contain isotope mass disorder, and are in close agreement with the measurement of 5.1 $\text{Wm}^{-1}\text{K}^{-1}$ by Osako¹³⁴.

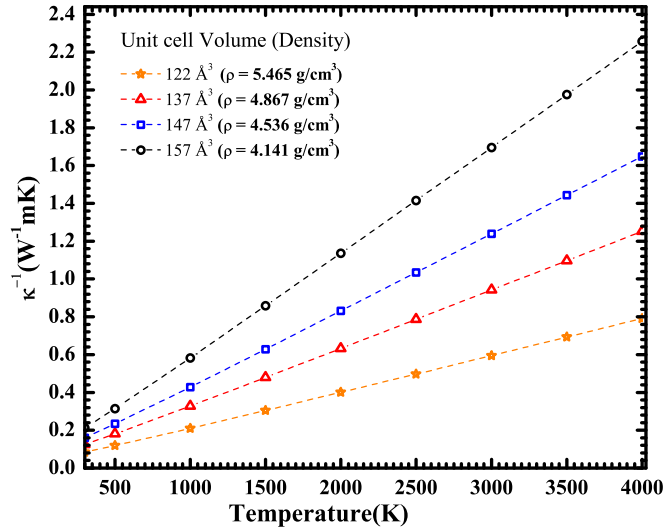


Figure 5.8: Temperature dependence of κ^{-1} in PV-MgSiO₃. κ is calculated at 4 distinct densities corresponding to unit cell volumes shown on the figure, at 9 different temperatures ranging from 300 K to 4000K, for a total of 36 density-temperature configurations. κ is seen to follow the T^{-1} dependence typical of lattice thermal conductivity in insulating materials.

At the bottom of the mantle close to the core/mantle boundary, a phase transformation from the PV to the PPV structure may occur^{137–139}. To assess whether this transformation

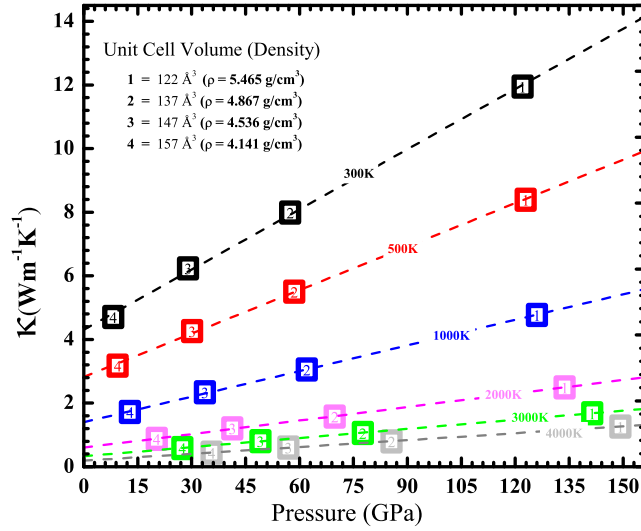


Figure 5.9: Pressure dependence of κ^{-1} in PV-MgSiO₃ at isothermal conditions. This is derived based on the P-V-T relations κ obtained from our LDA calculated thermal EOS.

may influence thermal conductivity in the core/mantle boundary layer, we performed a single calculation of thermal conductivity of a PPV-structured MgSiO₃ at T=3000 K, P =130 GPa, which yields similar values to the MgSiO₃ perovskite structure. Based on our calculations and the materials shared low symmetries, we expect that the difference in the intrinsic κ_{latt} of PV and PPV will be negligible.

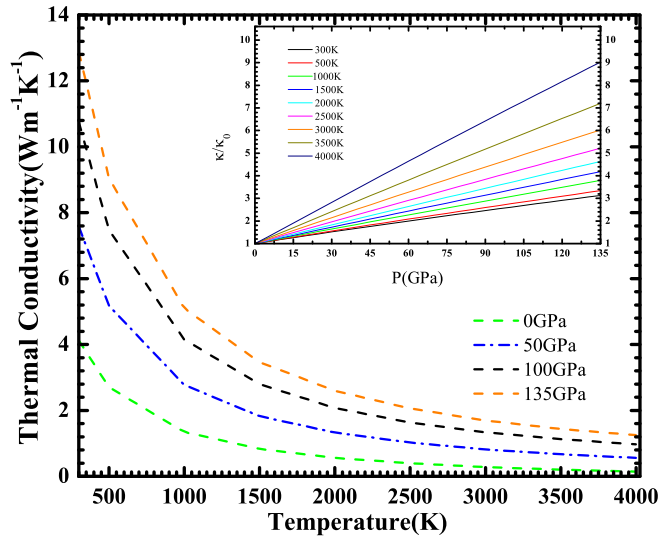


Figure 5.10: Main: Temperature dependence of isobaric κ in PV-MgSiO₃. Inset: Pressure variation of normalized lattice thermal conductivity. Using the coefficients from $\kappa = a_0 + a_1P + a_2P^2$ the isobaric lattice thermal conductivity was derived. Four isobars 0, 50, 100 and 135 GPa are shown. Inset: Pressure variation of normalized κ . κ_0 represents the thermal conductivity at 0 GPa for each isotherm. From 300 K to 4000K, κ/κ_0 increases from 3 to 9 at 135 GPa.

5.4 Discussion

5.4.1 Comparison of the Behavior of κ_{MgO} and κ_{MgSiO_3}

Both κ_{MgO} and κ_{MgSiO_3} follow a T^{-1} dependence at the isochoric condition as expected for insulator thermal conductivity, but the pressure increase of κ_{MgSiO_3} is substantially weaker than that of κ_{MgO} . For example, $\frac{d\ln(\kappa)}{dP}$ at 300 K is 0.25 %GPa⁻¹ for PV, while the same value is ~ 4 % GPa⁻¹ for MgO. This weak pressure-dependence has a strong effect at core/mantle conditions (3000 K, 135 GPa) where κ_{MgSiO_3} is calculated to be ~ 1.64 W/m/K, an order of magnitude smaller than most previous estimates for MgSiO₃¹⁴⁰, and smaller than the calculated value for lattice thermal conductivity of MgO at similar conditions, ~ 40 W/m/K¹⁰¹. The very different lattice thermal conductivities calculated for MgO and MgSiO₃ and their different pressure-dependencies can be understood based on their contrasting phonon behavior interpreted in the context of the kinetic transport theory. According to the Peierls-Boltzmann equation, the bulk lattice thermal conductivity is proportional to the phonon heat capacity, group velocity and lifetime. Of these, the heat capacity plays a lesser role, especially at high temperatures where the heat capacity of each phonon approaches the Dulong-Petit limit 3kB, making little contribution to the differences between thermal conductivity of the two systems. The phonon dispersion curves for the two crystals are also plotted in Figure 5.2. Note that 3 out every 6 phonon modes (50%) are acoustic modes in MgO, while only 3 out of 60 modes (5%) are acoustic modes in PV-MgSiO₃. Acoustic phonon modes, especially those of q-points near the BZ center, behave like classical elastic waves and they usually have large phonon group velocities. In contrast, optic phonon modes can not be approximated with the classical elastic waves and they usually show a much flatter dispersion. In both crystals, low-frequency acoustic phonons (e.g. less than 200 cm⁻¹) are effective heat carriers, while high-frequency optic phonons (e.g. above 700 cm⁻¹) are poor heat carriers. The drastic difference in κ_{latt} of the

two crystals is due to the distinct behaviors of mid-frequency (200 to 700 cm^{-1}) phonons, which are slow optic phonons in PV-MgSiO₃, but much faster acoustic phonons in MgO. The flatter dispersions in PV-MgSiO₃ also likely increase the phonon scattering rates even when the lattice anharmonicity coupling strength remains the same, since more phonon-triplets can simultaneously satisfy the energy and momentum conservation conditions of phonon scattering. As a result, the PV-MgSiO₃ modes have lifetimes nearly one order of magnitude shorter than those in MgO. It is worthy to note that in PV-MgSiO₃, phonon Grüneisen ratios, a parameter that is commonly adopted to quantify lattice anharmonicity, are less than 30% lower than those in MgO; Yet the comparison of the phonon lifetimes shows that the lifetimes of most phonon modes of PV-MgSiO₃ are at least one order magnitude shorter than those of MgO. This result indicates that any empirical models that correlate the Grüneisen ratios and phonon lifetimes are only qualitative at best. Realistic evaluation of phonon lifetimes of individual modes requires an accurate assessment of the number of the conservation-allowed phonon triplets, the anharmonic coupling strengths, and the frequencies of the phonons.

5.5 Conclusions

In summary, we have calculated the harmonic and anharmonic lattice dynamics of PV-MgSiO₃ based on 20-atom unit cells. The density dependence of inter-atomic force constants, phonon group velocities and phonon lifetimes has been studied. Our study reveals a weak pressure dependence of mode group velocities, and the phonon lifetimes of optical modes. Our calculations further demonstrate that the pressure dependence of κ_{latt} is clearly material-dependent, and simple elastic theories are likely insufficient. Many phonon group velocities increase with increasing pressure in both crystals, contributing positively to the pressure dependence of the lattice thermal conductivity. However, acoustic and optic phonons have different pressure dependencies. While the group velocities of acoustic phonon scale approximately as the square root of bulk modulus, there is no simple relation

between elastic properties and the group velocities of optic phonons. Group velocities of some mid-frequency optic modes in PV-MgSiO₃ are found to decrease with increase of pressure, leading to a much complicated pressure dependence of the averaged phonon group velocity. Unlike the high-frequency optic phonons, the mid-frequency optic phonons in PV-MgSiO₃ still have noticeable contribution to the bulk lattice thermal conductivity, and they are largely responsible for the distinct difference in the pressure dependencies of lattice thermal conductivity in the two crystals.

CHAPTER 6

LATTICE THERMAL CONDUCTIVITY OF FERROPERICLASE

6.1 Introduction

Ferropericlasite (fp)- $\text{Mg}_{(1-x)}\text{Fe}_x\text{O}$ is thought to be the second most abundant lower mantle (LM) mineral with nearly 20% of the volume fraction^{141,142}. Its thermal conductivity is important to our understanding of the heat flow across the core-mantle boundary (CMB). Yet, it remains poorly constrained due to the challenges in carrying out measurements at LM conditions. We report here, a direct calculation of the lattice thermal conductivity of fp- $\text{Mg}_{(1-x)}\text{Fe}_x\text{O}$ at lower mantle conditions without any empirical extrapolation. Using our calculated lattice thermal conductivity of Fe-free MgO crystal¹⁰¹ as the starting point, we have evaluated the iron effects on lattice thermal conductivity of fp by calculating the phonon scattering rates due to lattice anharmonicity and Mg/Fe mass disorder within the vibrational virtual crystal approximation (vVCA). We find that phonon scattering due to Fe/Mg mass disorder is significant. Our study based on an iron content of 12.5% shows a significant lowering of lattice thermal conductivity of fp even at the high temperature conditions of the LM. At 3000K and 135GPa we predict the κ of fp to be $11\text{Wm}^{-1}\text{K}^{-1}$ which is nearly 20% of the κ_{MgO} .

6.2 Static Equation of State

The pressure-volume relation was derived using static equation of state (EOS) calculated using the LDA+U technique. Using a unit cell 8 times the size of the 2-atom f.c.c. MgO unit cell, one of the eight Mg atoms was substituted with Fe. The Brillouin zone

integration for electronic energy was calculated using the tetrahedron method over a $8 \times 8 \times 8$ Monkhorst-Pack grid. The calculated energy v.s. volume data shown in figure 6.1 were fitted with a 3^{rd} order BirchMurnaghan EOS. Our calculated EOS parameters are summarised in table 6.1

Our calculated static equation of state agrees well with experiment.

Table 6.1: Static Equation of state of fp-Mg_(1-x)Fe_xO

	V_0 (\AA^3 per atom)	B_0 (GPa)	B'_0
$X_{Fe}=0.00$ (This work: LDA)	9.05	172.7	4.2
$X_{Fe}=0.125$ (This work: LDA+U)	8.85	187.5	4.12
$X_{Fe}=0.17$ (Experiment) ¹⁴³	8.92	186	4.6
$X_{Fe}=0.25$ (Theory GGA+U) ¹⁴⁴	9.37	170	4.1

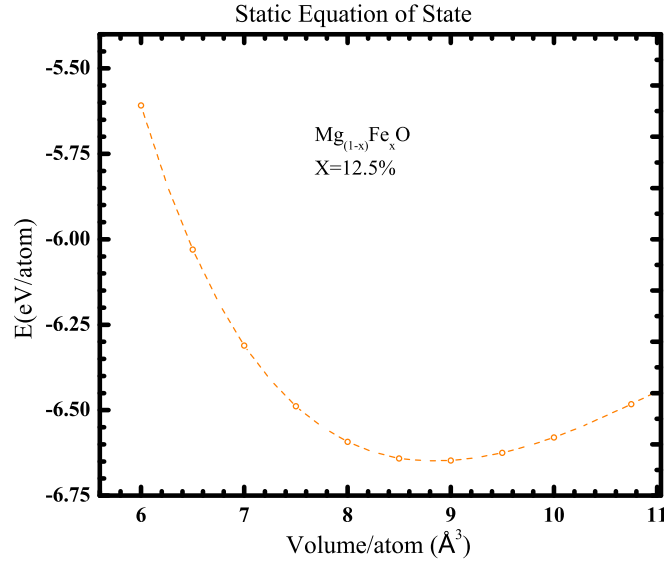


Figure 6.1: Static EOS of ferropericlase fitted to 3^{rd} order BM EOS

6.3 Vibrational Virtual Crystal Approximation of Lattice Dynamics of Ferropericlase

The harmonic and anharmonic lattice dynamics were calculated using our recently developed finite displacement supercell technique¹¹² based on a 128-atom supercell. Atomic forces are derived using the first-principles LDA+U method. The equivalent B1-structured force constants matrices were reconstructed using the vVCA approach described in section 2.6. The cation mass was replaced by the average mass of Fe and Mg in the phonon calculations. We assume that 3rd order lattice anharmonicity tensors are not sensitive to the Fe-content in the dilute limit. Figure 6.2 shows the phonon mode frequencies and group velocities of Fe-free MgO compared to ferropericlase (fp) with 12.5% Fe content calculated based on 128-atom supercell. The black line/symbols shows the result obtained by replacing the mass of Mg in the MgO calculation by the weighted mass $\text{Mg}_{0.875}\text{Fe}_{0.125}$. The blue lines/symbols show the result obtained from the vVCA approach. The overall trend consistently shows softening of phonon mode frequencies and group velocities with increasing Fe content. Based on the similar harmonic lattice dynamics, we assume that the lattice anharmonicity are similar, so we use the Fe-free MgO lattice anharmonicity to evaluate anharmonicity induced scattering rates for fp

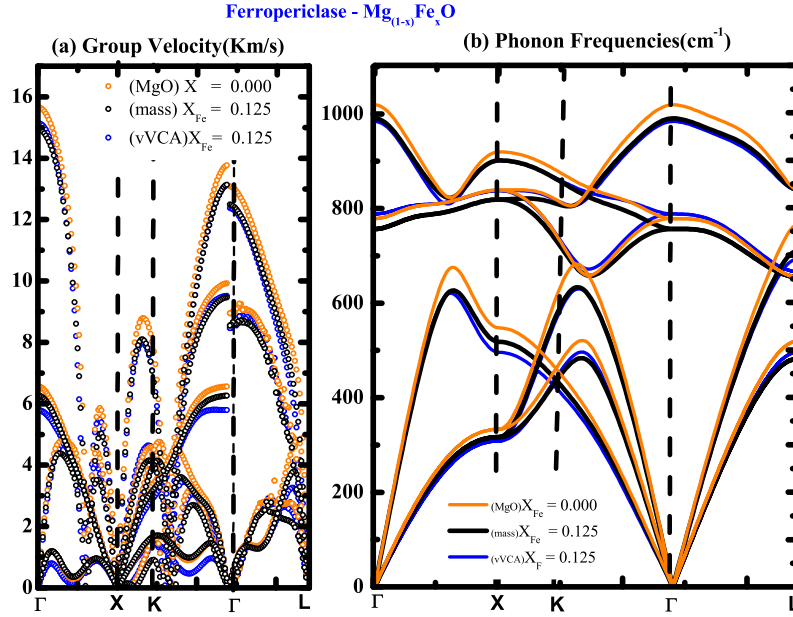


Figure 6.2: Phonon dispersion relations and mode group velocities in $\text{Mg}_{0.875}\text{Fe}_{0.125}\text{O}$. The black line/symbols shows the result obtained by replacing the mass of Mg in the MgO calculation by the weighted mass $\text{Mg}_{0.875}\text{Fe}_{0.125}$. The blue lines/symbols show the result obtained from the vVCA approach where the interatomic force constants are directly calculated as described in section 2.6. Fe substitution is seen to have the effect of softening phonon frequencies and mode group velocities.

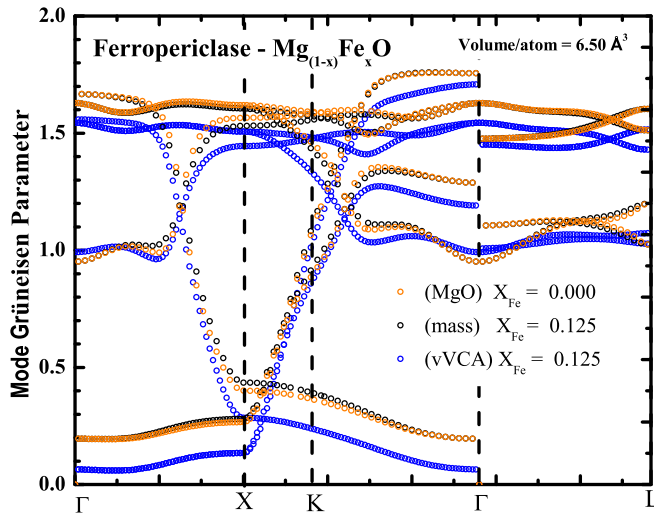


Figure 6.3: Mode Grüneisen parameter

6.4 Phonon Lifetimes

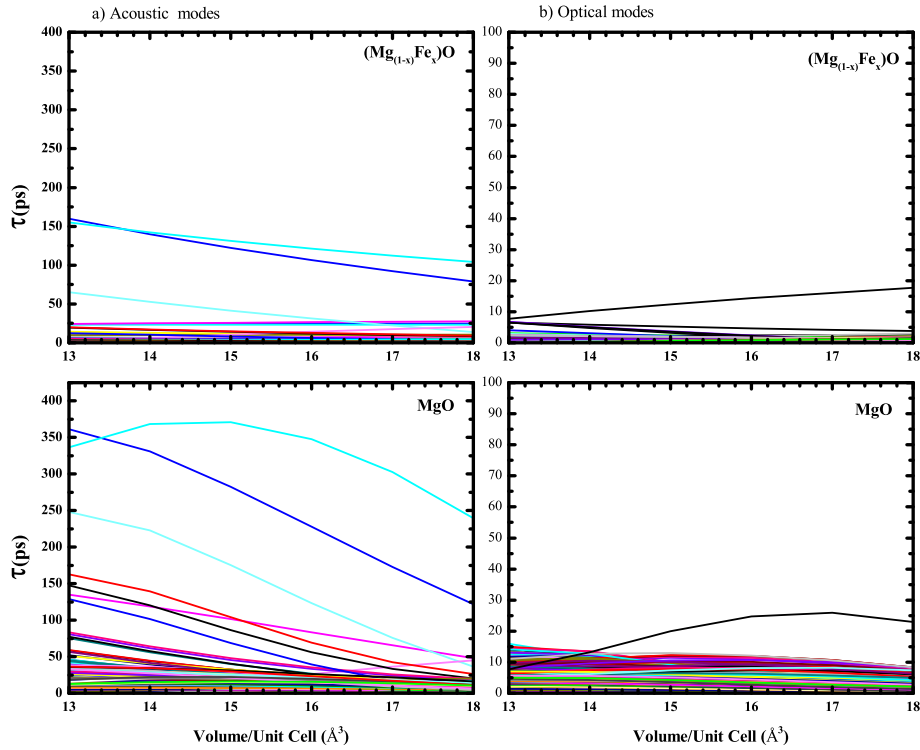


Figure 6.4: Volume/density dependence of phonon lifetimes of acoustic and optical phonon modes in fp as predicted by vVCA compared to corresponding modes in MgO. Panels under a) show the density dependence of the lifetimes for acoustic modes and b) shows the lifetimes of optical modes. The longest optical lifetime is nearly a factor of 10 lower than the longest acoustic mode, confirming the notion that acoustic modes are more effective heat transporters than the optical modes.

The phonon lifetimes are evaluated based on an $16 \times 16 \times 16$ k-point grid for a total of 4096 k-points, 145 of which are irreducible. The phonon-phonon scattering rates are directly evaluated from for all the irreducible k-points in the Brillouin zone and life times in the whole Brillouin Zone (BZ) are obtained using the symmetry relations between the irreducible k-points and the dependent ones. Figure 6.4 shows the density dependence of all the acoustic and optical phonon modes at the 145 irreducible k-points in the Brillouin zone

for MgO and fp respectively. Quantitatively, our study reveals that the lower frequency (acoustic) modes account for nearly 95% of the total conductivity in MgO and fp. It is observed that the phonon lifetimes of the acoustic modes in fp are almost a factor of two lower than those in MgO. In both cases, the modes having longer lifetimes show increasing lifetimes with increasing density (decreasing volume). The short lived modes are almost insensitive to pressure. Most of the modes have lifetimes that vary almost linearly with volume/density.

6.5 Lattice Thermal Conductivity of fp-Mg_(1-x)Fe_xO

Figure 6.5 shows that the lattice thermal conductivities associated with anharmonicity scattering are comparable in MgO and fp (see the orange and blue dashed lines). Including scattering due to mass disorder results in a reduction in thermal conductivity by a factor of 4-10

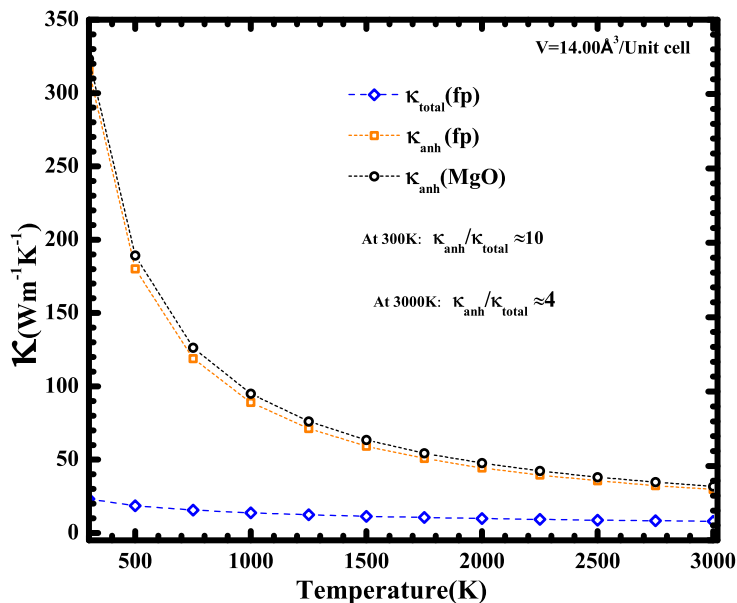


Figure 6.5: Thermal conductivity associated with anharmonicity

Figure 6.7 presents the thermal conductivity of fp for $x_{Fe} = 0.125$ in the LS. κ was directly calculated at 5 density points and from 300K to 3000K without any empirical extrapolation. $\kappa(T, P)$ is then derived using our first-principles calculated thermal EOS $V(T, P)$.

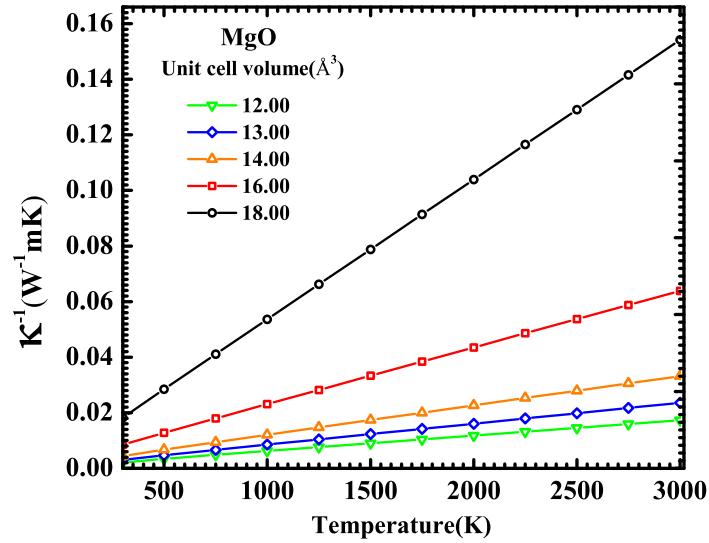


Figure 6.6: Temperature dependence of κ^{-1} in MgO. κ was calculated at 5 distinct densities corresponding to unit cell volumes shown on the figure, at 12 different temperatures ranging from 300 K to 3000K. Our calculated κ follows a T^{-1} dependence.

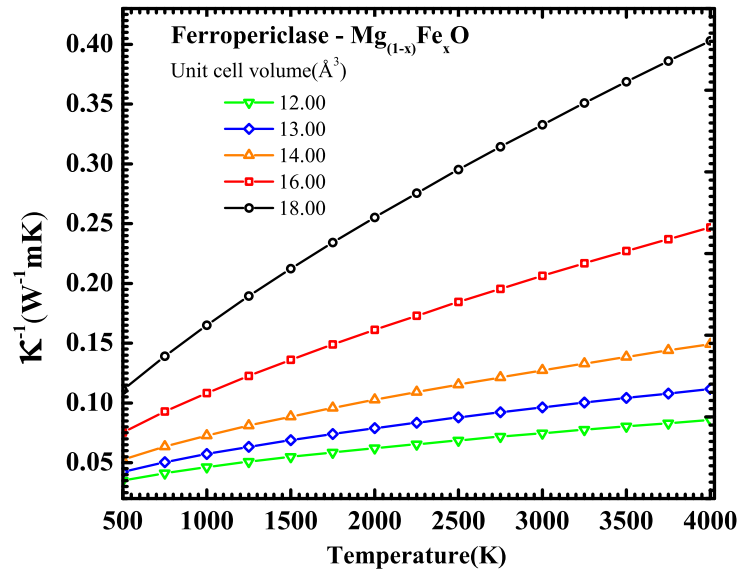


Figure 6.7: Temperature dependence of κ^{-1} in fp calculated at the corresponding unit cell volumes for the Fe-free MgO results presented in figure 6.6. κ does not quite follow the T^{-1} dependence seen in MgO.

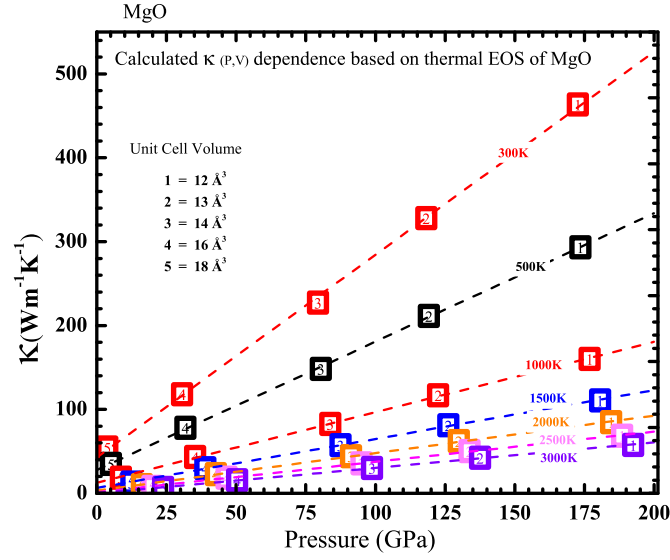


Figure 6.8: Pressure dependence of isothermal κ in MgO derived from our LDA calculated thermal EOS. For each isotherm, we used our calculated thermal EOS to determine the pressure corresponding to the unit cell volumes 12, 13, 14, 16 & 18 \AA^3 labeled 1, 2, 3, 4 & 5 along the isotherms: 300 K - 3000 K. Only seven of the 12 isotherms are shown, for clarity. By fitting this to a second order polynomial in P ($\kappa = a_0 + a_1P + a_2P^2$) we used the coefficients a_0, a_1, a_2 from the 12 isotherms to predict κ at isobaric conditions.

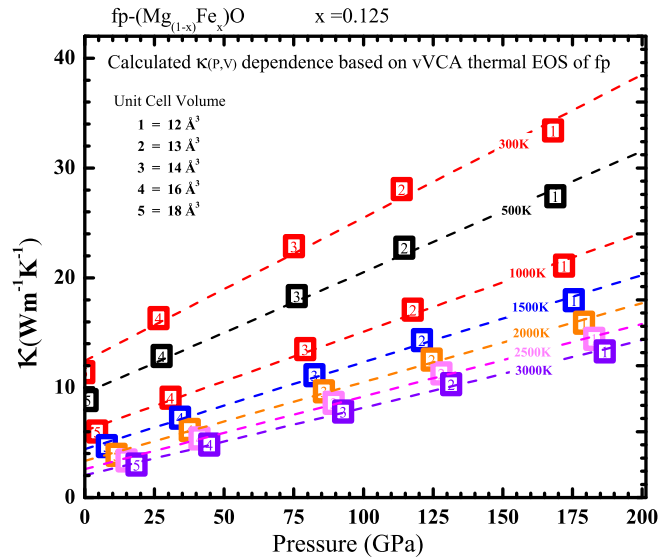


Figure 6.9: Pressure dependence of κ at isothermal conditions in fp. This pressure dependence was derived using the same approach described under figure 6.8

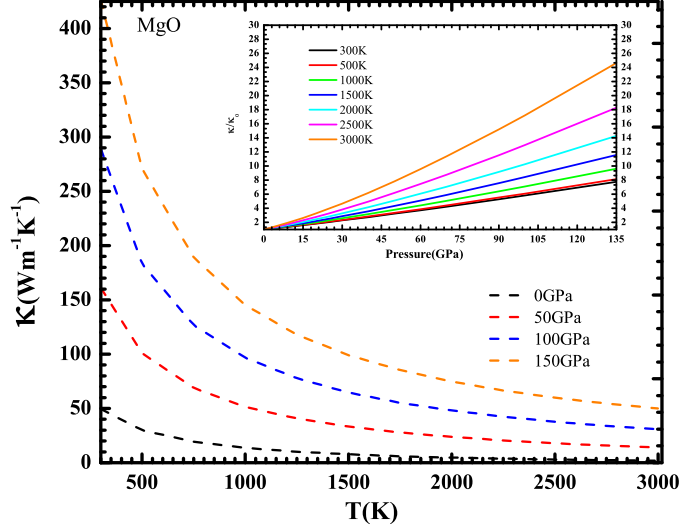


Figure 6.10: Main: Temperature dependence of isobaric κ in MgO. Using the coefficients from $\kappa = a_0 + a_1P + a_2P^2$ we derived the isobaric thermal conductivity. Four isobars 0, 50, 100 and 150 GPa are shown. Inset: Pressure variation of normalized κ . κ_0 represents the thermal conductivity at 0 GPa for each isotherm. From 300 K to 3000K, κ/κ_0 increases from 8 to 25 at 135 GPa.

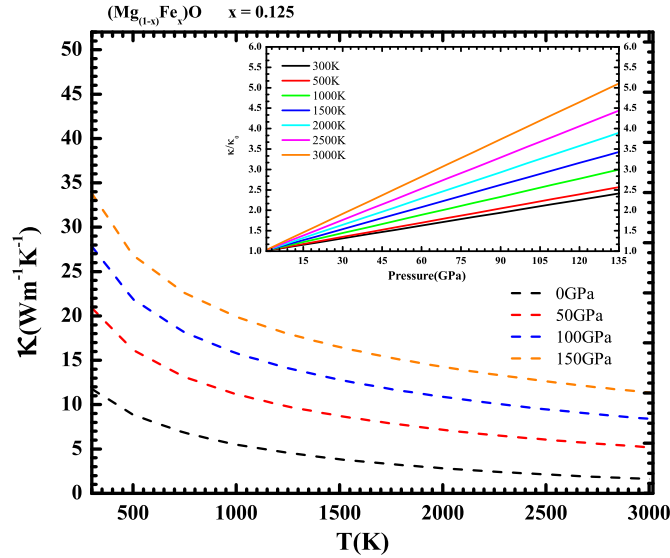


Figure 6.11: Main: Temperature dependence of isobaric κ in $\text{Mg}_{(1-x)}\text{Fe}_x\text{O}$; Inset: Pressure dependence of $\frac{\kappa}{\kappa_0}$ from 0 GPa to 135 GPa. κ_0 is the thermal conductivity at 0 GPa for each isotherm. From 300 K to 3000K, κ/κ_0 increases from 2.4 to 5 at 135 GPa. This is almost a factor of 5 lower than in MgO.

6.6 Conclusions

Substituting Mg with Fe lowers lattice thermal conductivity through two mechanisms: (1) adding additional disorder that scatters phonons and therefore further reduces phonon lifetimes, and (2) lowering phonon group velocities because of weaker chemical bonds and larger Fe mass. As a first step to quantitatively estimate the factor of reduction due to Fe substitution, we neglect the changes due to chemical difference of Mg and Fe, and focus only on the effects of mass difference, i.e. approximating the iron-bearing mineral solid solution systems with the same force constants and lattice anharmonicity, but with additional Mg/Fe mass disorder and heavier average mass ($\text{Mg}_{1-x}\text{Fe}_x$). Our approximation provides the upper limits of κ_{latt} in the solid solution systems, and it is valid for the Mg-rich system. We also carried out a test based on more computationally intensive vibrational virtual crystal approximation (vVCA) method for Fe-bearing $\text{Mg}_{1-x}\text{Fe}_x\text{O}$ model containing 12.5% low-spin ferrous Fe^{2+} . We confirmed that the mass effects are significantly larger than those due to the change of force constants at the high temperatures.

CHAPTER 7

IMPLICATIONS FOR HEAT FLOW ACROSS THE CORE-MANTLE BOUNDARY (CMB)

Parts of this Chapter 7 have been submitted for publication in Nature Geoscience by Tang, Ntam, Dong, Rainey, and Kavner.

7.1 Introduction

The core/mantle boundary (CMB) is the major thermal boundary layer in the Earth's deep interior, and the heat flux cross the CMB (J_{CMB}) governs the thermochemical trajectory of the Earth. Yet, estimates of J_{CMB} are widely scattered, ranging from 5 to 15 terawatts⁵. The lower-bound-estimates suggest that additional sources of heat in the mantle such as enhanced internal heating or an additional thermal boundary layer are required to accommodate the observed budget of 47 ± 3 terawatts from the surface of the Earth^{1,5}. The upper-bound-estimates suggest a recent evolution of the inner core/outer core system and high internal temperatures for early Earth conditions¹². To constrain these interlocked deep-Earth evolution models, we provide a comprehensive evaluation of lower mantle (LM) thermal conductivity κ_{LM} , anchored on our first-principles calculations of the pressure- and temperature-dependent lattice contribution to the heat transport in the most abundant lower mantle mineral (Mg,Fe)SiO₃ perovskite, which demonstrate a heretofore unrecognized shallow pressure dependence. Including a re-evaluation of conflicting data sets constraining the radiative contribution to overall κ , we show that values for κ_{LM} are much lower than previously thought, and approximately constant throughout the lower mantle, with little sensitivity to lateral variations in temperature.

The thermal conductivity κ , a material property relating the heat flux \mathbf{J} to the temperature gradient ∇T , via Fourier's law, $\mathbf{J} = \kappa \nabla T$, is notoriously difficult to measure, especially at the extreme conditions relevant to Earth and planetary interiors. Discrepancies exist among measured and calculated κ values for the important deep Earth materials magnesium silicate perovskite (PV-MgSiO₃ Osako et al¹³⁴, Manthilake et al¹⁰⁷ and periclase (MgO)^{48,58,101,106}, due to large uncertainties arising from differing models used to extrapolate those values to high pressures and high temperatures^{19,112,145,146}, and confusion regarding the relative importance of contributions to overall thermal conductivity from lattice phonons (κ_{latt}) versus photon (κ_{rad})^{147,148}. The goal of this multidisciplinary study is to address all of these issues resulting in a robust determination of lower mantle thermal conductivity (κ_{LM}) and its dependence on pressure (P), temperature (T), and composition. A major challenge to constrain κ_{LM} is the lack of reliable physical models for κ_{latt} of complex minerals at extreme P-T conditions. Based on the density functional theory (DFT) and the kinetic Peierls-Boltzmann transport theory, we implemented a first-principles method to directly predict κ_{latt} of pure crystals without any empirical P-T extrapolations details reported in chapter 5. This method has been recently used to calculate κ_{latt} for MgO¹⁰¹ giving good agreement with independent experiments⁴⁸ and theory⁵⁸. However, it is significantly more challenging to accurately compute all the phonon-phonon scattering rates in the 20-atom orthorhombic unit-cell of PV-MgSiO₃ crystals than in the 2-atom cubic unit-cell of MgO crystals. In this study, we further improved the numerical efficiency of our algorithm and used more than 2 million CPU hours at massive parallelized computer clusters to calculate κ_{latt} of PV-MgSiO₃ at 36 P-T conditions, ranging from that of ambient to that at the CMB. Our calculated value for iron-free PV-MgSiO₃ at ambient conditions (gray lines in Figure 7.2) is in good agreement with one set of measurements under corresponding conditions¹³⁴, but noticeably lower than a recent set¹⁰⁷. Two important outcomes of our calculations are the significant reduction of κ_{latt} of PV-MgSiO₃ in comparison with MgO, and the

much lower pressure-dependence of the thermal conductivity of PV-MgSiO₃ than that of MgO. These unexpected results arise from the detailed differences in the phonon behavior between the high-symmetry, 2-atom unit cell MgO and the lower symmetry, 20-atom unit cell PV-MgSiO₃, and are at the root of our estimate of low thermal conductivity and weak pressure dependence. Our theoretical method provides a series of testable hypotheses about how crystalline symmetry, structure, and pressure affect thermal conductivity of mineral insulators

7.2 Results

The calculated phonon spectra of the iron-bearing solid solutions are shown in Figure 7.1. The scattering rates due to Mg/Fe mass disorder are evaluated using the Fermi golden rule equation 3.16 based on Fe-bearing phonon spectra. In the dilute limit, the total phonon scattering rates in the Fe-bearing solid solution systems are approximated as sum of scattering rates due to both lattice anharmonicity and the Mg/Fe mass disorder. Considering the predominant effect of Mg/Fe mass disorder in the current calculation, we assume that lattice anharmonicity induced phonon scattering rates in the mineral solid solutions are the same as those in the iron-free crystal. Iron (Fe) content affects the κ_{latt} of lower mantle minerals. However, it is difficult to untangle its contribution from that of lattice anharmonicity in experimental measurements. In this study, we analyzed the Mg/Fe mass disorder induced phonon scattering of substituting 12.5% of the Mg for Fe in both the perovskite and oxide. Including iron further lowers κ_{latt} , although the reduction at high pressures and temperatures is not as significant as it is closer to ambient conditions (Fig1). While the expected T^{-1} dependence of κ_{latt} for iron-free PV-MgSiO₃ at constant density is observed, the calculation for PV-MgSiO₃ down a typical lower mantle geotherm shows κ_{latt} is slightly below $\sim 1 \text{ Wm}^{-1}\text{K}^{-1}$ and approximately constant as a function of depth (Fig2), in contrast to the much higher-valued κ_{latt} and steeper depth dependence for (Mg,Fe)O¹⁰¹.

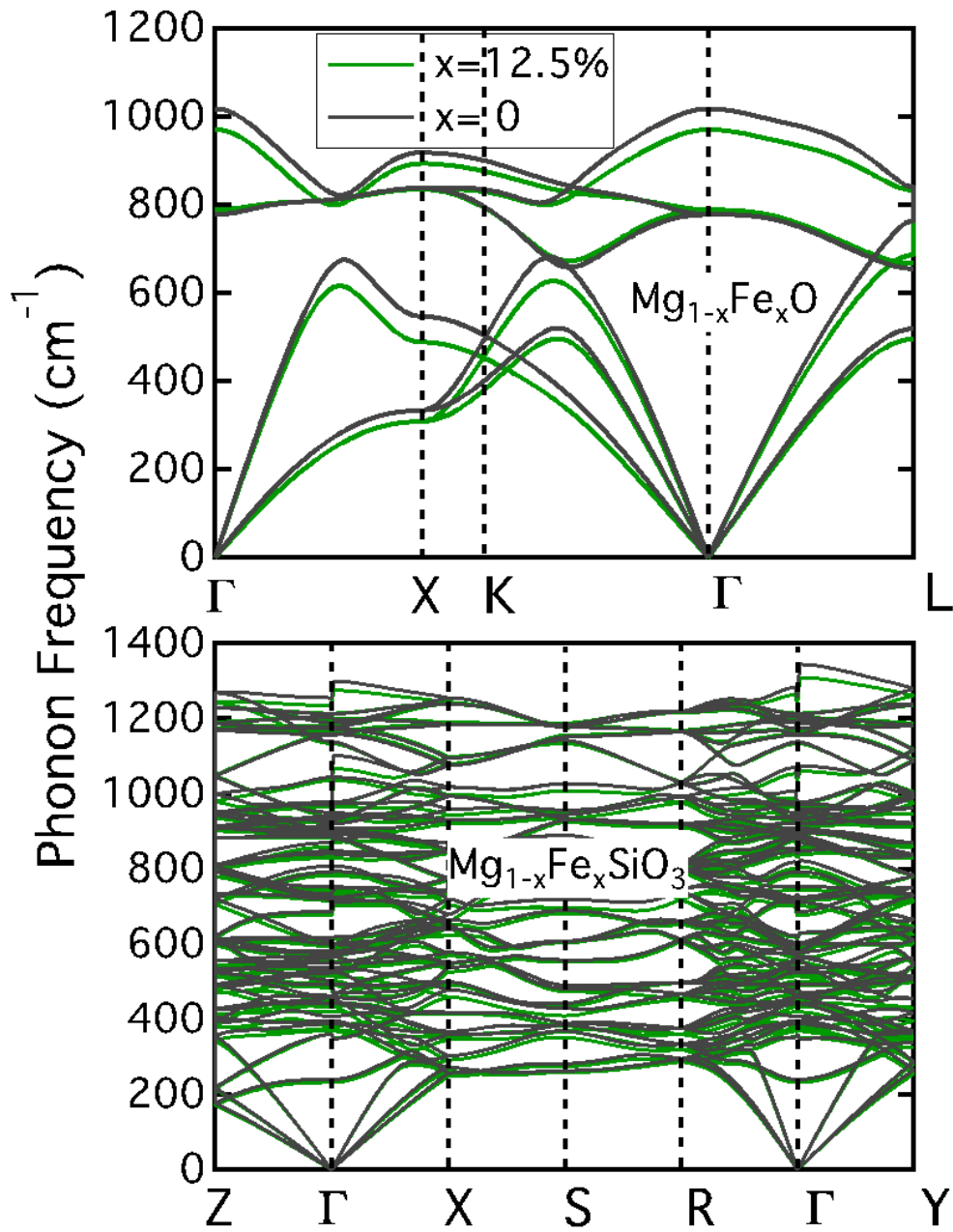


Figure 7.1: Vibrational phonon frequencies of $(\text{Mg}_{1-x}\text{Fe}_x)\text{O}$ (a) and $(\text{Mg}_{1-x}\text{Fe}_x)\text{SiO}_3$ -perovskite (b) with iron concentration $x=12.5\%$ at deep mantle pressure

Earth’s mantle is optically thick, and localized radiative heat transport may contribute to the overall diffusive heat transport. For this case, the photon radiative contribution to κ can be estimated using the Rosseland mean approximation^{149,150}. We provide two estimates based on a consistent analysis of the two sets of measured absorption spectra for Fe-bearing perovskite at high pressures^{147,148}. Choosing between these two estimates is beyond the scope of this work, but we were comforted to note that the two spectra showed a similar spectral structure and pressure dependence. The resulting estimates of radiative contribution to heat flow differ by a factor of 2 to 3; however we note that this is a significant improvement of the order-of-magnitude difference claimed in the original studies. This partial reconciliation of two disparate data sets arises from treating the optical absorption data consistently in the Rosseland calculation of κ_{rad} . Generally the calculated κ_{rad} is affected by scattering (e.g. grain boundary scattering) as well as absorption. Here we neglect a possible scattering component due to the short absorption length scales (~ 100 m) compared with the expected grain sizes of the lower mantle (~ 1 mm). The presence of additional scattering will only serve to lower the overall radiative thermal conductivity; thus we consider our estimates for κ_{rad} to be upper bounds. The two dashed red lines in Figures 7.3 and correspond to calculations incorporating the two estimates for κ_{rad} at constant pressure as a function of temperature (Fig.2), and down a lower mantle geotherm (Figure 7.4). Our two calculations for the κ_{rad} of perovskite are similar in magnitude to the computed κ_{latt} , but with a strong positive temperature dependence (Figure 7.3) such that at low temperatures the lattice values dominate and at high temperatures the radiative values dominate. Total thermal conductivity is the sum of the lattice phonon and radiative contributions. Our resulting two estimates of total κ are approximately constant with temperature (Figure 7.3) and depth in the lower mantle (Figure 7.4). This temperature- and pressure- stability of the perovskite thermal conductivity is a robust result of our analysis. Modest temperature perturbations about the geotherm will increase the radiative contribution to κ while attenuating the lattice

contribution. Changes in iron content or other impurities will likely have the same effect on both radiative and lattice contributions; for example an increase in iron content will decrease the value of both components. Finally, we determine the total κ_{LM} based on the Maxwell-Garnett model, which is an effective medium approximation for examining the total conductivity of a composite where a minor phase exists as random inclusions within a matrix phase^{151,152}. As a first-order representation of the lower mantle, we consider a composite material consisting of a matrix of iron-bearing perovskite with $\sim 20\%$ iron-bearing oxide existing as isolated inclusions. Because the length scales for both phonon scattering ($\sim \text{nm}$) and typical optical depth for photon scattering ($\sim 10\text{-}100 \text{ m}$) are both likely to be less than the average grain size of individual perovskite and oxide grains ($\sim 1 \text{ mm}$), we perform the calculation by first summing the lattice and radiative contributions to κ for each phase, and then combining the two phases in the Maxwell Garnett composite model. Figure 3 shows

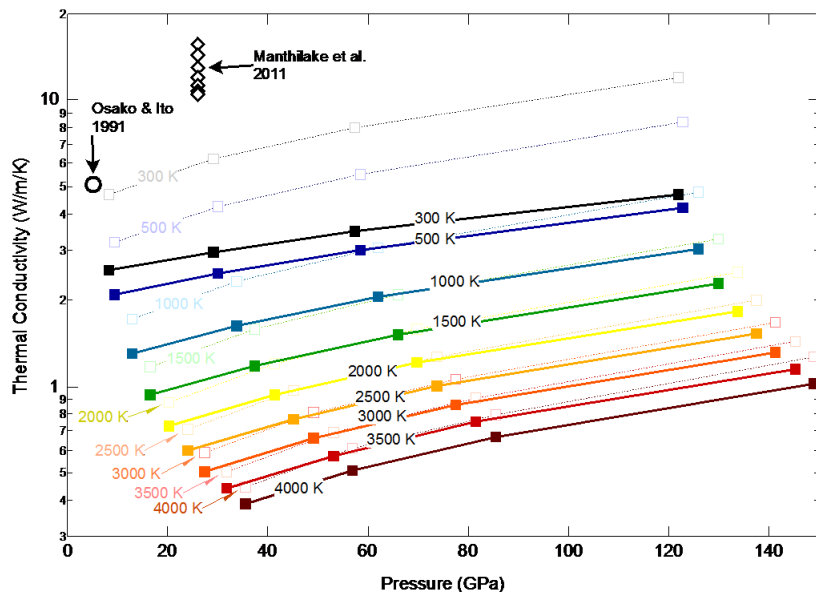


Figure 7.2: Calculated lattice thermal conductivity for MgSiO_3 perovskite as a function of pressure and temperature. Calculations are shown for Fe-free crystal (translucent symbols and lines) and mineral solid solution including 12.5% Fe (bold color symbols and lines). Also plotted are experimental data from Osaka & Ito, 1991 on MgSiO_3 and from Manthilake et al., 2011 on $(\text{Mg,Fe})\text{SiO}_3$ at temperatures from 473 to 1073 K.

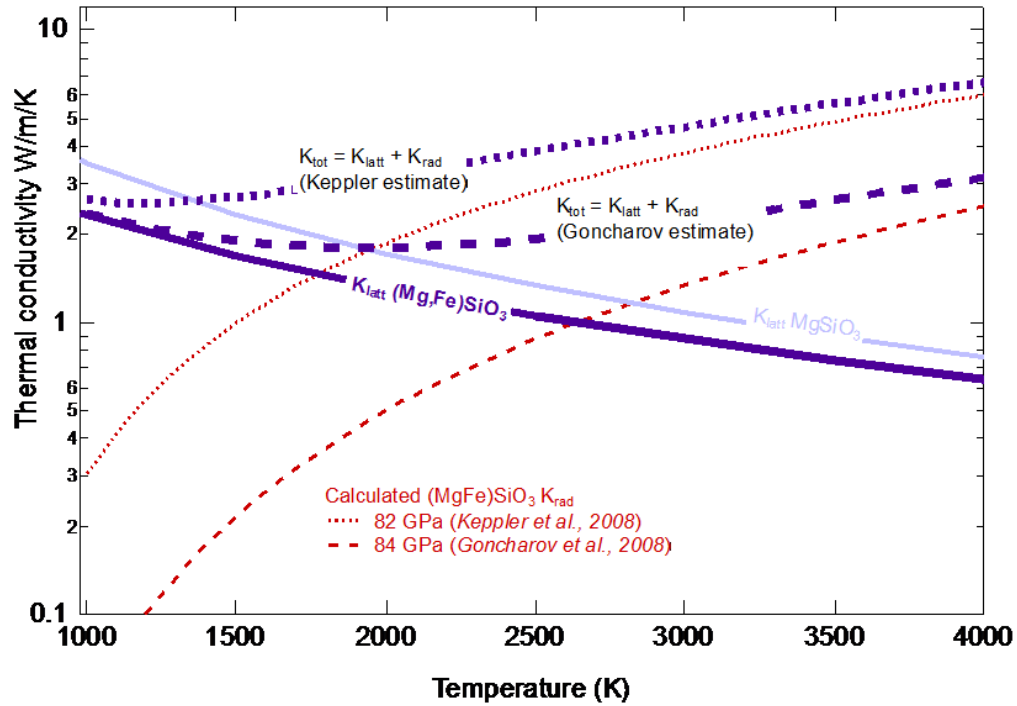


Figure 7.3: Isobaric thermal conductivity as a function of temperature. Computed lattice conductivity (solid purple line) and calculated contribution from radiative heat flow (red dashed and dotted lines, from optical absorption values provided by Goncharov et al., 2008 and Keppler et al., 2008 respectively, as a function of temperature at constant mid-mantle pressure of 80 GPa. The total thermal conductivity of perovskite is given by the sum of $\kappa_{rad} + \kappa_{latt}$ (purple dotted and dashed lines, corresponding to the two estimates for radiative contributions to the thermal conductivity)

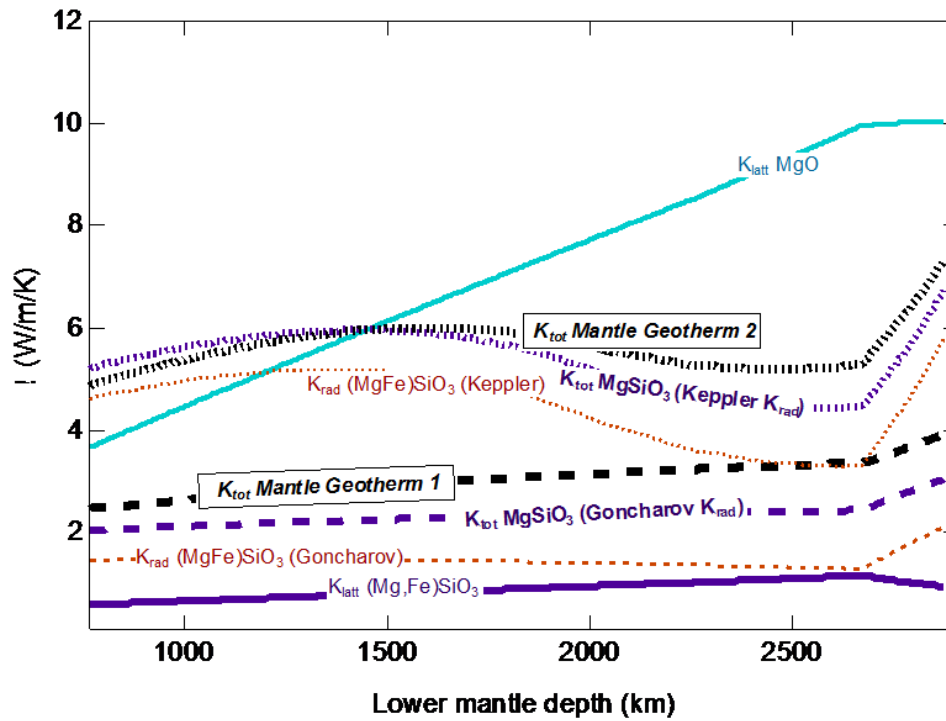


Figure 7.4: Thermal conductivity calculated down a sample lower mantle geotherm (Jeanloz) and thermal boundary layer. Lattice thermal conductivity calculated from first principles estimates for MgO (solid blue line, Tang & Dong, 2010), and MgSiO₃ perovskite (solid purple line, this study). Thin red lines show calculated radiative contribution to thermal conductivity from two optical absorption estimates (dashed line: Goncharov et al., 2008;

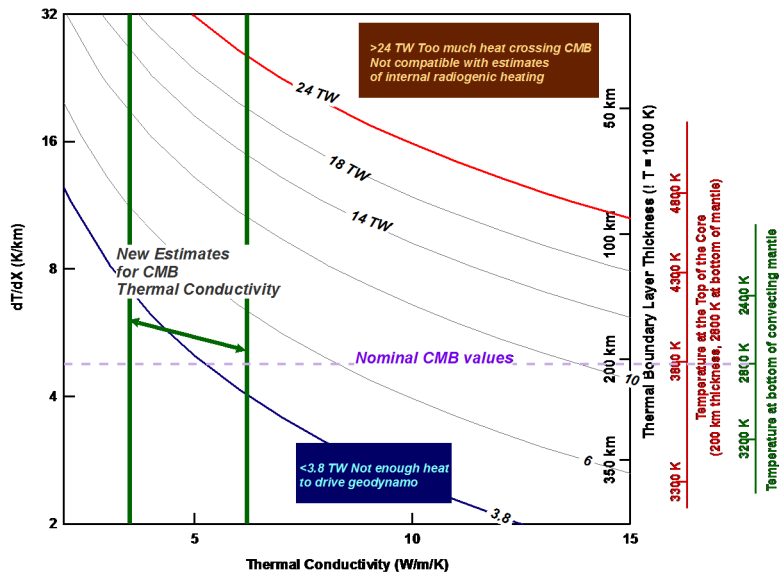


Figure 7.5: A plot summarizing the observational tradeoffs used to determine the total heat flow across the core-mantle boundary (contoured, labels in terawatts). Commonly assumed values from Lay et al., 2008 for the thermal boundary thickness, the temperature at the bottom of the mantle, and the temperature at the top of the core are shown on the right axis. Vertical solid green lines delineate our newly-determined range of estimates for lower mantle thermal conductivity.

two estimates for total κ_{LM} down a calculated mantle temperature profile¹⁵³, including the effect of a ~ 200 km-thick thermal boundary layer between the convecting lower mantle and the outer core. Our calculations suggest that thermal conductivity will increase across the steep temperature gradient of the thermal boundary layer, mostly due to increased radiative transfer. The thermal conductivity is lower if lower temperatures are assumed at the base of the convecting mantle, but the thermal boundary temperature dependence likely becomes steeper due to an increased gradient across the core/mantle boundary. When the uncertainties in the temperatures at the bottom of the convecting lower mantle and the top of the outer core⁵ are mapped onto an uncertainty in the thermal conductivity, we obtain values of values of 3.5 to 5.5 at the bottom of the convecting lower mantle. The thermal conductivity values rise across the thermal boundary layer if there is an increase in the radiative contribution to total heat flow in the lowermost boundary layer, which would occur in the absence of major phase and/or chemistry changes within the thermal boundary. These values represent a significant adjustment of the κ_{LM} downward from the typically used value of $10 \text{ Wm}^{-1}\text{K}^{-1}$. Models of thermal evolution of the mantle and the core are coupled via the κ_{LM} . Figure 4 illustrates how tradeoffs in the assumed values for thickness of the lower mantle thermal boundary, temperature at the top of the outer core, and temperature at the foot of the convecting mantle influence estimates of the total heat crossing the core mantle boundary. The contours in Figure 4 show the calculated total heat flow across the CMB given estimates of the thermal boundary layer conductivity (X-axis) and the temperature gradient across the boundary layer (left Y-axis). The temperature gradient across the boundary layer depends on estimates of the temperature in the outer core, the temperature of the bottom of the convecting mantle, and the thickness of the boundary layer; all of these parameters have some uncertainty. Often-used values (temperature of 2800 K at the bottom of the convecting mantle, 3800 K at the top of the core⁵, and a thermal boundary layer thickness that varies from 100 km to 200 km¹⁵⁴ are shown as a dashed

horizontal line. Using these values, the total heat flow across the core mantle boundary inferred from our new thermal conductivity estimates is calculated to be in the range of 3.5 to 5 TW, much lower than previous estimates of ~ 10 TW. Our new estimates of heat flux across the core/mantle boundary relax some of the constraints on timing of inner core growth¹², but pose difficulties (but not insurmountable ones) in accounting for the global heat balance of the mantle^{5,155}. Our new thermal conductivity values permit a heat flux larger than 5 TW across the core/mantle boundary, but require a steeper temperature gradient to do this. For example, a 10 TW heat flux across the core/mantle boundary can be most easily accomplished by assuming a much thinner thermal boundary layer, equal to 75 to 100 km. This is permissible within observational constraints, and is consistent with seismic observations of the boundary layer width above the core/mantle boundary¹⁵⁶). If the seismological constraints are taken as indicative of the thermal boundary layer thickness, then one must consider a laterally varying thickness of the thermal boundary layer. Our results suggest that variations of the thermal conductivity as a result of lateral variations in temperature or pressure will not be significant. However, local changes in modal abundance of minerals, chemistry such as iron content, presence of melt, and/or mechanical texturing may all serve to significantly perturb the value of the thermal conductivity. Therefore, our results suggest that any nonlinear influence that thermal conductivity has in geodynamical models¹¹ arises not from pressure- or temperature- dependence, but is solely a function of compositional heterogeneity at the base of the lowermost mantle.

7.3 Discussion

The thermal evolution of the whole Earth is poorly constrained, as laid out in a review by Lay et al⁵. As pointed out in that review, one of the keys to resolving that uncertainty is a better constraint of the material property of thermal conductivity relevant to the Earths lower mantle. For ~ 20 years, a value of ~ 10 W/m/K has been used, and this value was based on

a 1991 measurement at ambient conditions, with a long extrapolations in both pressure and temperature. The uncertainties in that extrapolated value are large (over a factor of two) and therefore our understanding of Earths thermal-mechanical-chemical evolution of both the mantle and the core systems are uncertain. The previously used pressure extrapolations of perovskite were based on models of the pressure-dependent behavior of phonons in simple high-symmetry iron-free crystals. These new show that previous pressure-dependent models are insufficient in complex materials systems, where contribution from optic phonons are non-negligible. Combining the evaluation of Mg/Fe mass disorder effects and our prediction of lattice thermal conductivity of $(\text{Mg,Fe})\text{SiO}_3$ results in a lower estimate for thermal conductivity throughout the Earths deep mantle. Besides the first-principles calculations themselves, we provide a synthesis of the bottom line contribution for two issues that contribute to understanding heat flow in the deep Earth: a radiative contribution and the composite effect, drawing on an extensive multidisciplinary literature that quantitatively describes these effects. Particularly, the radiative contribution to the overall heat transport has caused a great deal of uncertainty in the literature, with two papers published in Nature and Science in 2008 making opposite claims based on similar measurements. As part of this study, we return to the optical absorption data sets as originally published, and treat them both in a self-consistent and physically correct manner. The result is a partial reconciliation of the two estimates, with predictions for radiative conductivity in the lower mantle that differ by a factor of 2-3, rather than the order-of-magnitude disagreement originally cited in the literature.

7.4 Conclusions

The end result is a new estimate of the lower mantle thermal conductivity throughout the lower mantle. The number is still uncertain, mostly due to lingering uncertainties in the radiative component of thermal conductivity and the composite effect of combining

oxide which has much higher thermal conductivity with perovskite, which has much lower. Even with this uncertainty, two results of our study are extremely robust. First, our study requires that much lower values of thermal conductivity, $\sim 3.55.5$ W/m/K rather than previous estimate of 5-15 W/m/K be adopted in our Earths thermal evolution models. This new range of values has the advantage of relaxing some of the constraints on timing of the inner core growth, and allowing for a more reasonable initial temperature profile at the origin of whole Earth evolution. The second robust result is our finding that thermal conductivity is likely single-valued as a function of depth throughout the lower mantle and insensitive to local variations in temperature. This arises because the lattice component and radiative component of thermal conductivities have approximately similar magnitudes, but with opposite temperature and weak pressure dependencies. This means that geodynamical models can rest soundly on the assumption of a constant value of thermal conductivity throughout the convecting lower mantle. This simplifies calculations significantly, and lessens the likelihood of nonlinearities due to temperature-dependent thermal conductivity.

CHAPTER 8

CONCLUSIONS AND FUTURE WORK

In summary, I have presented here the results of our recent first-principles calculations of lattice thermal conductivities of Earth forming minerals using our recently developed computational techniques based on first-principles DFT. Under methodology development, we have optimized our recently developed real space supercell finite displacement algorithm to extract the harmonic and anharmonic inter-atomic potentials for complex material systems up to 20-atoms per unit cell and also implemented the vibrational virtual crystal approximation for the study of mineral solid-solutions.

Using the extracted third order lattice anharmonicity I have evaluated the phonon scattering rates of individual phonon modes based on quantum mechanical scattering theory at high temperature and pressure conditions relevant to the Earth's lower mantle, without any empirical fitting. Our calculation of phonon-phonon scattering rates was within the framework of the single mode excitation approximation (SMEA). To better understand the pressure dependence of thermal conductivity, I have studied the volume/density dependence of the group velocities and phonon lifetimes of individual phonon modes. My study reveals that phonon scattering rates for optical modes are almost insensitive to pressure. The pressure dependence of the lattice thermal conductivity appears to be largely determined by the pressure behavior of the scattering rates of acoustic phonon modes. Acoustic phonon modes are found to be the effective carriers of heat in MgO, (Mg,Fe)O (3 acoustic + 3 optic) and α -Al₂O₃ (3-acoustic +27 optic) , while the optical modes account for most of the heat transport in PV-MgSiO₃ (3 acoustic + 57 optic). Table 8.1 summarizes the contribution to the overall lattice thermal conductivity at ambient conditions:

Table 8.1: Contributions to overall κ_{latt} from acoustic and optical phonon modes in MgO, α -Al₂O₃ and PV-MgSiO₃

System	κ_{acc} (Wm ⁻¹ K ⁻¹)	κ_{opt} (Wm ⁻¹ K ⁻¹)	κ_{latt} (Wm ⁻¹ K ⁻¹)
MgO	46.30	8.45	54.75
α -Al ₂ O ₃	16.59	9.70	26.29
PV-MgSiO ₃	1.63	3.08	4.71

We have successfully predicted the lattice thermal conductivity of PV-MgSiO₃ at lower mantle conditions. While discrepancies remain between our predicted values at ambient conditions and measurements from experiment, we do observe unusual behavior in existing experimental data. We are currently repeating our calculation to systematically test for: different Brillouin zone K-point sampling grids, third order lattice anharmonicity cut-offs and the GGA formalism.

Using our recent implementation of the vibrational virtual crystal approximation we have studied the effect of Fe on the thermodynamic and thermal transport properties of ferropicricle (Mg,Fe)O based on and Fe content of 12.5%. Fe is observed to lower the thermal conductivity of ferropicricle. We have also estimated the effect of Fe on the thermal conductivity of (Mg,Fe)SiO₃ in the dilute limit, assuming same harmonic and anharmonic lattice dynamics as Fe-free PV-MgSiO₃, and discussed the implications for heat flow in the Earth’s lower mantle.

Lifetimes of phonon modes in MgO are observed to follow the $\tau \propto \omega^{-2}$ behavior consistent with Klemens’ formular^{157–159}(equation 8.1) while MgSiO₃ phonon lifetimes do not follow this rule.

$$\frac{1}{\tau_{\vec{q},i}} = \gamma_{\vec{q},i}^2 \frac{2K_B T}{M v_{\vec{q},i}^2} \frac{\omega_{\vec{q},i}^2}{\omega_i^{\max}} \quad (8.1)$$

Here τ is the phonon lifetime, γ , V_g and ω are the mode Grüneisen parameter, mode group velocity and phonon frequency of a phonon mode (\vec{q}, i) ; ω_i^{\max} is the largest frequency in the i^{th} branch. According to Klemens’ rule, low-frequency phonons will have longer lifetimes and thus contribute more to the thermal conductivity.

Future Work

The behavior of phonon mode lifetimes in PV-MgSiO₃ deserves further investigation. All DFT calculations reported here were performed within the LDA framework; It is necessary to repeat these calculations within the generalized gradient approximation (GGA), and test the convergence of calculated lattice thermal conductivity on the q-point sampling grid for the Brillouin Zone. The thermal conductivity calculations reported in this dissertation were performed within the Peierls-Boltzmann transport theory (*PBTT*) also known as the phonon gas model. Using a 2-D lattice model, Sun and Allen¹⁶⁰ claim that the phonon gas model breaks down at high temperatures. How this applies to real complex mineral systems is not yet well known. In future, it would be desirable to investigate the high temperature behavior of PV-MgSiO₃ using the Green-Kubo formalism. Immediate extensions of the the work presented in this dissertation would be a self consistent solution of the Boltzmann transport equation, and a careful investigation the effect of different Fe concentrations on the thermodynamic and thermal transport properties of (Mg,Fe)O and (Mg,Fe)SiO₃ by directly calculating the harmonic and anharmonic lattice dynamics, taking into account the effect of spin polarization in Fe.

BIBLIOGRAPHY

1. D. Anderson, *New theory of the Earth* (Cambridge Univ Pr, 2007).
2. K. Hirose and T. Lay, *Elements* **4**, 183 (June 2008).
3. T. Tsuchiya, J. Tsuchiya, K. Umemoto, and R. Wentzcovitch, *Earth and Planetary Science Letters* **224**, 241 (2004).
4. S. Labrosse and C. Jaupart, *Earth and Planetary Science Letters* **260**, 465 (2007).
5. T. Lay, J. Hernlund, and B. Buffett, *Nature Geoscience* **1**, 25 (2008).
6. D. Gubbins, A. Willis, and B. Sreenivasan, *Physics of the Earth and Planetary Interiors* **162**, 256 (2007).
7. J. Brown and R. McQueen, *Journal of Geophysical Research* **91**, 7485 (1986).
8. C. Matyska and D. Yuen, *Physics of the Earth and Planetary Interiors* **154**, 196 (2006).
9. J. B. Naliboff and L. H. Kellogg, *Physics of the Earth and Planetary Interiors* **161**, 86 (2007).
10. A. Van den Berg, E. Rainey, and D. Yuen, *Physics of the Earth and Planetary Interiors* **149**, 259 (2005).
11. A. M. Hofmeister and D. A. Yuen, *Journal of Geodynamics* **44**, 186 (2007).
12. B. Buffett, *Geophysical research letters* **29**, 7 (2002).
13. Y. Syono, *Pure and Applied Geophysics (PAGEOPH)* **143**, 759 (1994).

14. H. Hsu, K. Umemoto, Z. Wu, and R. Wentzcovitch, *Reviews in Mineralogy and Geochemistry* **71**, 169 (2010).
15. H. Spiering, E. Meissner, H. Köppen, E. Müller, and P. Gütlich, *Chemical Physics* **68**, 65 (1982).
16. J. Lin, G. Vankó, S. Jacobsen, V. Iota, V. Struzhkin, V. Prakapenka, A. Kuznetsov, and C. Yoo, *Science* **317**, 1740 (2007).
17. A. M. Hofmeister, *Physics of the Earth and Planetary Interiors* **170**, 201 (2008).
18. A. Hofmeister, *Physics and chemistry of minerals* **33**, 45 (2006).
19. A. Hofmeister, *Proceedings of the National Academy of Sciences* **104**, 9192 (2007).
20. M. Pertermann and A. Hofmeister, *American Mineralogist* **91**, 1747 (2006).
21. A. M. Hofmeister, *Physics of the Earth and Planetary Interiors* **180**, 138 (2010).
22. V. Solomatov and C. Reese, *J. Geophys. Res* **113**, B07408 (2008).
23. L. Lorenz, *Ann. Phys.* **13**, 422 (1881).
24. A. van den Berg, D. Yuen, G. Beebe, and M. Christiansen, *Physics of the Earth and Planetary Interiors* **178**, 136 (2010).
25. Y. Touloukian, R. Powell, C. Ho, and P. Klemens (1970).
26. M. Graf, S. Yip, J. Sauls, and D. Rainer, *Physical Review B* **53**, 15147 (1996).
27. F. Blatt, *Physics of electronic conduction in solids*, vol. 191 (McGraw-Hill New York, 1968).
28. K. Ohta, K. Hirose, M. Ichiki, K. Shimizu, N. Sata, and Y. Ohishi, *Earth and Planetary Science Letters* **289**, 497 (2010).

29. A. Oganov, J. Brodholt, and G. Price, *Earth and Planetary Science Letters* **184**, 555 (2001).
30. K. Watari and S. Shinde, *MRS Bulletin* **26**, 440 (2001).
31. S. Shindé and J. Goela, *High thermal conductivity materials* (Springer Verlag, 2006).
32. J. Klett, R. Hardy, E. Romine, C. Walls, and T. Burchell, *Carbon* **38**, 953 (2000).
33. W. Kim, J. Zide, A. Gossard, D. Klenov, S. Stemmer, A. Shakouri, and A. Majumdar, *Physical review letters* **96**, 45901 (2006).
34. D. Clarke, *Surface and Coatings Technology* **163**, 67 (2003).
35. K. Kurosaki, A. Kosuga, H. Muta, M. Uno, and S. Yamanaka, *Applied Physics Letters* **87**, 061919 (2005).
36. M. Dresselhaus, G. Chen, M. Tang, R. Yang, H. Lee, D. Wang, Z. Ren, J. Fleurial, and P. Gogna, *Advanced Materials* **19**, 1043 (2007).
37. G. Nolas, G. Slack, D. Morelli, T. Tritt, and A. Ehrlich, *Journal of Applied Physics* **79**, 4002 (1996).
38. D. Morelli and G. Meisner, *Journal of applied physics* **77**, 3777 (1995).
39. J. Wu, X. Wei, N. Padture, P. Klemens, M. Gell, E. García, P. Miranzo, and M. Osendi, *Journal of the American Ceramic Society* **85**, 3031 (2002).
40. X. Cao, R. Vassen, and D. Stoeber, *Journal of the European Ceramic Society* **24**, 1 (2004).
41. R. Vassen, X. Cao, F. Tietz, D. Basu, and D. Stöver, *Journal of the American Ceramic Society* **83**, 2023 (2000).
42. M. Winter and D. Clarke, *Journal of the American Ceramic Society* **90**, 533 (2007).

43. A. F. Goncharov, P. Beck, V. V. Struzhkin, B. D. Haugen, and S. D. Jacobsen, *Physics of the Earth and Planetary Interiors* **174**, 24 (2009).
44. P. Andersson and G. Backstrom, *Review of Scientific Instruments* **47**, 205 (1976).
45. R. Barker Jr, R. Chen, and R. Frost, *Journal of Polymer Science: Polymer Physics Edition* **15**, 1199 (1977).
46. R. Frost, R. Chen, and R. Barker, *Journal of Applied Physics* **46**, 4506 (1975).
47. H. Ftjjisawa, N. Ftjjii, H. Mizutani, H. Kanamoei, and S. Akimoto (1968).
48. T. Katsura, *Physics of the earth and planetary interiors* **101**, 73 (1997).
49. B. Hakansson, P. Andersson, and G. Backstrom, *Review of scientific instruments* **59**, 2269 (1988).
50. E. Abramson, J. Brown, and L. Slutsky, *The Journal of Chemical Physics* **115**, 10461 (2001).
51. E. Abramson, L. Slutsky, M. Harrell, and J. Brown, *The Journal of chemical physics* **110**, 10493 (1999).
52. M. Chai, J. Brown, and L. Slutsky, *Physics and chemistry of minerals* **23**, 470 (1996).
53. P. Beck, A. Goncharov, V. Struzhkin, B. Militzer, H. Mao, and R. Hemley, *Applied Physics Letters* **91**, 181914 (2007).
54. A. Goncharov, P. Beck, V. Struzhkin, B. Haugen, and S. Jacobsen, *Physics of the Earth and Planetary Interiors* **174**, 24 (2009).
55. A. Goncharov, V. Struzhkin, J. Montoya, S. Kharlamova, R. Kundargi, J. Siebert, J. Badro, D. Antonangeli, F. Ryerson, and W. Mao, *Physics of the Earth and Planetary Interiors* **180**, 148 (2010).

56. A. Hofmeister, Applied Physics Letters **95**, 096101 (2009).
57. D. Cahill and J. Li, Copyright 2011 Wen-Pin Hsieh (2011).
58. S. Stackhouse, L. Stixrude, and B. Karki, Physical review letters **104**, 208501 (2010).
59. P. Hohenberg and W. Kohn, Phys. Rev **136**, B864 (1964).
60. W. Kohn, L. Sham, et al., Phys. Rev **140**, A1133 (1965).
61. URL <http://cms.mpi.univie.ac.at/vasp/vasp/vasp.html>.
62. J. Hafner, Journal of computational chemistry **29**, 2044 (2008).
63. X. Gonze, J. Beuken, R. Caracas, F. Detraux, M. Fuchs, G. Rignanese, L. Sindic, M. Verstraete, G. Zerah, F. Jollet, et al., Computational Materials Science **25**, 478 (2002).
64. X. Gonze, Zeitschrift für Kristallographie **220**, 558 (2005).
65. P. Giannozzi, S. Baroni, N. Bonini, M. Calandra, R. Car, C. Cavazzoni, D. Ceresoli, G. Chiarotti, M. Cococcioni, I. Dabo, et al., Journal of Physics: Condensed Matter **21**, 395502 (2009).
66. R. Cohen, L. Boyer, M. Mehl, W. Pickett, and H. Krakauer, Perovskite: A Structure of Great Interest to Geophysics and Material Science (1989).
67. R. Cohen and J. Weitz (1996).
68. R. Cohen, NATO ASI SERIES C MATHEMATICAL AND PHYSICAL SCIENCES **543**, 201 (1999).
69. Z. Wu, X. Chen, V. Struzhkin, and R. Cohen, Physical Review B **71**, 214103 (2005).

70. R. M. Wentzcovitch, Y. G. Yu, and Z. Wu, *Reviews in Mineralogy and Geochemistry* **71**, 59 (2010).
71. K. Thomson, R. Wentzcovitch, and M. Bukowinski, *Science* **274**, 1880 (1996).
72. A. Oganov and S. Ono, *Nature* **430**, 445 (2004).
73. A. Oganov and S. Ono, *PNAS* **102**, 10828 (2005).
74. R. Caracas and R. Cohen, *AGU Fall Meeting Abstracts* **1**, 0191 (2004).
75. R. Caracas and R. Cohen, *Geophysical research letters* **32**, L06303 (2005).
76. H. Cynn, D. Isaak, E. Cohen Ronald, M. Nicol, and O. Anderson, *Am. Mineral.* **75**, 439 (1990).
77. L. Stixrude, R. Cohen, R. Yu, and H. Krakauer, *American Mineralogist* **81**, 1293 (1996).
78. J. Dong and O. Sankey, *J. Phys: Condens. Matter* **11**, 6129 (1999).
79. J. Dong, O. Sankey, S. Deb, G. Wolf, and P. McMillan, *Phys. Rev. B* **61**, 11979 (2000).
80. W. Duan, B. Karki, and R. Wentzcovitch, *Am. Mineral.* **84**, 1961 (1999).
81. R. Caracas and R. Cohen, *AGU Fall Meeting Abstracts* **1**, 07 (2005).
82. R. Caracas and R. Cohen, *Geophysical research letters* **32**, L16310 (2005).
83. G. Steinle-Neumann, L. Stixrude, and R. Cohen, *Physical Review B* **69**, 219903 (2004).
84. D. Machon, P. McMillan, B. Xu, and J. Dong, *Physical Review B* **73**, 094125 (2006).
85. J. Dong, O. Sankey, and G. Kern, *Phys. Rev. B* **60**, 950 (1999).
86. B. Karki and R. Wentzcovitch, *Physical Review B* **68**, 224304 (2003).
87. A. Oganov, M. Gillan, and G. Price, *Journal of Chemical Physics* **118**, 10174 (2003).

88. S. Ono, A. Oganov, T. Koyama, and H. Shimizu, *Earth Planet. Sci. Lett.* **246**, 326 (2006).
89. L. Stixrude and R. Cohen, *Nature* **364**, 613 (1993).
90. R. Caracas and R. Cohen, Arxiv preprint cond-mat/0603222 (2006).
91. R. Cohen, *Geophysical Research Letters* **14**, 1053 (1987).
92. J. Tsuchiya, T. Tsuchiya, and R. Wentzcovitch, *J. Geophys. Res* **110**, B02204 (2005).
93. Z. Wu, R. Wentzcovitch, K. Umemoto, B. Li, K. Hirose, and J. Zheng, *J. Geophys. Res* **113**, B06204 (2008).
94. I. Inbar and R. Cohen (1995).
95. D. Isaak, R. Cohen, and M. Mehl, *Journal of Geophysical Research* **95**, 7055 (1990).
96. F. Marton, J. Ita, and R. Cohen, Arxiv preprint physics/0010083 (2000).
97. X. Sha and R. Cohen, Arxiv preprint arXiv:0708.0183 (2007).
98. P. Dorogokupets, *Physics and Chemistry of Minerals* **37**, 677 (2010), ISSN 0342-1791, 10.1007/s00269-010-0367-2.
99. R. Wentzcovitch, L. Stixrude, and J. Rosso, *Theoretical and computational methods in mineral physics: geophysical applications* (Mineralogical Society of America, 2010).
100. J. Hafner, C. Wolverton, and G. Ceder, *MRS bulletin* **31**, 659 (2006).
101. X. Tang and J. Dong, *Proceedings of the National Academy of Sciences* **107**, 4539 (2010).
102. D. Evans and G. Morriss, *Statistical mechanics of nonequilibrium liquids* (Cambridge Univ Pr, 2008).

103. B. Daly, H. Maris, K. Imamura, and S. Tamura, PHYSICAL REVIEW-SERIES B- **66**, 24301 (2002).
104. F. Müller-Plathe, Journal of Chemical Physics **106**, 6082 (1997).
105. C. Nieto-Draghi and J. Avalos, Molecular Physics **101**, 2303 (2003).
106. N. De Koker, Physical review letters **103**, 125902 (2009).
107. G. Manthilake, N. de Koker, D. Frost, and C. McCammon, Proceedings of the National Academy of Sciences **108**, 17901 (2011).
108. R. Cohen, Arxiv preprint cond-mat/9708134 (1997).
109. S. Stackhouse and L. Stixrude, Reviews in Mineralogy and Geochemistry **71**, 253 (2010).
110. R. Kubo, Reports on Progress in Physics **29**, 255 (1966).
111. M. Green, The Journal of Chemical Physics **22**, 398 (1954).
112. X. Tang and J. Dong, Physics of the Earth and Planetary Interiors **174**, 33 (2009).
113. W. Frank, C. Elsässer, and M. Föhnle, Phys. Rev. Lett. **74**, 1791 (1995).
114. G. Kresse, J. Furthmüller, and J. Hafner, Europhys. Lett **32**, 729 (1995).
115. A. García and D. Vanderbilt, Phys. Rev. B **54**, 3817 (1996).
116. J. Dong, J. Tomfohr, O. Sankey, K. Leinenweber, M. Somayazulu, and P. McMillan, Phys. Rev. B **62**, 14685 (2000).
117. X. Tang and J. Dong, Bulletin of the American Physical Society (2006).
118. K. Kunc and R. Martin, Phys. Rev. Lett. **48**, 406 (1982).

119. B. Xu, Ph.D. thesis, Auburn University, AL (2009).
120. T. Barron and M. Klein, *Dynamical Properties of Solids* (North-Holland, Amsterdam, 1974).
121. J. Fabian and P. Allen, Physical review letters **79**, 1885 (1997).
122. N. Funamori and R. Jeanloz, Science **278**, 1109 (1997).
123. T. Mashimo, K. Tsumoto, K. Nakamura, Y. Noguchi, K. Fukuoka, and Y. Syono, Geophys. Res. Lett **27**, 2021 (2000).
124. J. Lin, O. Degtyareva, C. Prewitt, P. Dera, N. Sata, E. Gregoryanz, H. Mao, and R. Hemley, Nat. Mater. **3**, 389 (2004).
125. F. Marton and R. Cohen, The American mineralogist **79**, 789 (1994).
126. R. Caracas and R. Cohen, Geophys. Res. Lett **32**, L06303 (2005).
127. W. Kingery, Journal of the American Ceramic Society **37**, 88 (1954).
128. W. Kingery, J. Francl, R. Coble, and T. Vasilos, Journal of the American Ceramic Society **37**, 107 (1954).
129. G. Slack, Physical Review **126**, 427 (1962).
130. G. Kresse and J. Furthmüller, Comput. Mater. Sci **6**, 15 (1996).
131. G. Kresse and J. Furhmuller, Phys. Rev. B **47**, R558 (1993).
132. R. Caracas and R. E. Cohen, Geophys. Res. Lett **33**, 12 (2006).
133. D. Andrault, M. Muoz, N. Bolfan-Casanova, N. Guignot, J.-P. Perrillat, G. Aquilanti, and S. Pascarelli, Earth and Planetary Science Letters **293**, 90 (2010).
134. M. Osako and E. Ito, Geophysical Research Letters **18**, 239 (1991).

135. P. Blöchl, Phys. Rev. B **50**, 17953 (1994).
136. G. Kresse and D. Joubert, Phys. Rev. B **59**, 1758 (1999).
137. M. Murakami, K. Hirose, K. Kawamura, N. Sata, and Y. Ohishi, Science **304**, 855 (2004).
138. K. Catalli, S. Shim, and V. Prakapenka, Nature **462**, 782 (2009).
139. B. Grocholski, K. Catalli, S. Shim, and V. Prakapenka, Proceedings of the National Academy of Sciences **109**, 2275 (2012).
140. A.-L. Auzende, J. Badro, F. J. Ryerson, P. K. Weber, S. J. Fallon, A. Addad, J. Siebert, and G. Fiquet, Earth and Planetary Science Letters **269**, 164 (2008).
141. A. Dziewonski and D. Anderson, Physics of the earth and planetary interiors **25**, 297 (1981).
142. R. van der Hilst and H. Kárason, Science **283**, 1885 (1999).
143. S. Speziale, V. Lee, S. Clark, J. Lin, M. Pasternak, and R. Jeanloz, J. geophys. Res **112**, B10212 (2007).
144. K. Persson, A. Bengtson, G. Ceder, and D. Morgan, Geophysical research letters **33**, 16306 (2006).
145. A. Hofmeister, Science **283**, 1699 (1999).
146. N. de Koker, Earth and Planetary Science Letters **292**, 392 (2010).
147. A. Goncharov, B. Haugen, V. Struzhkin, P. Beck, and S. Jacobsen, Nature **456**, 231 (2008).
148. H. Keppler, L. Dubrovinsky, O. Narygina, and I. Kantor, Science **322**, 1529 (2008).

149. M. Alloy and D. Menezes, *Brazilian Journal of Physics* **37**, 1183 (2007).
150. R. Siegel and J. Howell, *Thermal radiation heat transfer*, vol. 1 (Taylor & Francis, 2002).
151. R. Progelhof, J. Throne, and R. Ruetsch, *Polymer Engineering & Science* **16**, 615 (1976).
152. O. Levy and D. Stroud, *Physical Review B* **56**, 8035 (1997).
153. R. Jeanloz and S. Morris, *Annual Review of Earth and Planetary Sciences* **14**, 377 (1986).
154. D. Turcotte and G. Schubert, *Geodynamics* (Cambridge Univ Pr, 2002).
155. K. Collaboration, A. Gando, Y. Gando, K. Ichimura, H. Ikeda, K. Inoue, Y. Kibe, Y. Kishimoto, M. Koga, Y. Minekawa, et al., *Nature Geoscience* **4**, 647 (2011).
156. J. Hernlund, C. Thomas, and P. Tackley, *Nature* **434**, 882 (2005).
157. R. Tye, *Thermal conductivity*, vol. 1 (Academic press, 1969).
158. P. Klemens, *Proceedings of the Royal Society of London. Series A. Mathematical and Physical Sciences* **208**, 108 (1951).
159. P. Klemens, *Thermochimica acta* **218**, 247 (1993).
160. T. Sun and P. Allen, *Physical Review B* **82**, 224305 (2010).
161. G. Kresse and J. Hafner, *Phys. Rev. B* **47**, 558 (1993).
162. X. Tang, *Theoretical study of thermal properties and thermal conductivities of crystals* (ProQuest, 2008).
163. K. Umemoto and R. Wentzcovitch, *PNAS* **105**, 6526 (2008).

164. D. Schiferl, W. Denner, H. Schulz, and W. Holzapfel, *J. Appl. Phys.* **49**, 4411 (1978).
165. J. Wachtman, W. Tefft, D. Lam, and R. Stinchfield, *J. Am. Ceram. Soc.* **43**, 334 (1960).
166. A. Schauer, *Can. J. Phys.* **43**, 523 (1965).
167. G. White and R. Roberts, *High Temperatures. High Pressures(Print)* **15**, 321 (1983).
168. P. Aldebert and J. Traverse, *High Temp-High Press* **16**, 127 (1984).
169. A. Amatuni, T. Malyutina, V. Chekhovskoi, and V. Petukhov, *High Temp-High Press* **8**, 565 (1976).

APPENDICES

APPENDIX A

FINITE DIFFERENCE METHOD FOR HARMONIC FORCE CONSTANTS

A.1 Symmetry Analysis

In crystal solid models, many of the atomic displacements are identical. As a result, computational time can be greatly reduced by carrying out first principle calculations only for the truly independent atomic displacements (irreducible moves). After making a choice of the sizes of the unit and super cell models, a group symmetry analysis is then performed to determine the atomic displacements that are truly independent. This information is stored in a file called *IrreducibleMoveList*. The symmetry analysis also determines the dependency relations between the dependent partial forces and the independent ones and also reveals which terms are zero. The symmetry analysis information is stored in the following files: *Phielement_depNZ.dat*, *Phielement_indNZ.dat* and *Phielement_zeroes.dat*, which contain the dependency information, indices of independent elements, and the zero terms in the force constants matrix, respectively (NZ stands for "non-zero"). The MgO calculation reported in this thesis, was based on 2-atom face centered cubic (f.c.c.) unit cell and 128-atom cubic super cell models. After the group symmetry analysis, we find that out of the 128 atoms in the super cell only 2 are truly independent, the rest are mirror images of these two under group symmetry operations. According to our finite displacement algorithm, we need to displace each of the independent atoms by a small but finite amount (Δ) in two directions ($+\Delta, -\Delta$). This results in a total of four-independent moves i.e. we need to perform four total energy calculations to obtain one full dynamic matrix as opposed to 256 calculations if we had to displace all the 128 atoms in the supercell. Consequently, our computational

time is reduced by a factor of 64 due to crystal symmetry alone. The symmetry analysis also reveals that force constants matrix of MgO has 52 non-zero independent elements, 48524 non-zero elements that are linearly dependent on the independent elements and a total of 25344 elements which are zeroes. We do not need to spend any computational time on the zero terms. Before performing a symmetry analysis to determine which atoms we need to displace, it is necessary to relax the ionic positions in the supercell to their ground state values. In the MgO calculation the relaxation was performed using VASP code with the following parameters:

- NSW = 999
- ISIF = 2
- IBRION = 2
- EDIFF = 1E-9
- LREAL=.TRUE.
- ISMEAR = 0

For a 128-atom cubic MgO supercell, it takes about one hour to complete the relaxation step. After relaxation, the One advantage of this step is that the 4 computations can be done concurrently if there are enough compute nodes, in which case it takes about one hour to complete the relaxation of the displaced calculate the partial forces on all the atoms due to the 4 displacements.

A.2 Calculation of Harmonic Force Constants

The next step is to calculate the partial forces resulting from the displacement of the unique atoms in the super cell according to the information in the *IrreducibleMoveList*

file. We use a code called *displacePair.x* to displace the desired atoms in the super cell. For total energy calculations, we use the VASP code^{130,161}. The VASP code requires the following inputs for a total energy calculation: POTCAR (wave functions, basis set) INCAR (Energy minimization parameters), POSCAR (displaced super cell) and KPOINTS (for Brillouin Zone sampling). One distinct advantage of this step is that it is highly parallelised, making it possible to perform all four total energy calculations concurrently if there are enough free compute nodes. For more complex systems with a large number of unique atomic displacements, sometimes we do not have enough compute nodes to run all computations concurrently. In such situations we submit several computations (jobs) per node and let them run one after the other. we use the portable batch system (PBS) queue software to manage job submission deletion from the computing cluster. The H-F forces are determined from the calculated total energies according to the Hellmann-Feynman theorem (equation 2.40) and used to evaluate the harmonic force constants. The algorithm for calculating the partial forces and force constants matrix elements when a single atom is displaced by a small, yet finite displacement (Δ) is described here¹⁶²

APPENDIX B

INTERPOLATION OF IRREDUCIBLE INTER-ATOMIC POTENTIALS (IIIP)

B.1 Introduction

We propose a new algorithm to interpolate the calculated irreducible inter-atomic force constants over the volumes of the simulation unit cells. This technique has several potential advantages. First, the interpolation of the irreducible harmonic force constants over the densities/volumes can serve as a useful guide in choosing the optimal value of atomic displacement (Δ) in our real space super cell finite displacement algorithm. A too small value will lead to higher numerical error while very large Δ would lead to more anharmonicity. Secondly the interpolation could potentially reveal the level of numerical uncertainties associated with our first-principles calculation thereby helping us control the quality of our data. We describe the IIIP technique next: The first step is to perform a first-principles total energy calculation to obtain the forces on different atoms based on different values of atomic displacement (Δ). Next, the set of inter-atomic force constants for each Δ are interpolated over the volumes of the simulation unit cells used in the total energy calculations. By comparing the smoothness of the inter-atomic force constant curves, it is easy to establish which choice of Δ is optimal or converged. Additionally, numerical uncertainties can be eliminated by fitting the calculated inter-atomic potentials up to 3rd order Birch-Murnaghan EOS. One distinct benefit of this BM EOS fitting approach is the predictive capability it has over the entire range of validity of the original calculation. This process is described in section B.3. Once we establish the trend of volume/density dependence of the calculated harmonic force constants, we can use this dependence to derive

harmonic force constants for any arbitrary density/volume within the range of validity of the original first principles calculation without the need to perform new total energy calculations. The interpolation process is described fully in the next section below with MgO as a case study.

B.2 Interpolation of Independent Force Constants

After extracting the independent elements of the force constants matrix at several unit cell volumes, we perform an interpolation of the elements over the volumes. In our MgO study, we extracted the independent force constants matrix elements at 20 different unit cell volumes between 10 \AA^3 and 20 \AA^3 using 4 different atomic displacements: (0.02, 0.04, 0.06, 0.08) \AA . Figure B.1 below shows an interpolation of the $\text{O}^{-2}\text{-O}^{-2}$ interatomic force constant from calculations based on four different finite displacements (Δ). The results show that an atomic displacement of 0.02 \AA or less would be too small as reflected by the irregular behavior of the force constant with volume, a clear deviation from the trend. It can be seen from this figure that we have a converged result for atomic displacements 0.04 , 0.06 & 0.08 \AA . For our real space super cell displacement calculations for MgO, we adopt an atomic displacement value of 0.04 \AA .

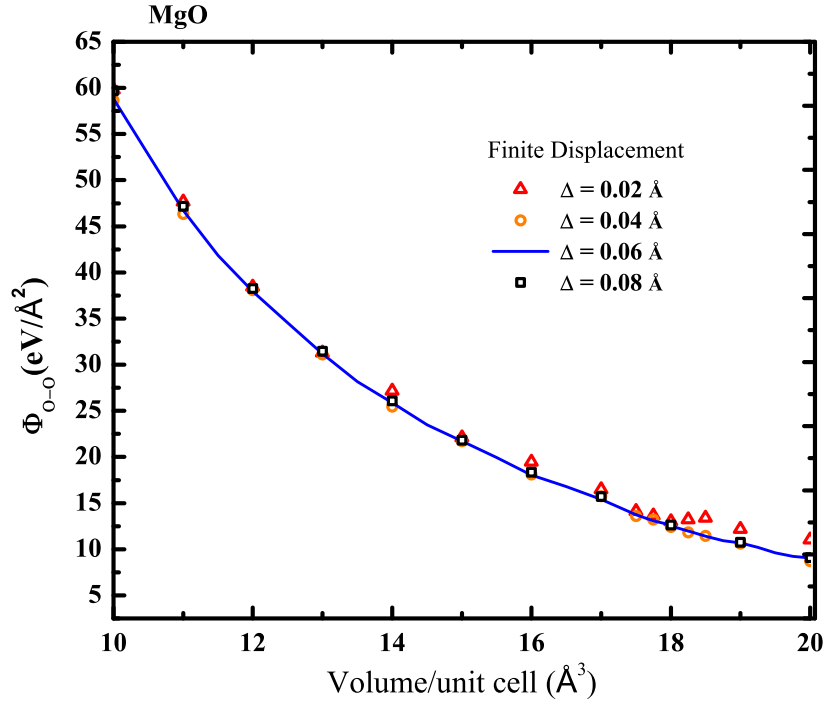


Figure B.1: Volume dependence of one inter-atomic Force constant calculated using different finite atomic displacements ($\Delta = 0.02, 0.04, 0.06, 0.08$)Å

B.3 Volume Dependence of Harmonic Force Constants Φ_{ij}

From our study of MgO, SrO and CaO, α -Al₂O₃ we have established that the interatomic force constants show a robust volume dependence according to Birch-Murnaghan equation of state up to third order as shown in equation B.1

$$\Phi(V)_{ij} = a + bx + cx^2 + dx^3 \quad (\text{B.1})$$

Where $x = V^{-\frac{2}{3}}$, V is the unit cell volume; a , b , c and d are parameters to be determined by fitting the calculated harmonic force constants to the unit cell volumes. For second order BM EOS fitting, $d=0$. These coefficients can be used to predict Φ_{ij} for any arbitrary volume within the range of the calculation from which the parameters were determined.

From this robust volume dependence of Φ_{ij} we observe that besides determining which atomic displacement (Δ) is appropriate for our RSSFD method, the interpolation of Φ_{ij} over the unit cell volumes has three distinct advantages. The first distinct advantage is that by establishing a robust volume dependence of the harmonic force constants, one can predict the independent force constants for other intermediate unit cell volumes without need for a new VASP calculation. This is particularly advantageous for systems with lower crystal symmetry, requiring longer computational times, to completely determine the H-F forces needed to extract the harmonic force constants for the full dynamic matrix. In such cases one can perform total energy calculations for a few unit cell volume sizes and then use the established volume dependence of the force constants (equation B.1) to generate the independent force constants for any arbitrary intermediate unit cell volumes within the range of validity of original the first principle calculation. This hypothesis was tested in our MgO study, by performing total energy calculations to directly determine the force constants for unit cell volumes 10 Å- 20 Å at steps of 2 Å. From the volume dependence, we predicted the force constants for the other unit cell volumes 11, 13, 15, 17 and 19 Å. We then performed total energy calculations to determine the force constants of MgO at these same unit cell volumes from first principles. The two results are almost indistinguishable. In figure B.2 we show the results of directly calculated independent force constants compared with those predicted from the volume dependence. Table B.1 shows the fitting parameters for the 52 independent harmonic force constants for our MgO calculation obtained by fitting our directly calculated force constants at five unit cell volumes (12 Å to 20 Å) to equation B.1. The calculation was done using a finite displacement of $\Delta = 0.04\text{Å}$. The first and second columns represent the indices of the atom pairs (including direction of displacement: x, y or z) corresponding to the independent interatomic force constants having fitting parameters a_0, a_1, a_2, a_3 (columns 3-6). One can use these fitting parameters in equation B.1 to generate $\Phi_{ii,jj}$ for any arbitrary volume between 12 Å and 20 Å. According to our notation, the 128

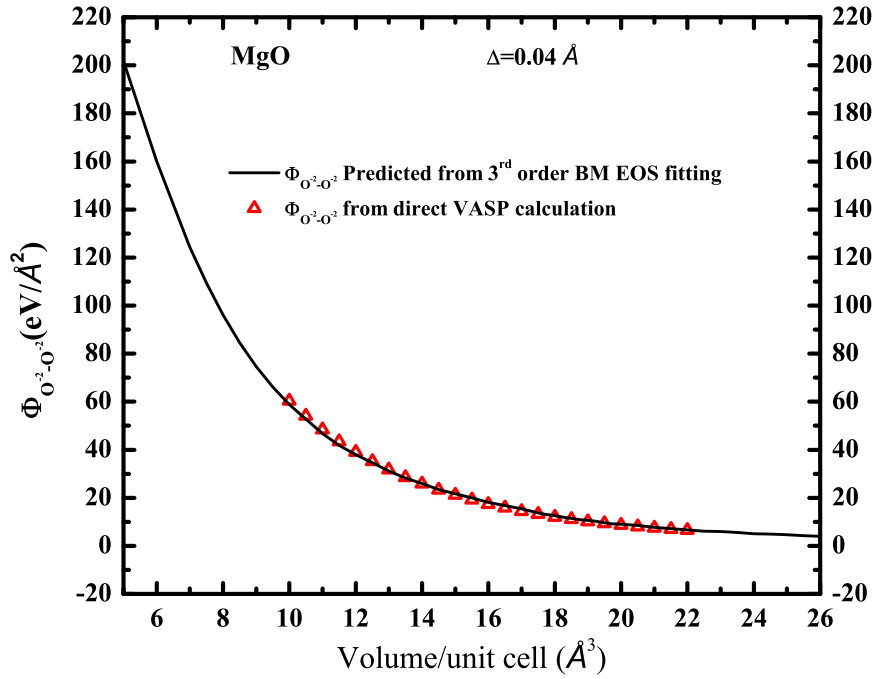


Figure B.2: Discrete symbols represent directly calculated values of irreducible interatomic force constants, solid lines are the values of force constants predicted using the fitting parameters from the calculated values according to equation B.1. Predicted force constants coincide with those from direct calculation.

atoms in our supercell are indexed from 1-128 with 1-64 being O^{-2} and 65-128 being Mg^{2+} . Atoms can be displaced in the directions $(\pm x, \pm y, \pm z)$. we label these directions $idir$ and $jdir$ taking values 1, 2, 3. ii and jj in table B.1 are related to the atom index ia , ja (1-128) as shown in equation B.2.

$$ii = (ia - 1) * Ns + idir \quad (B.2)$$

$$jj = (ja - 1) * Ns + jdir \quad (B.3)$$

Ns is the number of degrees of freedom ($Ns=3$ in our MgO calculation) The second advantage of this volume/density interpolation of harmonic force constants is that from the volume dependence of the force constants one can directly evaluate the Mode Grüneisen parameter (γ_i) via the analytic logarithmic volume derivative of the force constant elements without requiring two different force constant matrices to evaluate (γ_i) via finite difference.

$$\gamma_{\vec{q},i} \equiv -\frac{d \ln \omega(\vec{q}, i)}{d \ln V} = -\frac{1}{2\omega^2(\vec{q}, i)} \langle \mathbf{e}_i(\vec{q}) | \frac{d\mathbf{D}(\vec{q})}{d \ln V} | \mathbf{e}_i(\vec{q}) \rangle \quad (B.4)$$

$$\frac{d(D(\vec{q}))}{d \ln V} = \sum_l \left(\frac{d(\Phi_{ij})}{d \ln V} \right) \cdot \frac{\exp[-i\vec{q} \cdot (\vec{R}_{jl} - \vec{R}_{i0})]}{\sqrt{m_i m_j}} \quad (B.5)$$

The term $\frac{d(\Phi_{ij}(V))}{d \ln V}$ can be obtained by performing a logarithmic volume derivative of equation B.1 as follows: $\frac{d(\Phi_{ij}(V))}{d \ln V} = V \frac{d(\Phi_{ij}(V))}{dV} = -\frac{2}{3} (bx + 2cx^2 + 3dx^3)$, where $x = V^{-\frac{2}{3}}$.

In our previous approach namely the finite difference approach (FDA) for γ , two force constant matrices corresponding to two different unit cell volumes, were necessary to evaluate (γ_i) for any given unit cell volume as illustrated in equation B.6.

$$\gamma_i(V) = -\frac{V}{\omega_i^2} \sum_{\alpha\beta} \left(\frac{D_2 - D_1}{V_2 - V_1} \right)_{\alpha\beta} \hat{e}_i^*(\alpha) \hat{e}_i(\beta) \quad (B.6)$$

Here $V_1 < V < V_2$. Additionally, (γ_i) obtained this way involves taking the ratios of two differences. When the difference in the unit cell volumes is very small compared to the difference in the force constant matrices, this leads to divergence of (γ_i) which is difficult to distinguish from numerical error. This problem does not exist in our new approach, as we compute γ by directly evaluating the logarithmic derivative of the analytic form of the inter-atomic force constants. Details of the derivation of (γ_i) from the third order lattice anharmonicity are reported in section 2.5.

The third distinct advantage of our interpolation method is that one can use the volume dependence in equation B.1 to weed out numerical errors from calculated harmonic force constants. The volume/density dependence of all the irreducible force constants of three B1-structured ionic oxides: MgO, CaO and SrO is shown in the figures B.3, B.4 and B.5.

In table B.1, we present the fitting parameters a_0, a_1 and a_2 for all the 52 IFCs obtained by fitting our calculated MgO IFCs to third order BM EOS. One can use these parameters to predict IFCs for any arbitrary unit cell volume as follows: $\Phi(V)_{ij} = a + bx + cx^2 + dx^3$ with $x = V^{-\frac{2}{3}}$, V being the unit cell volume in \AA^3 .

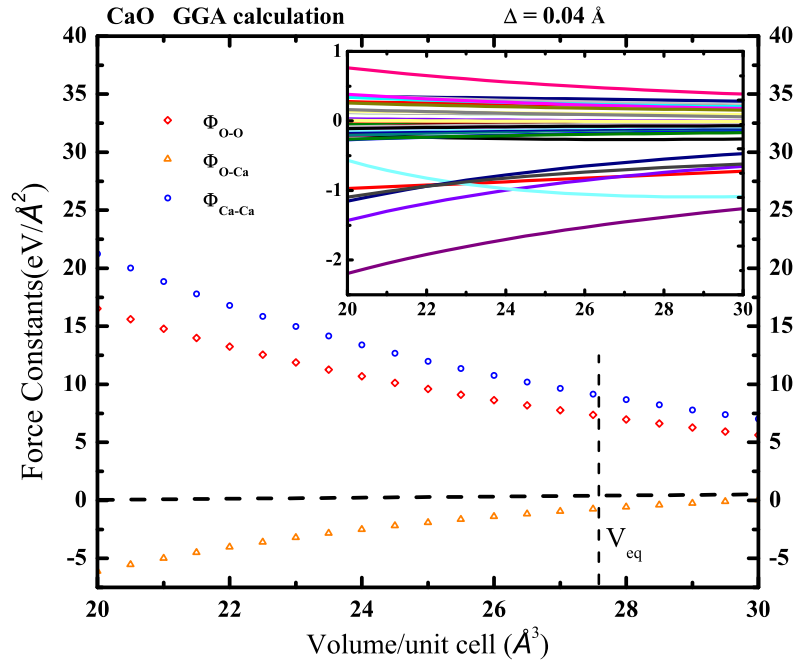


Figure B.3: Main: The dominant irreducible harmonic force constants corresponding to inter-atomic forces $\Phi_{Ca^{+2}-Ca^{+2}}$, $\Phi_{O^{-2}-Ca^{+2}}$, $\Phi_{O^{-2}-O^{-2}}$. Inset: Minor inter-atomic force constants (IFC). The major inter-atomic force constants are clearly volume dependent implying that the associated phonon frequencies are volume dependent. The mode Grüneisen parameter gives the volume dependence according to QHA theory. Most minor IFCs are volume independent.

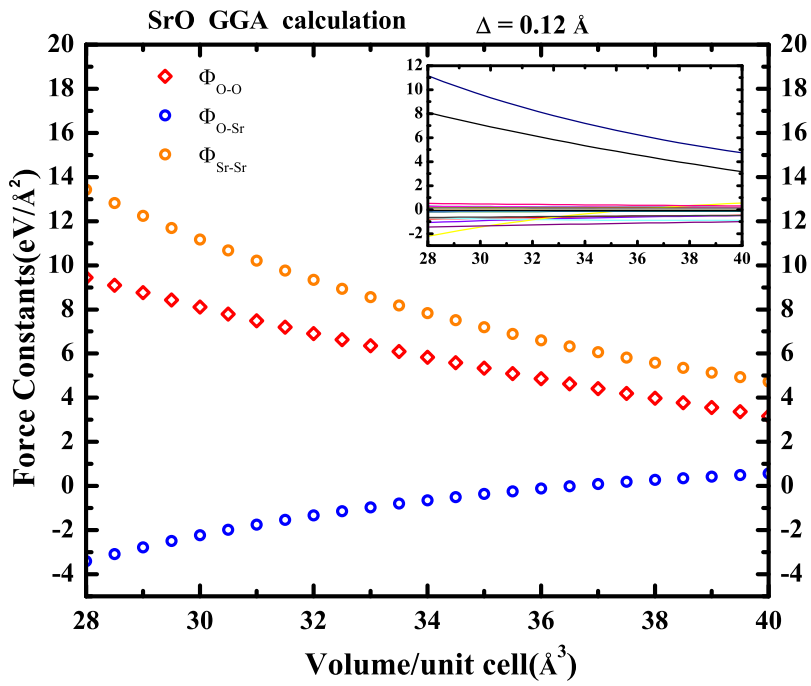


Figure B.4: Volume dependence of Force constants in SrO. Discrete symbols in the main graph are force constants between Sr-Sr, O-Sr and O-O. The inset shows the density dependence of the remaining IFCs

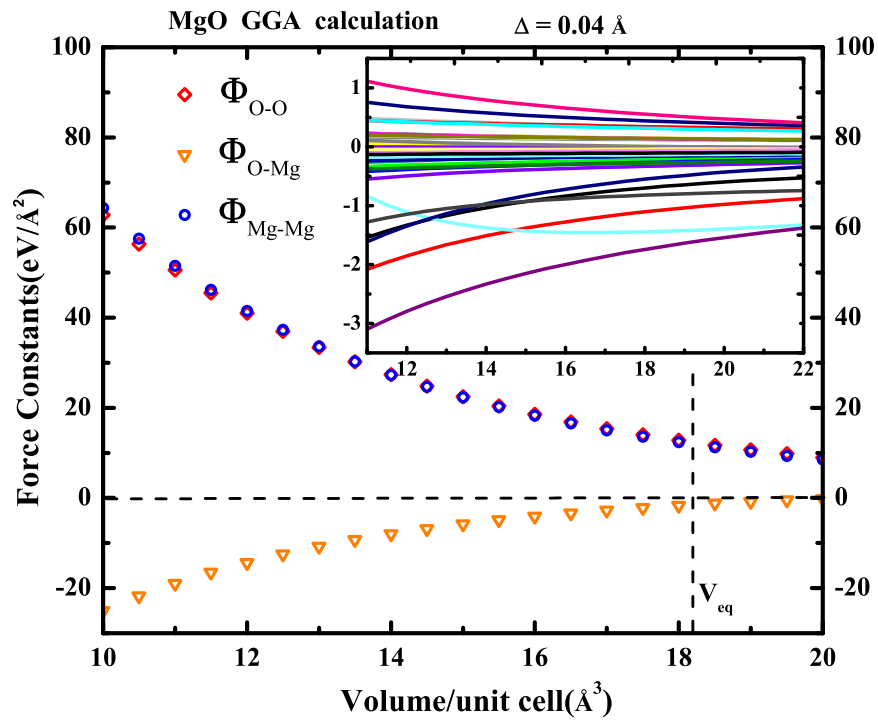


Figure B.5: Volume dependence of Force constants in MgO. Main: IFCs between Mg-Mg, O-Mg and O-O. Inset: Rest of the IFCs.

Table B.1: Fitting parameters a_0 , a_1 , a_2 , a_3 for the 52 independent harmonic force constants of MgO fitted to third order according to equation B.1. The original LDA calculated harmonic force constants were extracted based on a 128-atom supercell and a finite atomic displacement $\Delta = 0.04 \text{ \AA}$. $ii = (ia - 1) * Ns + idir$,
 $jj = (ja - 1) * Ns + jdir$. Where $(ia, ja) = 1$ to 128 and $Ns=3$

ii	jj	a_0 (eV \AA^{-2})	a_1 (eV)	a_2 (eV \AA^2)	a_3 (eV \AA^4)
1	1	92.47391711	- 1718.68492426	9513.01862554	- 10341.25717161
1	4	- 0.40482956	6.49643673	- 50.47378240	- 35.91076121
1	5	- 0.17783410	0.30949676	- 36.67019948	- 43.94750904
1	7	0.53994533	- 10.76994845	53.72063476	- 107.40040433
1	8	0.37080575	- 7.53578988	31.35209757	- 65.40606807
1	16	0.01730697	- 0.49509185	- 7.81719061	21.56255900
1	17	0.13912270	- 2.51110079	6.74094948	- 7.211171552
1	19	- 0.05807758	0.98499042	- 5.47536188	10.67920890
1	21	- 0.05531149	1.11998260	- 2.78379867	2.45922988
1	22	- 1.22095350	22.96027588	- 113.37737647	231.52908879
1	31	0.34524746	- 6.20819702	39.39422950	- 77.29218029
1	64	0.16080048	- 3.04080758	14.23910972	- 24.40120860
1	70	0.99249115	- 17.84161631	114.09655148	- 220.87478657
1	79	- 0.50588086	9.02857233	- 51.75492914	95.66906824
1	82	0.28496069	- 5.23341210	26.09410055	- 48.12514085
1	84	0.14895321	- 2.70672078	11.64119048	- 20.46924927
1	94	1.51639353	- 28.53442043	152.16348598	- 300.70442071
1	127	0.68312471	- 12.33400267	68.40260069	- 125.81115843
1	193	0.00193383	- 0.79754313	7.08808208	- 21.91981947
1	194	- 0.45313432	8.47513272	- 25.01964235	27.05598007
1	196	- 0.11916618	1.87574547	- 4.71566224	6.88718954
1	197	- 0.19734462	3.83688393	- 12.86162054	19.16890443
1	202	0.40561829	- 4.47310995	- 180.15834192	848.42384002
1	208	- 0.06743555	1.10193891	- 6.02138866	10.28276693
1	211	0.17313127	- 3.08862312	13.15758171	- 24.99260162
1	214	- 0.37560994	6.78677966	- 42.39902043	85.27290568
1	216	- 0.33670298	8.30745970	- 33.05358760	52.30120608
1	223	- 0.00007024	0.14532545	3.24479382	- 8.87989198
1	224	- 0.06653759	1.38235819	- 4.92958327	7.32881241
1	226	- 0.61500325	11.89659663	- 50.50666734	85.62592642
1	228	- 0.30876852	5.72822889	- 24.97879821	48.41965778
1	238	- 43.18835776	804.52823771	- 4054.14648323	3410.42072467
1	259	- 0.23835309	4.51025336	- 23.89790863	41.51155741
1	271	- 0.60784654	11.47865189	- 58.30196984	103.42874279
193	193	77.71621195	- 1443.35035960	7783.51846977	- 6646.35810740
193	196	1.28008731	- 21.86394086	124.70053340	- 420.54143451
193	197	1.95716047	- 38.57045061	144.07149558	- 360.73823814
193	199	0.30112093	- 4.43579562	20.44040415	- 42.14864279
193	200	0.23494728	- 5.86283241	21.43306968	- 35.01362786
193	208	0.20159417	- 3.13639796	6.76555682	- 11.54059049
193	209	0.20895303	- 4.18091948	14.54034306	- 21.96807984
193	211	- 0.00253489	0.06808854	0.05610270	- 1.69263644
193	213	- 0.04190171	0.39104627	- 2.42241567	7.81401863
193	214	- 0.72810237	11.62803953	- 34.78894406	103.15658186
193	223	0.00514154	- 0.12667549	4.87967830	- 9.53843389
193	256	0.08221283	- 1.33803224	3.58785005	- 7.55114810
193	262	0.56285035	- 11.29421051	67.71731699	- 112.13662209
193	271	- 0.08423031	1.07591453	- 7.55637038	16.43573280
193	274	0.29945488	- 6.19568117	29.59797576	- 51.39155161
193	276	0.15848508	- 2.79811492	11.14573352	- 18.49262242
193	286	0.18605395	- 16.68427019	120.61658739	- 359.72292314
193	319	0.40464050	- 7.95578245	41.07855666	- 72.20951864

APPENDIX C

THERMAL EQUATION OF STATE OF Al_2O_3

Static EOS

The present calculation is a repeat of previous calculation done by Bin Xu a former member of our research group¹¹⁹. The previous calculation by Bin, is well reproduced to within 3 % and our new data is consistent with previous calculations and experiments.

Table C.1: Third-order BM-EOS parameters for $\alpha\text{-Al}_2\text{O}_3$

Source	V_0 ($\text{\AA}^3/\text{atom}$)	K (GPa)	K'
Static calculation			
LDA+PAW (this work)	8.354	256.5	4.200
Calculation ⁷¹	8.441	258.9	4.01
Calculation ¹²⁶	8.10	248	4.13
Calculation ⁷³	8.486	252.6	4.237
300 K (QHA)			
LDA+PAW (this work)	8.526	235.06	4.000
Calculation ¹⁶³	8.498	251.0	4.04
Experiment ¹⁶⁴	8.484	254.4	4.275

Thermal EOS

Table C.2: Gibbs Free energy (F_0), Volume per unit cell(V_0), Bulk modulus (B_0) and derivative of bulk modulus (B'_0) at 0 GPa

T(K)	F_0 (eV/atom)	V_0 (\AA^3)	B_0 (GPa)	B'_0
300	-8.18302100	85.2618400	235.06238000	4.00336200
500	-8.21569000	85.6318600	228.98451400	4.09717000
1000	-8.36735800	86.8357200	211.67306800	4.35688500
1500	-8.58576600	88.2734500	192.45940900	4.64781800
2000	-8.85050700	89.9599700	171.34529700	4.98039700

Figure C.2 shows our LDA calculated thermal EOS derived within the quasi-harmonic approximation (QHA), together with measurements from experiments^{165–169} at 0 GPa and 300 K

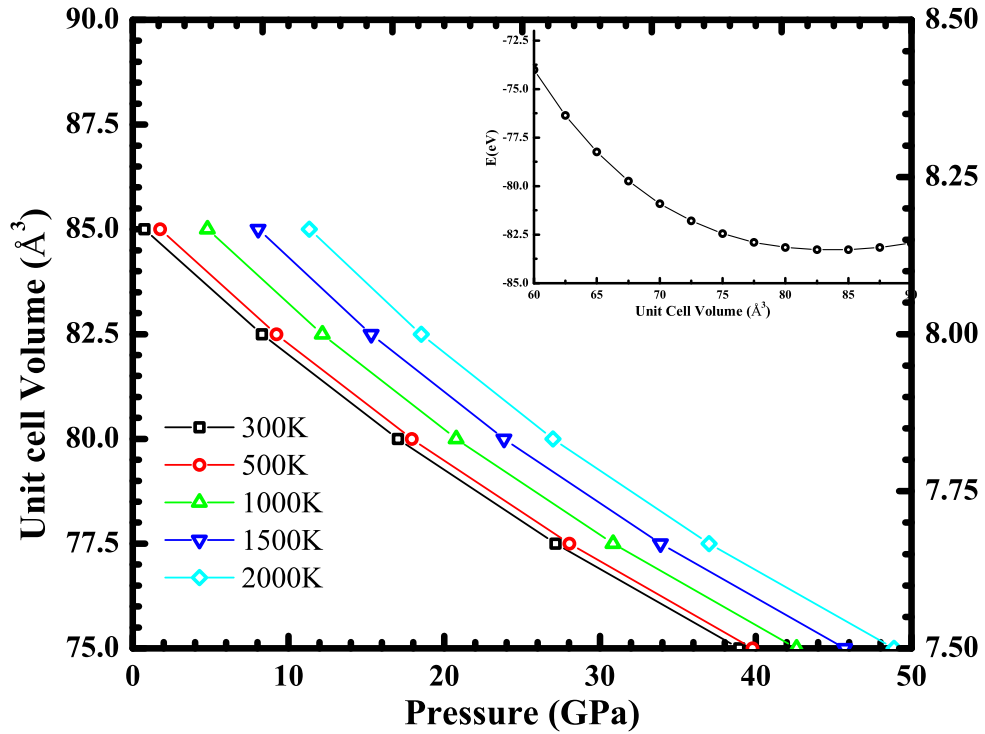


Figure C.1: Main: Volume-pressure relationship in α -Alumina at five temperature points: 300K, 500K, 100K, 1500K, 2000K. Inset: Static EOS fitted to 3rd order Birch Murnaghan EOS

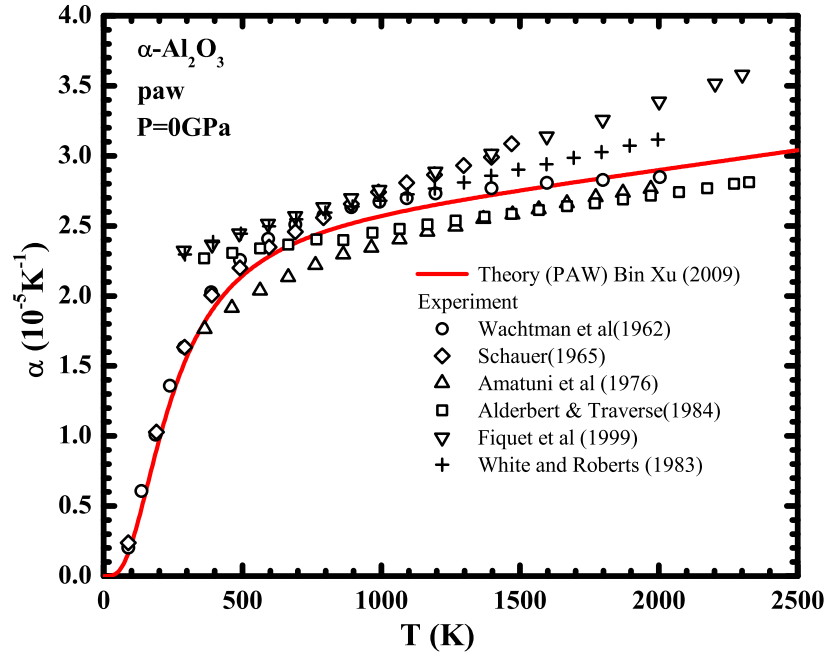


Figure C.2: Thermal EOS from first-principles theoretical calculation(LDA +PAW) compared with measurements. Discreet symbols represent measurements done by Wachtman et al., 1962; Schauer, 1965; Amatuni et al., 1976; Adelber & Traverse, 1984; Fiquet et al., 1999 and White & Roberts, 1983. Red solid line represents a reproduction of LDA+PAW calculation previously done by Bin Xu, 2009(former member of our research team)

APPENDIX D

EQUATIONS OF STATE (EOS) PV-MgSiO₃ AND LATTICE DYNAMICS OF PPV-MgSiO₃

D.1 Static Equation of State

Total energies at fixed unit cell volumes ranging from 122 Å³ to 160 Å³ were calculated using the VASP package with PAW method. An $8 \times 8 \times 6$ Monkhorst-Park k-points grid was used to sample the first Brillouin zone. The following energy cutoff parameters were used in the *INCAR* file.

- System = PV INCAR static
- NSW = 999
- ISIF = 4
- ENCUT = 600.00
- EDIFF = 1E-9
- LWAVE= .FALSE.
- LCHARG= .FALSE.

Table D.1: Static EOS parameters of MgSiO₃ PV and PPV fitted to 3rd order BM EOS at ambient conditions

	V ₀ (cm ³ per mol)	B ₀ (GPa)	B' ₀
PV(This work: LDA)	24.15	248.56	3.84
PPV(This work: LDA)	24.08	227.75	4.0
PV(Theory ⁹² :LDA)	24.71	246.1	4.0
PPV(Theory ⁹² : LDA)	24.66	215	4.41

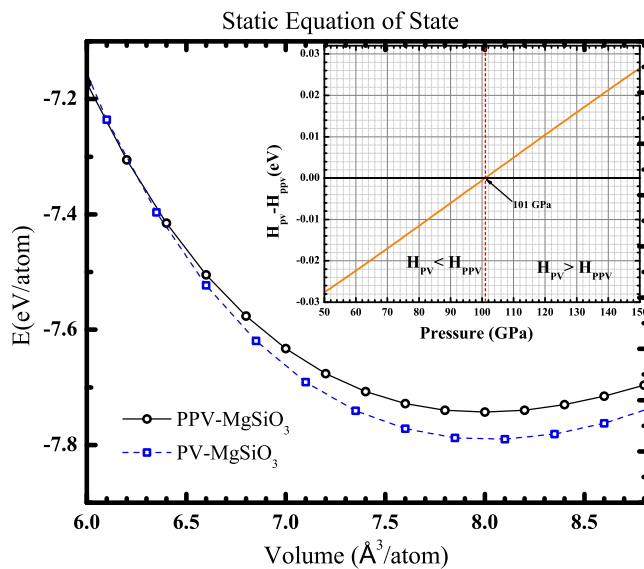


Figure D.1: Main: Static EOS of MgSiO₃ fitted to 3rd order Birch-Murnaghan EOS. Inset: Difference in enthalpies of PV and PPV phases plotted as a function of pressure. Our calculation predicts that at ambient temperature, the PV→PPV transition occurs at 101 GPa which is consistent other theoretical predictions for example Tsuchiya et al. (2004).

D.2 Thermal EOS of PV-MgSiO₃

Table D.2: LDA calculated thermal EOS parameters for PV-MgSiO₃ at 0 GPa. Values in parentheses are from Tsuchiya et al. (2005)

T(K)	V ₀ (cm ³ /mol)	K ₀ (GPa)	K' ₀
1.00	24.31	249.36317700	3.92435100
300.00	24.38 (24.71)	243.63925300 (246.1)	3.97535500(4.00)
1000.00	24.95	216.84633000	4.14579900
1500.00	25.46	196.36412500	4.27543300
2000.00	26.03	175.07605500	4.41773400
2500.00	26.76	152.94810800	4.57829400
3000.00	27.60	129.90054500	4.76629500
3500.00	28.68	105.80279200	4.99892500

Figure D.2 shows our LDA calculated P-V-T relations together with previous calculations and experiment for comparison. Our results agree well with previous calculations. In our calculation of lattice thermal conductivity, we need the pressure dependence of simulation cell volumes, to be able convert our calculated isochoric thermal conductivity to isobaric conditions for comparison with experiments, since experiments are usually carried out under isobaric conditions. Figure D.3 presents our calculated thermal expansivity together with previous calculations and experiment. Our LDA calculated thermal EOS is consistent with both previous calculations and experiment.

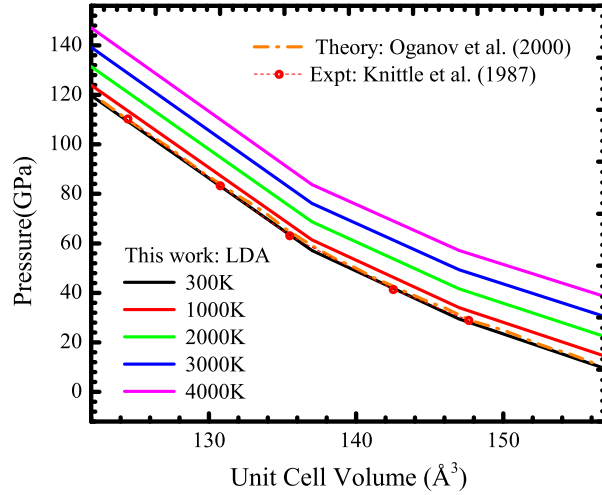


Figure D.2: P-V-T isotherms in PV-MgSiO₃ derived within the QHA. Solid lines represent our LDA calculation, dashed lines represent previous calculation by Oganov et al. (2000), circles denote Experimental measurement by Knittle et al. (1987)

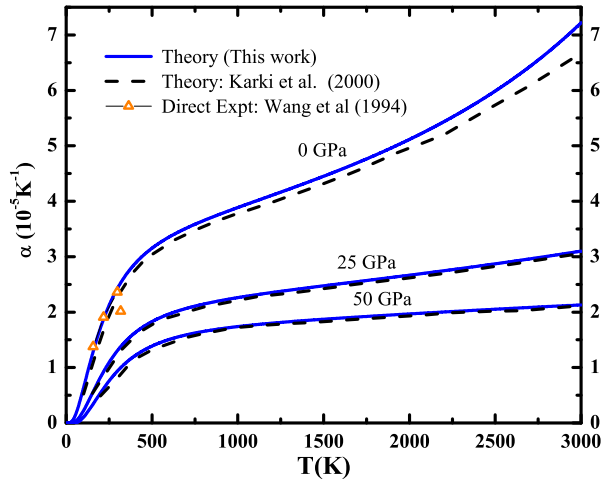


Figure D.3: Thermal EOS of PV-MgSiO₃ derived within the QHA. Solid lines represent our LDA calculation, dashed lines represent previous calculation by Karki et al. (2000), Discrete symbols are experimental measurement by Wang et al. (1994)

D.3 Lattice Dynamics of PPV-MgSiO₃

Using standard first-principles total energy and force calculations we have calculated the harmonic force constant matrices and third order lattice anharmonicity tensors of PPV-MgSiO₃ using an efficient real space super-cell finite-difference algorithm. Phonon spectra derived from the force constant matrices agree well with experiment and previous calculations.

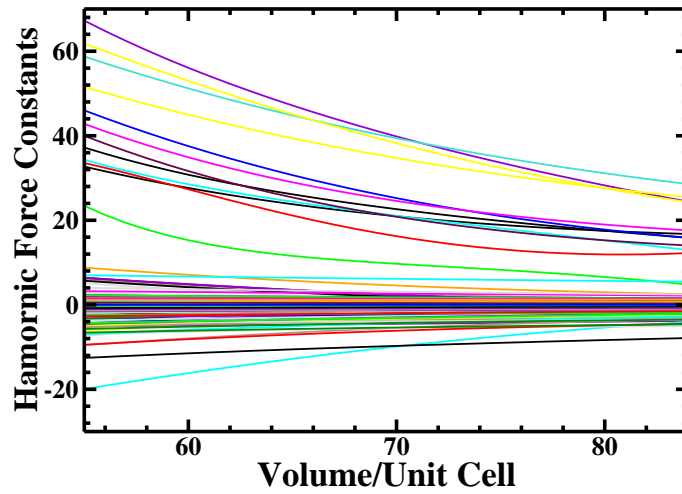


Figure D.4: Density dependence of harmonic force constants ($\text{eV}/\text{\AA}^2$) in PPV-MgSiO₃. Independent force constants shown for 160-atom periodic supercells of PPV.

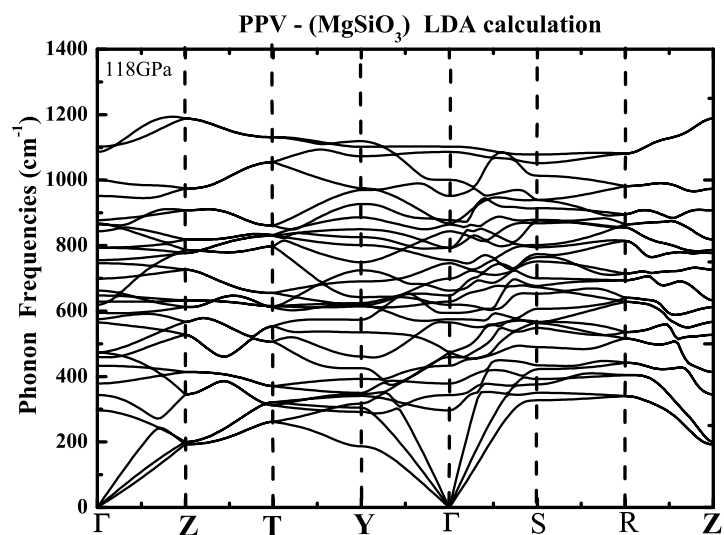


Figure D.5: LDA calculated phonon mode frequencies in PPV-MgSiO₃ at 118 GPa

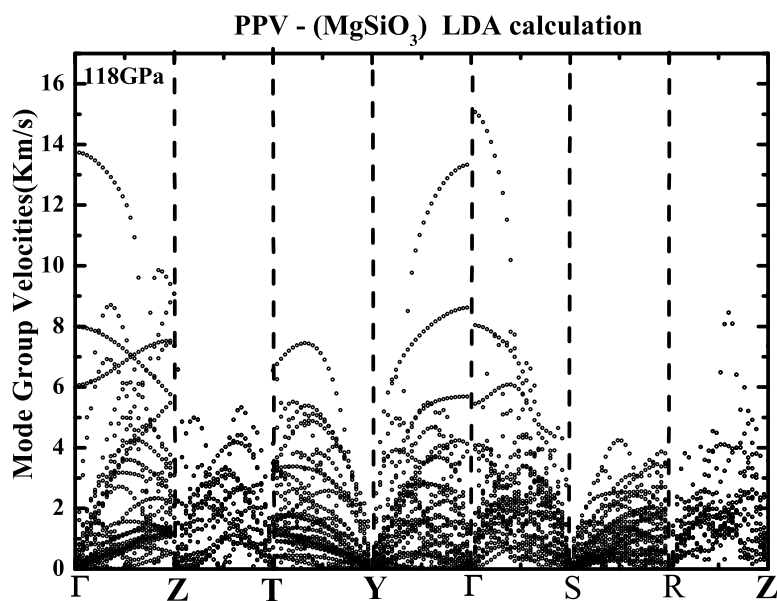


Figure D.6: LDA calculated phonon mode group velocities in PPV-MgSiO₃ at 118GPa. Mode group velocities in PPV are of the same order of magnitude as those in PV at corresponding pressure.

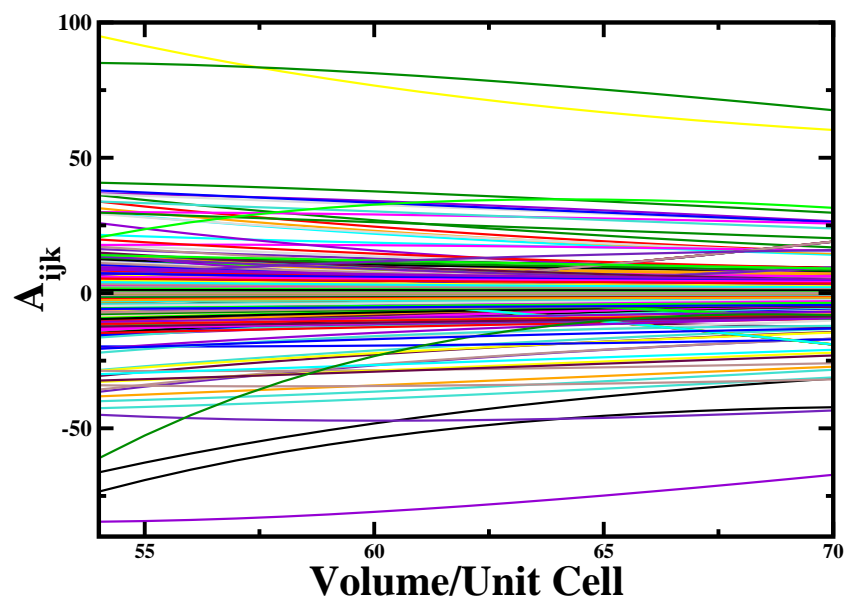


Figure D.7: Density dependence of 3^{rd} order lattice anharmonicity tensor elements ($\text{eV}/\text{\AA}^3$) in PPV-MgSiO₃. Most third order lattice anharmonicity tensors are insensitive to the change in volume/density. A few terms show a decreasing trend with compression.

APPENDIX E

DENSITY DEPENDENCE OF PHONON LIFETIMES IN PV-MgSiO₃

The volume dependence of the lifetimes of the 60 phonon modes at all the 100 irreducible directions (K-points) of the BZ are shown in figures E.1 to E.17. To our knowledge this is the first explicit ab initio calculation of density dependence of anharmonicity induced phonon scattering rates. Different modes are observed to have different density/pressure dependencies. Lifetimes of most phonon modes are seen to increase with decreasing volume (increasing pressure). Overall our calculation reveals a weak pressure dependence of phonon lifetimes. The variation of the phonon mode lifetimes with volume is almost linear. Table E.1 shows the Volumes and thermal EOS-derived pressures at 300 K for which we directly calculated the phonon lifetimes.

Table E.1: Simulation cell volumes and corresponding pressures for PV-MgSiO₃ at 300 K.

V_0 (Å ³)	122	127	137	147	157
P (GPa)	119.68	95.26	57.10	29.45	9.21

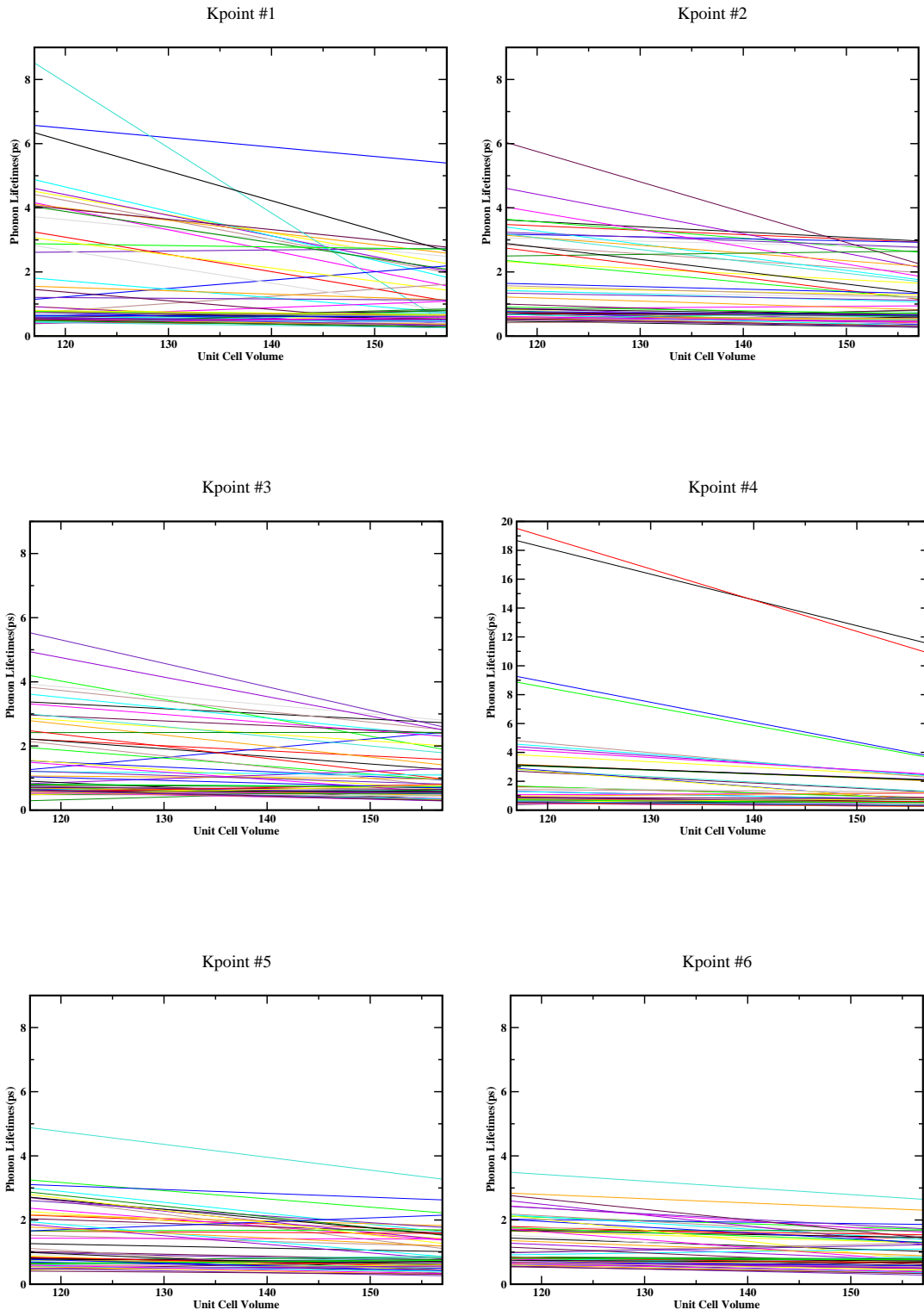


Figure E.1: Density dependence of phonon lifetimes for 60 phonon modes at irreducible K-points #1-6 in BZ

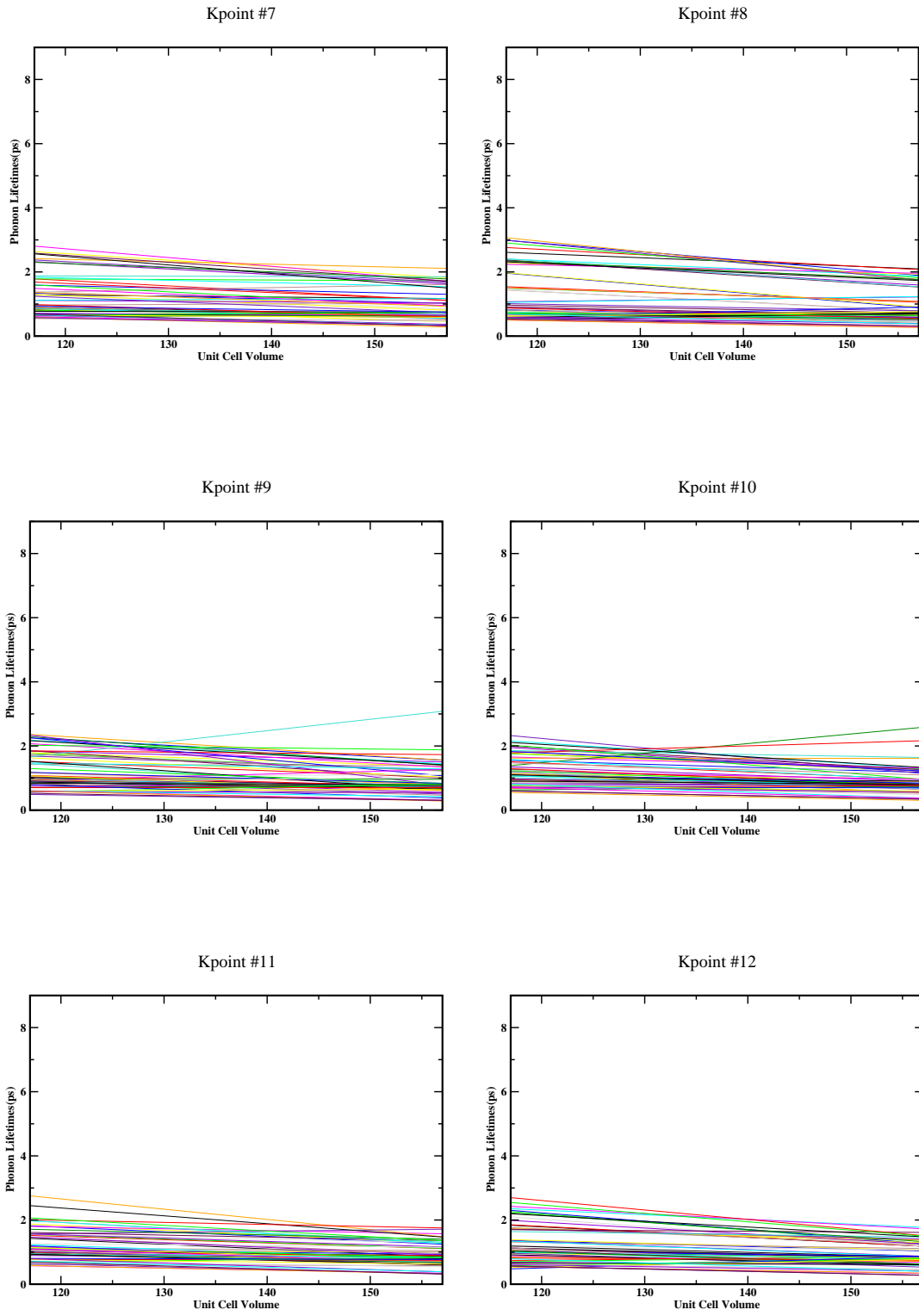


Figure E.2: Density dependence of phonon lifetimes for 60 phonon modes at irreducible K-points #7-12 in BZ

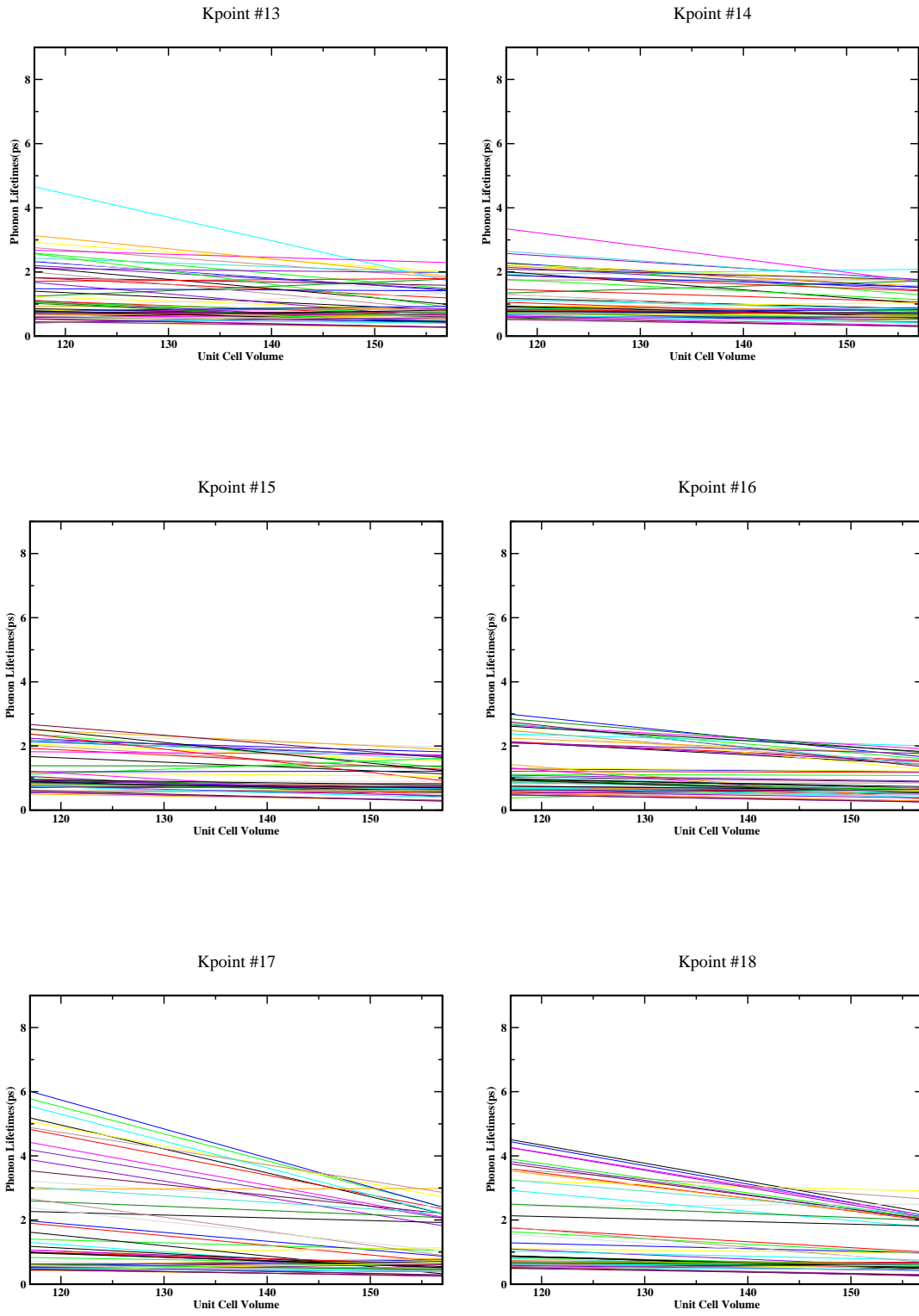


Figure E.3: Density dependence of phonon lifetimes for 60 phonon modes at irreducible K-points #13-18 in BZ

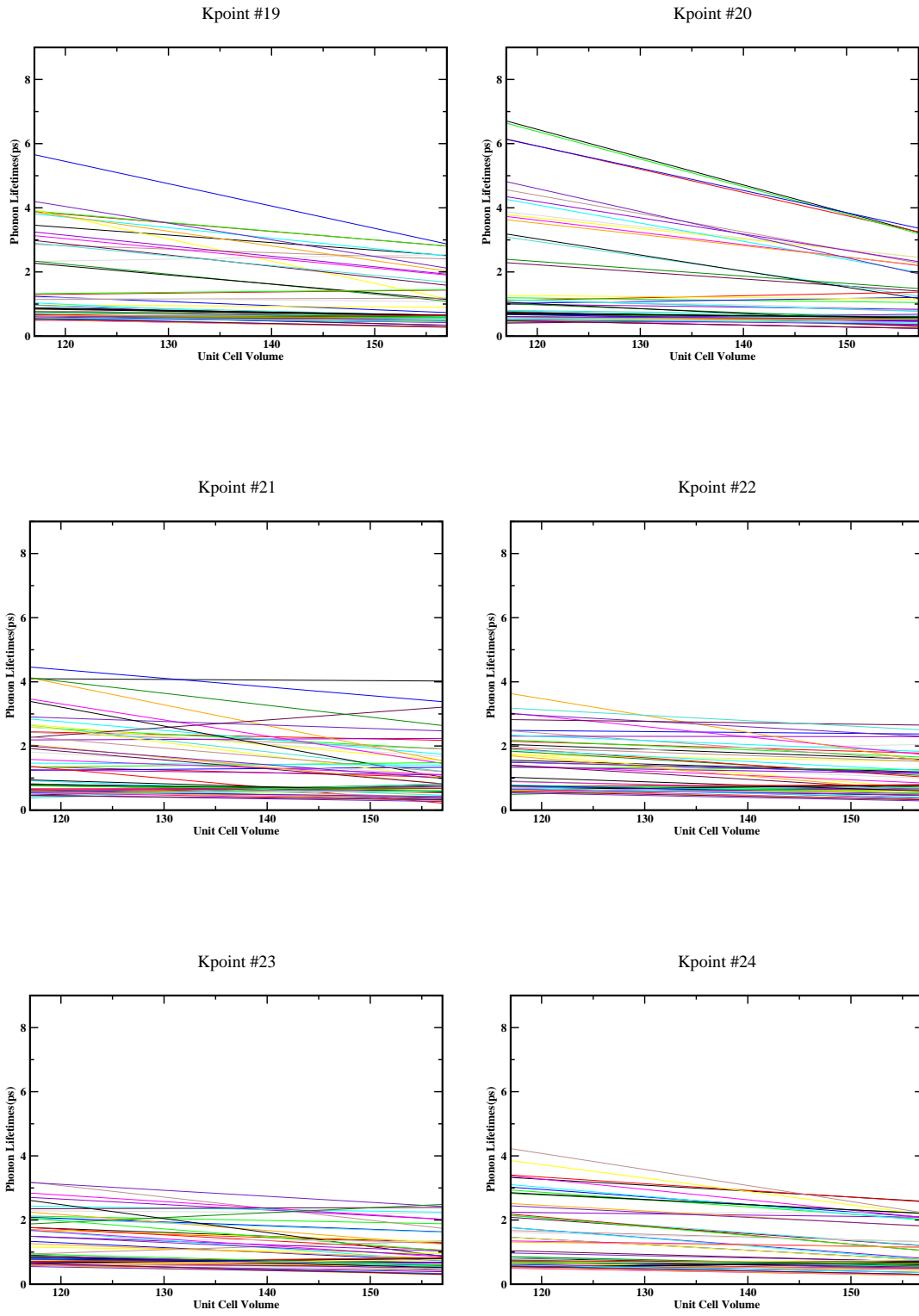


Figure E.4: Density dependence of phonon lifetimes for 60 phonon modes at irreducible K-points #19-24 in BZ

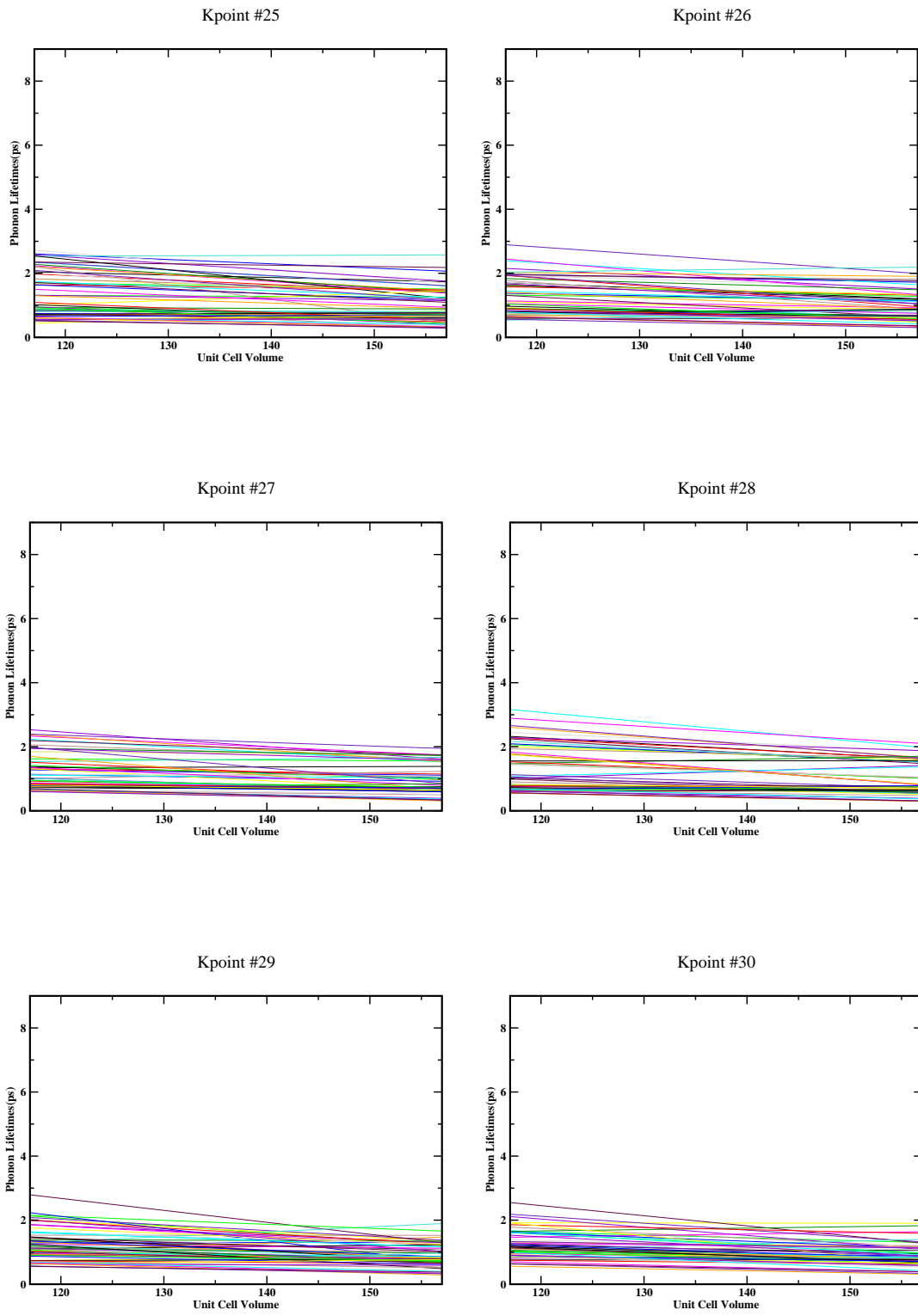


Figure E.5: Density dependence of phonon lifetimes for 60 phonon modes at irreducible K-points #25-30 in BZ

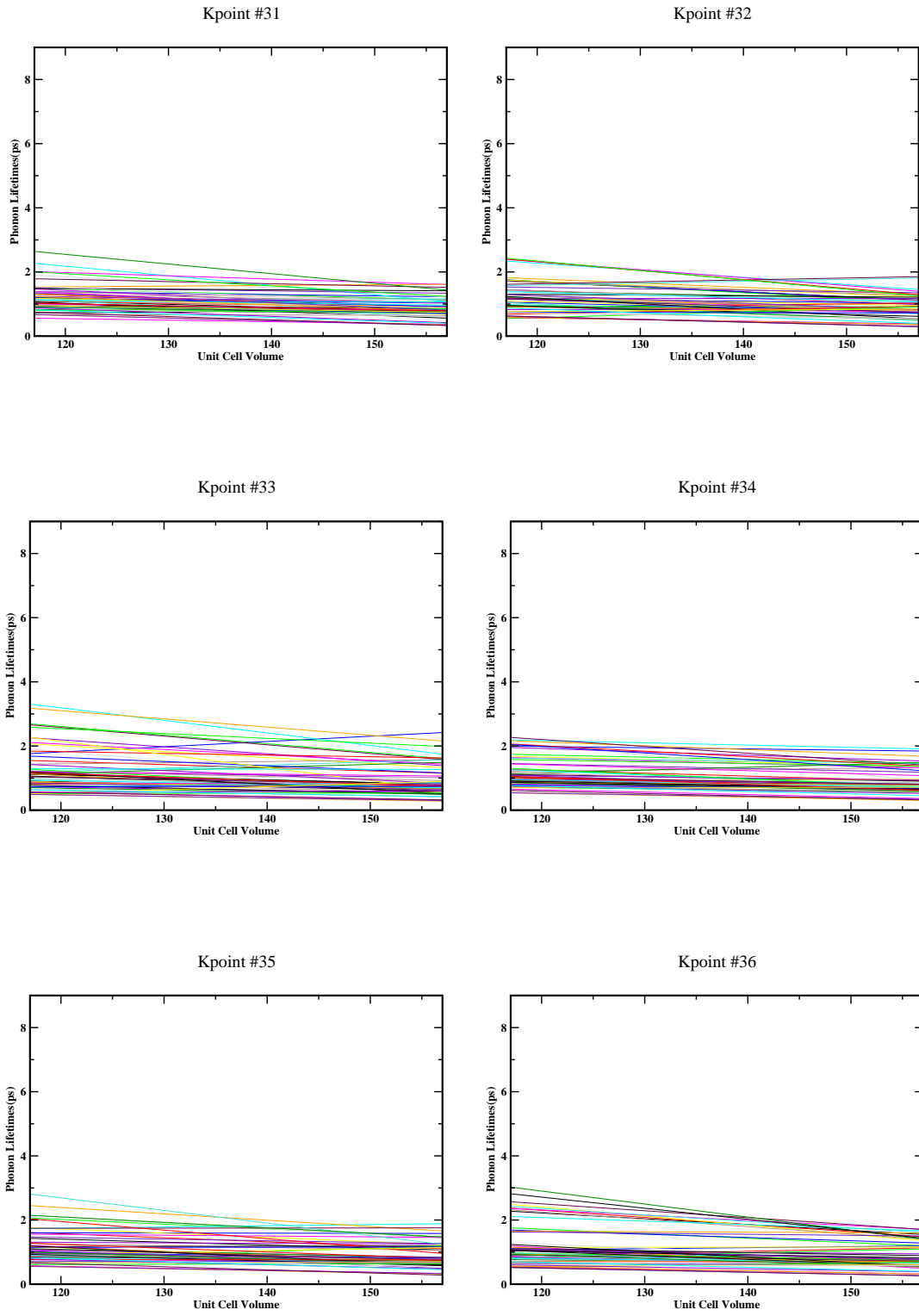


Figure E.6: Density dependence of phonon lifetimes for 60 phonon modes at irreducible K-points #31-36 in BZ

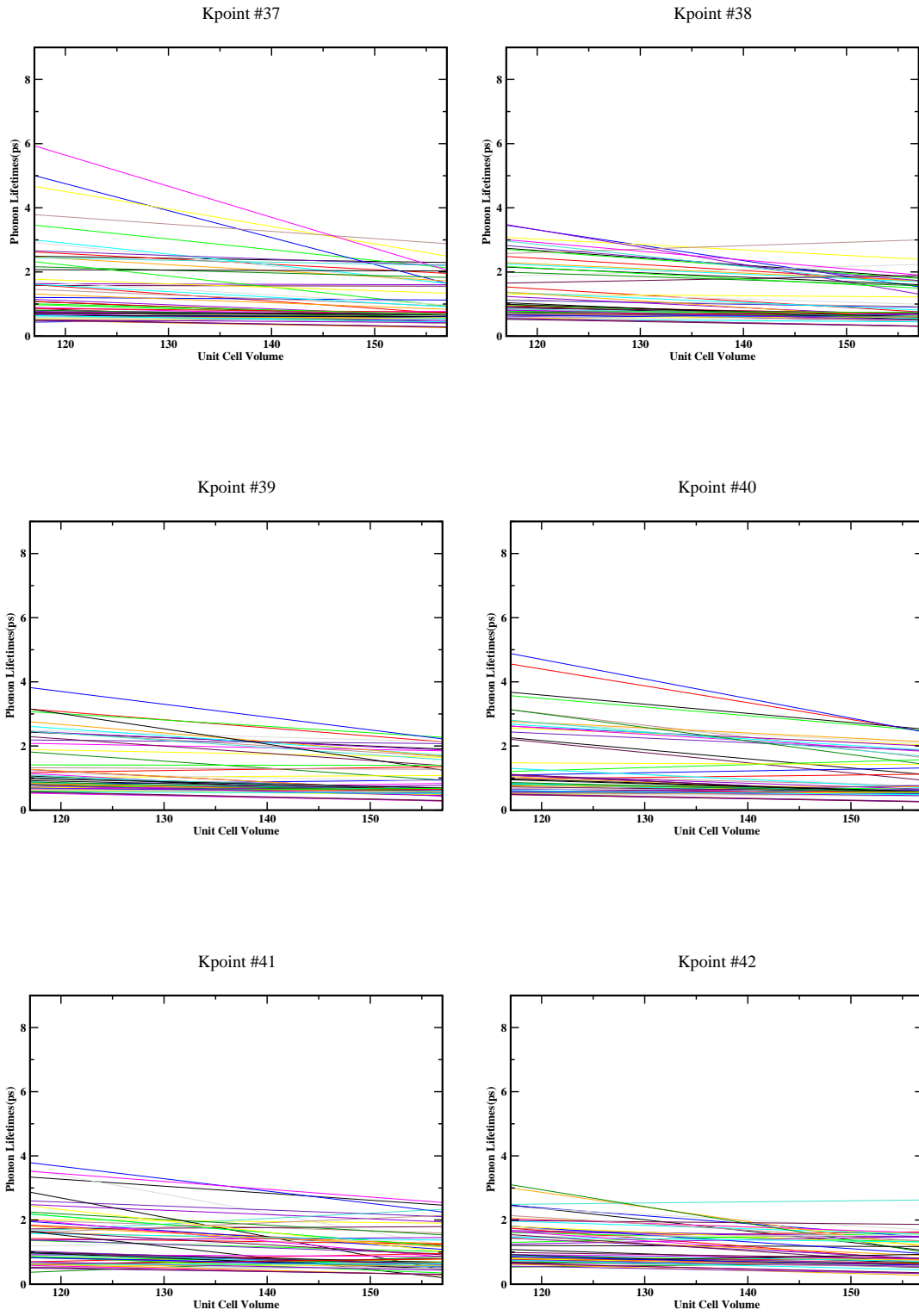


Figure E.7: Density dependence of phonon lifetimes for 60 phonon modes at irreducible K-points #37-42 in BZ

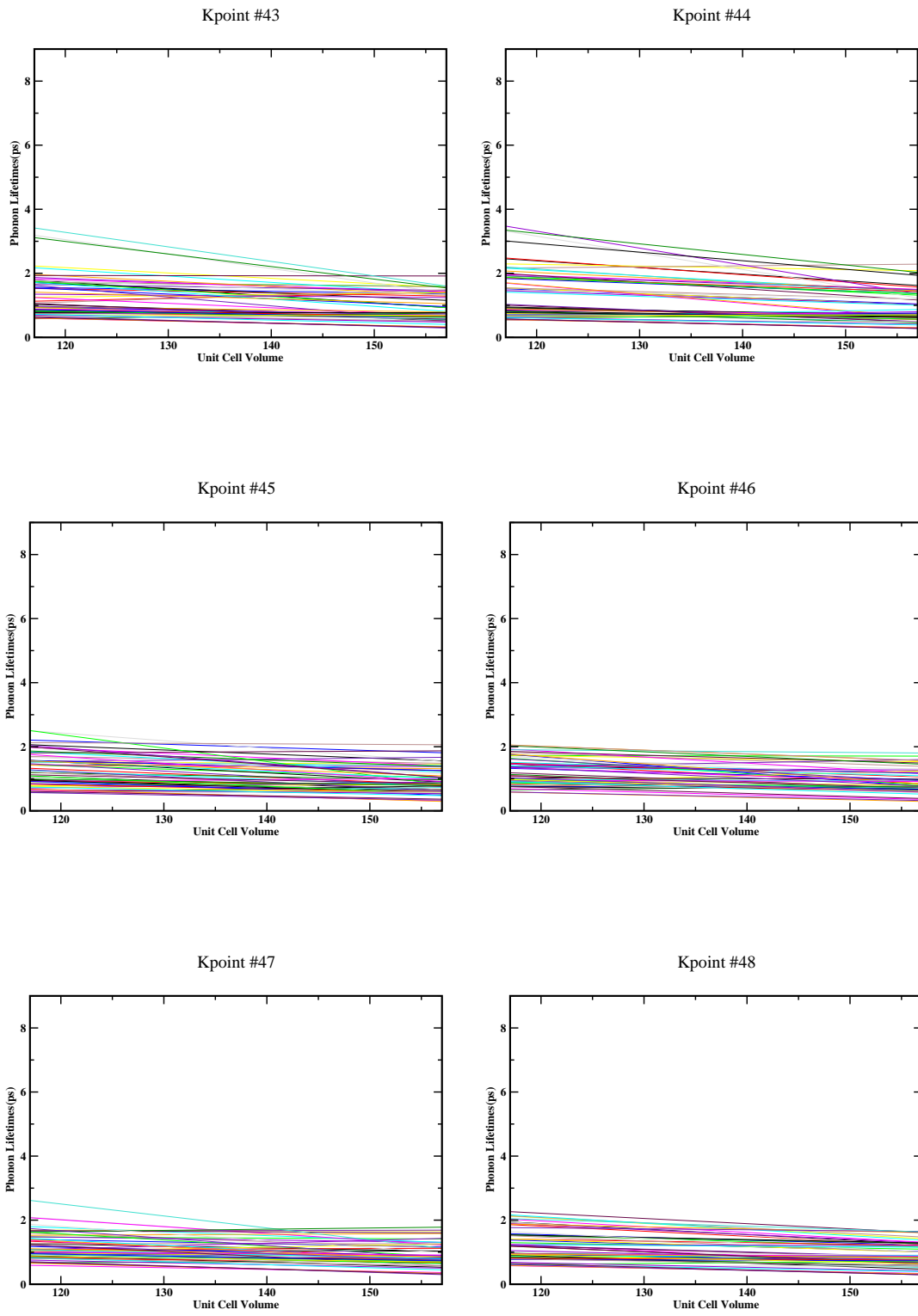


Figure E.8: Density dependence of phonon lifetimes for 60 phonon modes at irreducible K-points #43-48 in BZ

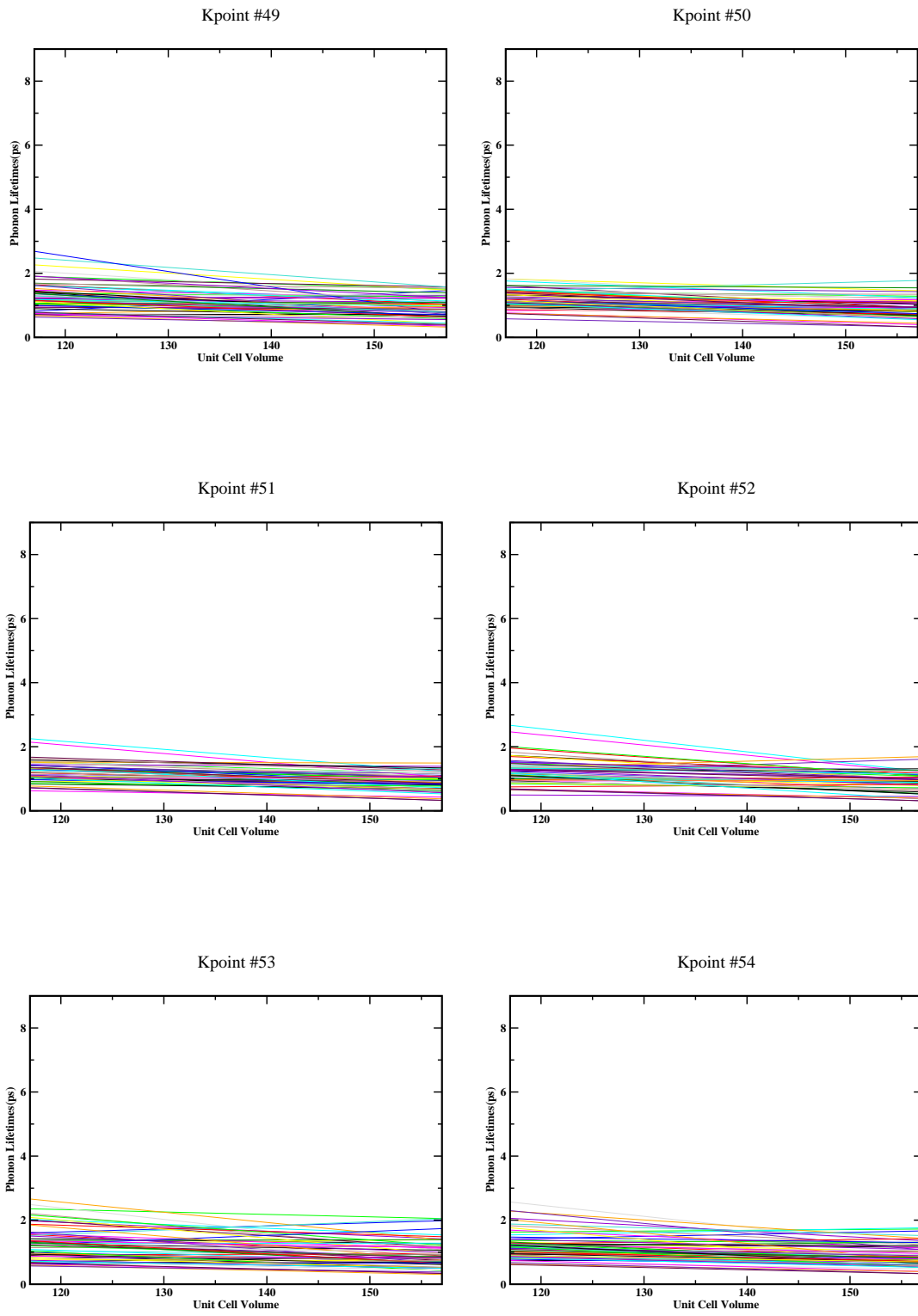


Figure E.9: Density dependence of phonon lifetimes for 60 phonon modes at irreducible K-points #49-54 in BZ

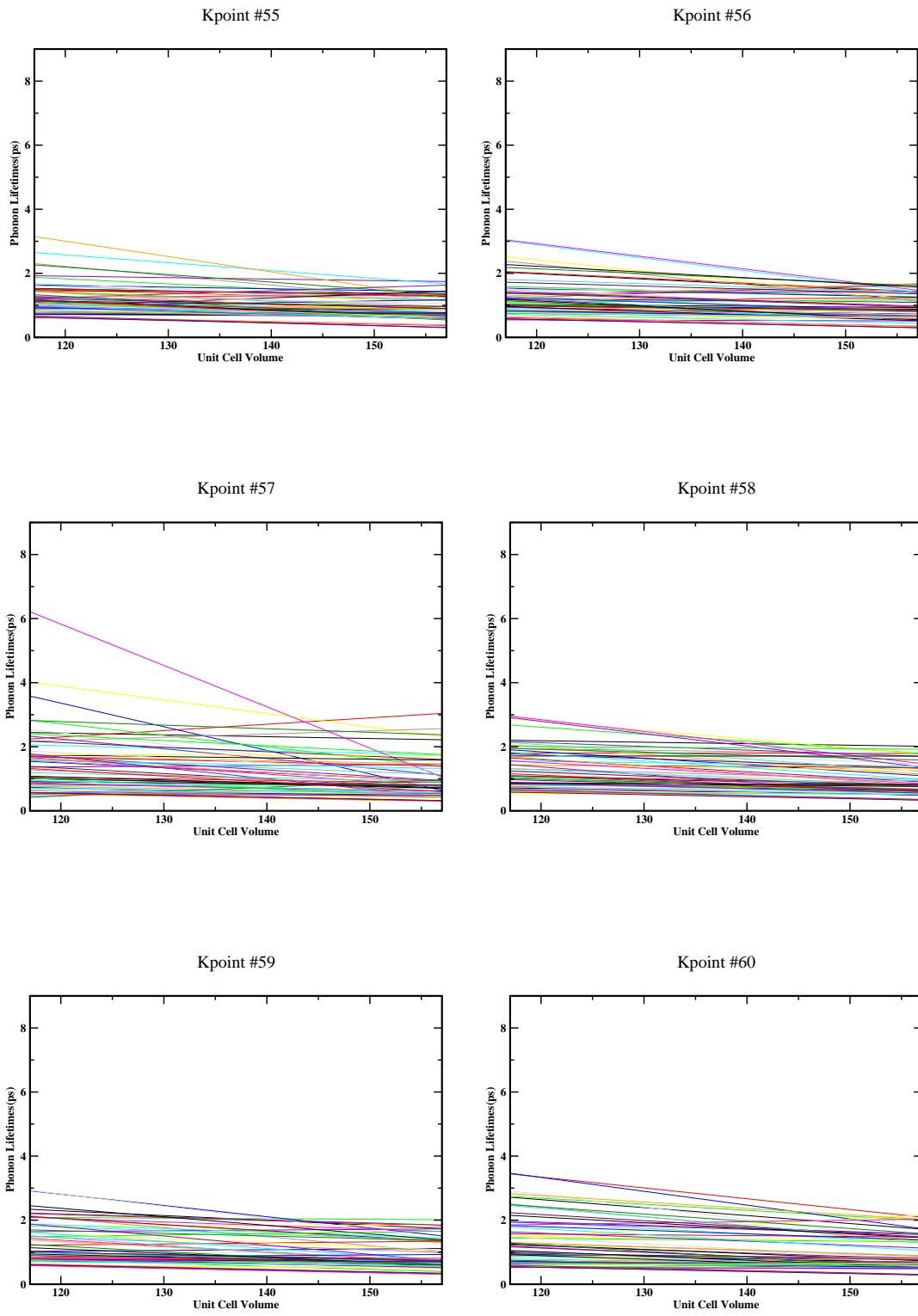


Figure E.10: Density dependence of phonon lifetimes for 60 phonon modes at irreducible K-points #55-60 in BZ

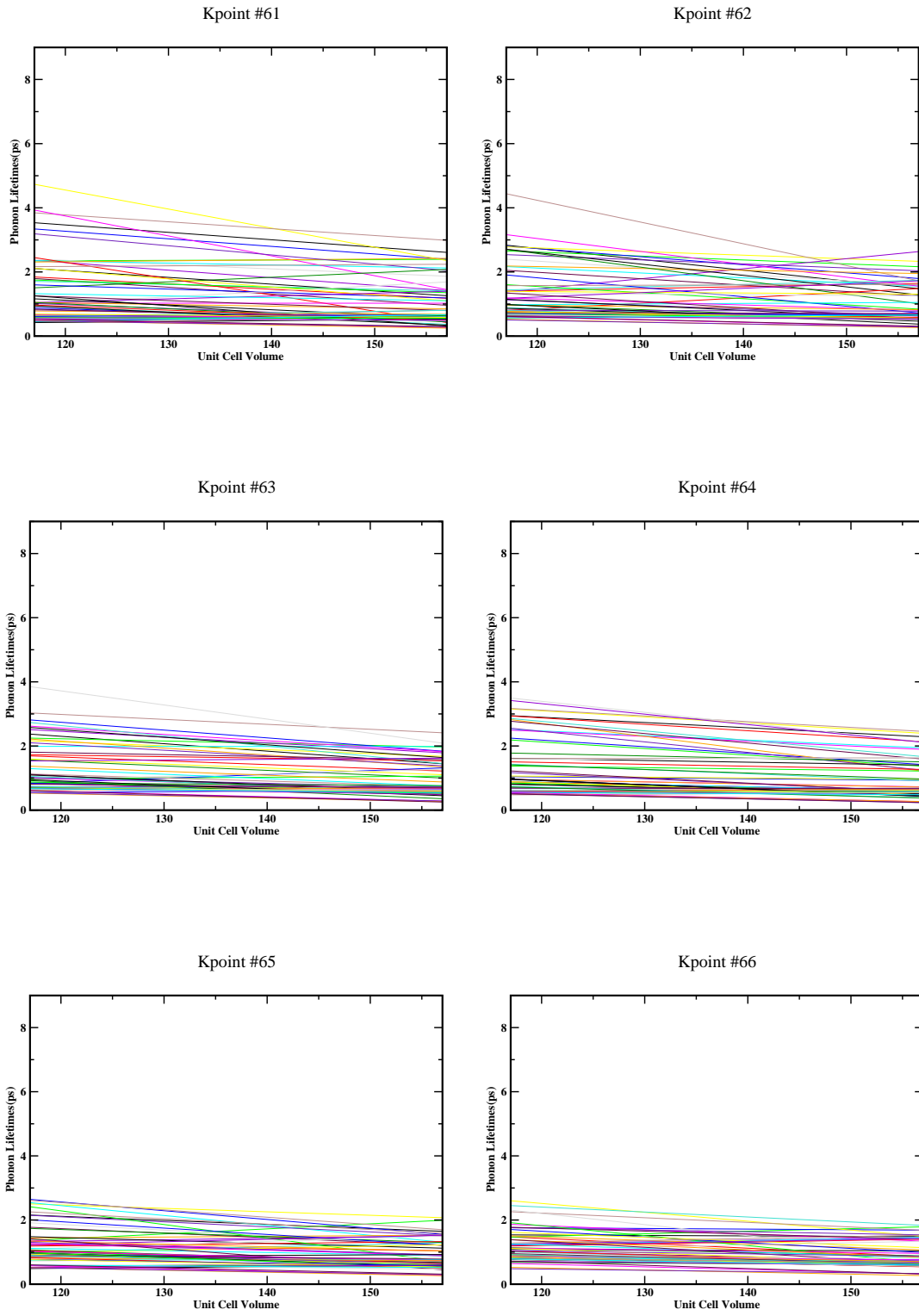


Figure E.11: Density dependence of phonon lifetimes for 60 phonon modes at irreducible K-points #61-66 in BZ

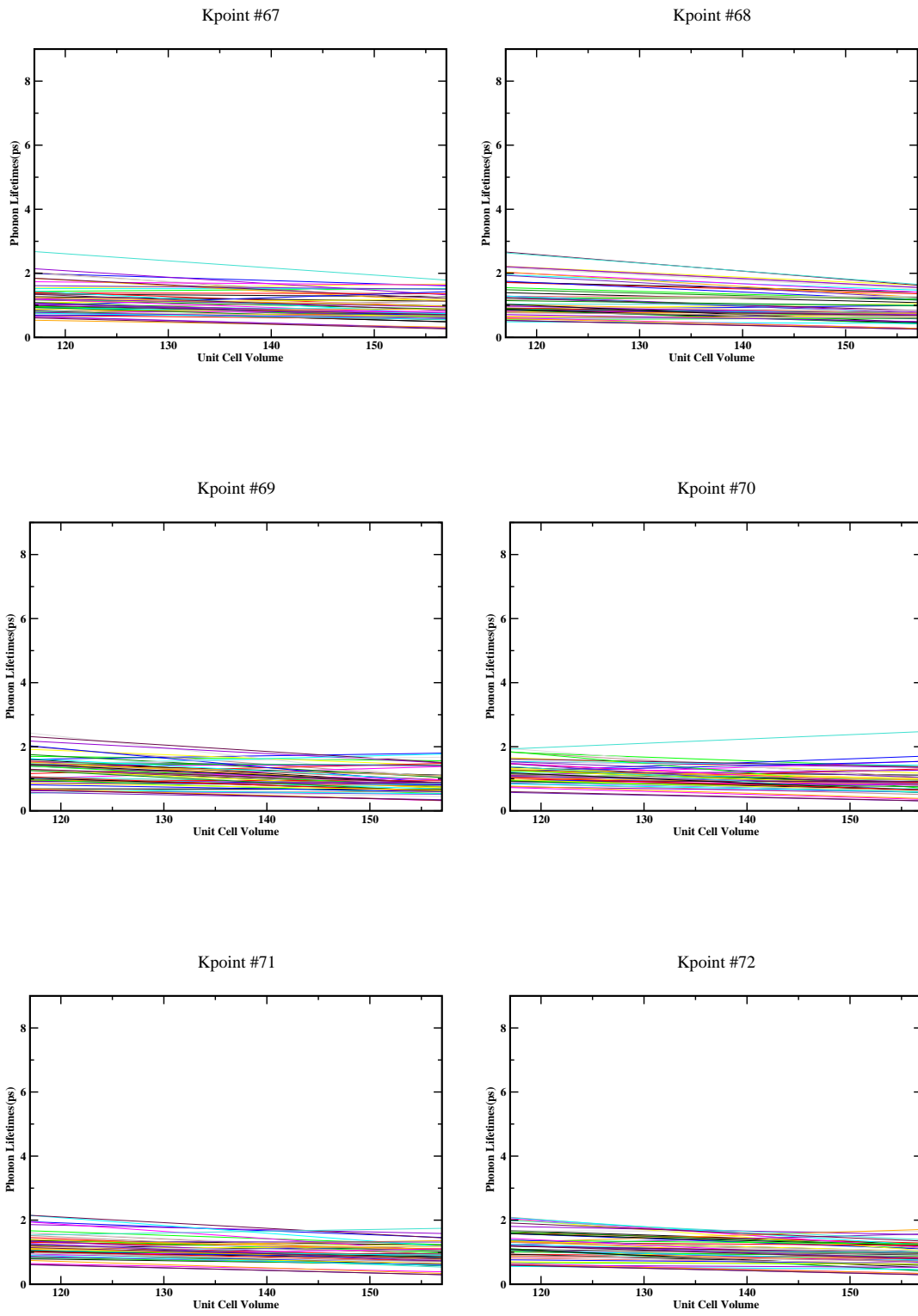


Figure E.12: Density dependence of phonon lifetimes for 60 phonon modes at irreducible K-points #67-72 in BZ

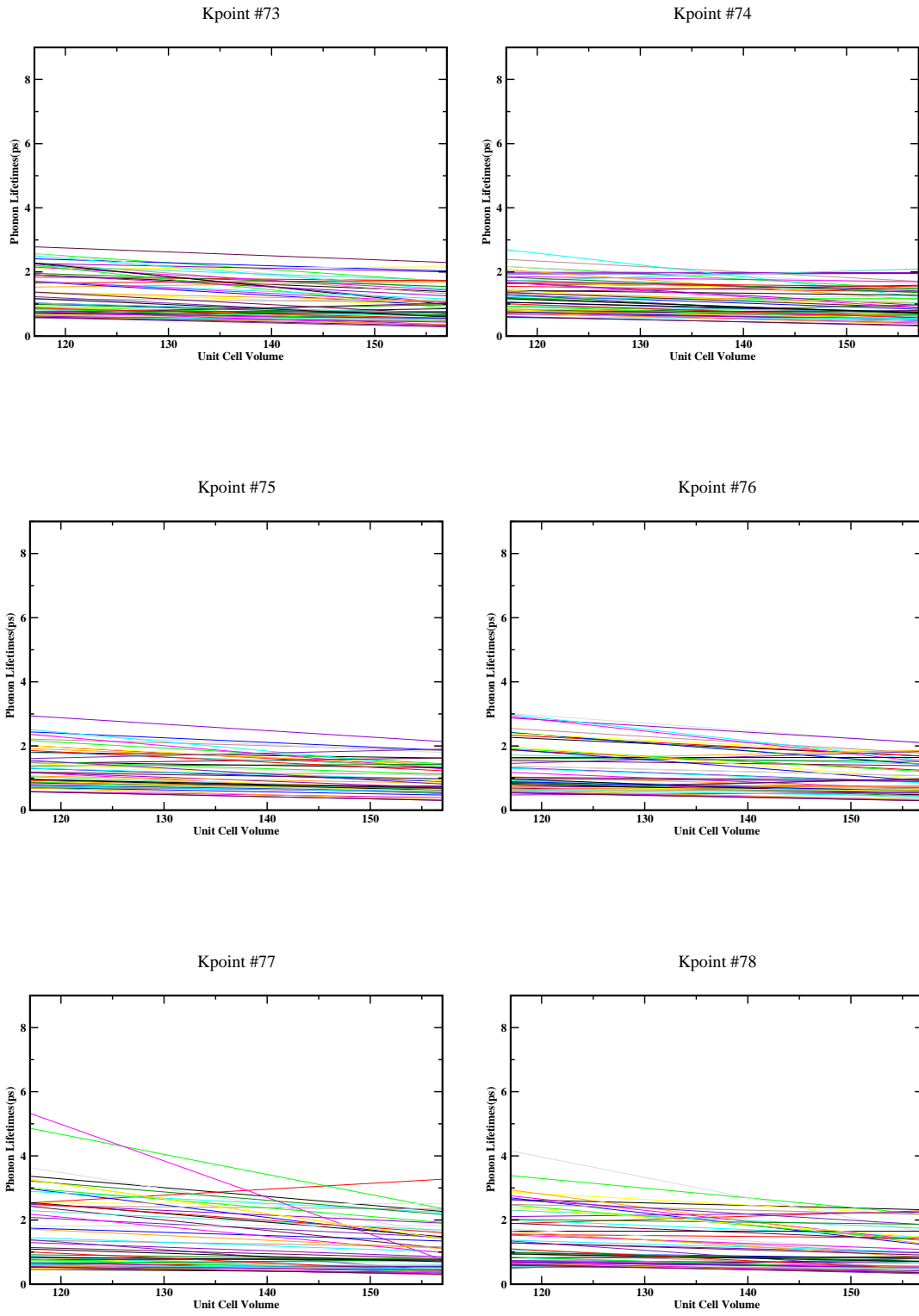


Figure E.13: Density dependence of phonon lifetimes for 60 phonon modes at irreducible K-points #73-78 in BZ

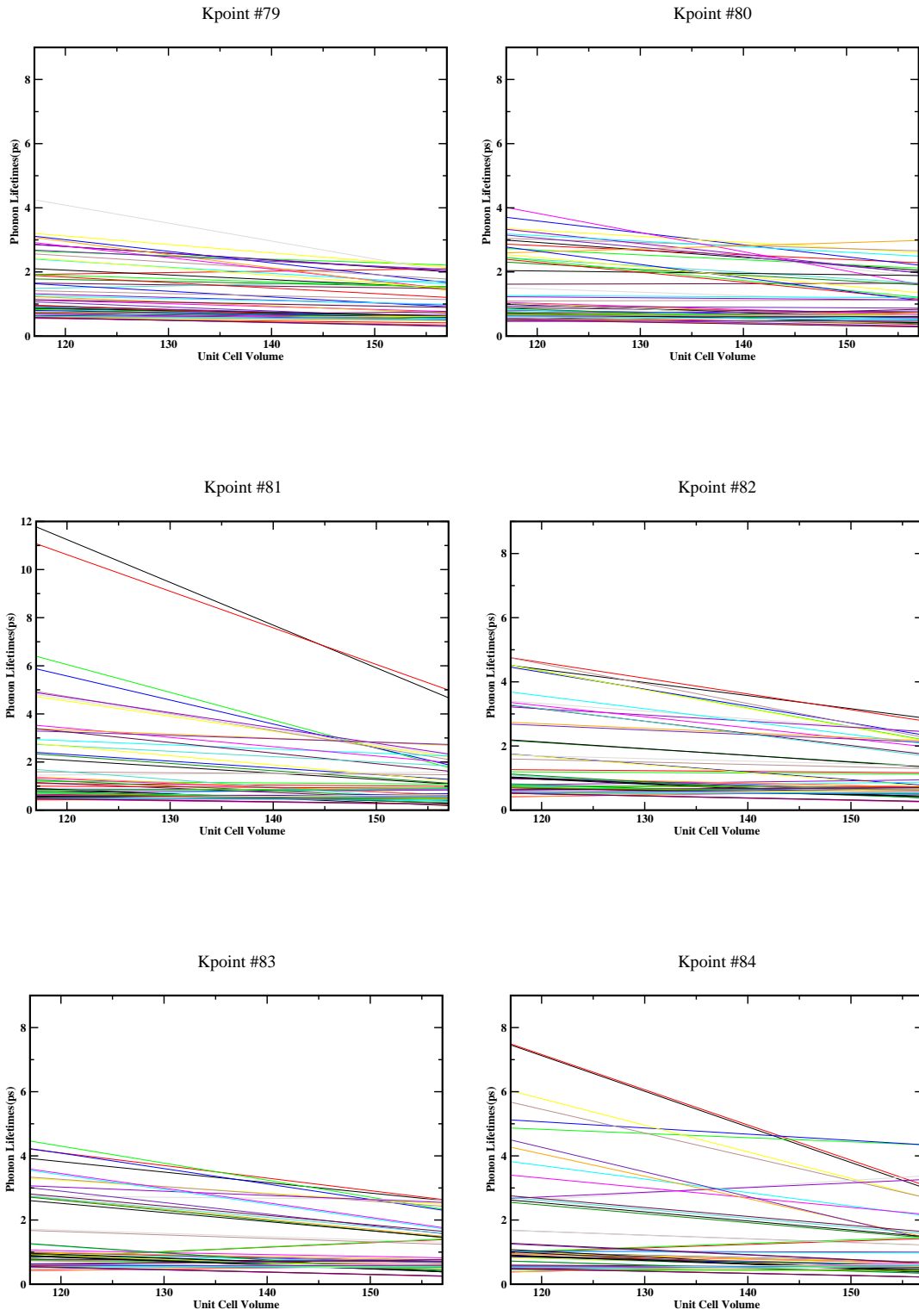


Figure E.14: Density dependence of phonon lifetimes for 60 phonon modes at irreducible K-points #79-84 in BZ

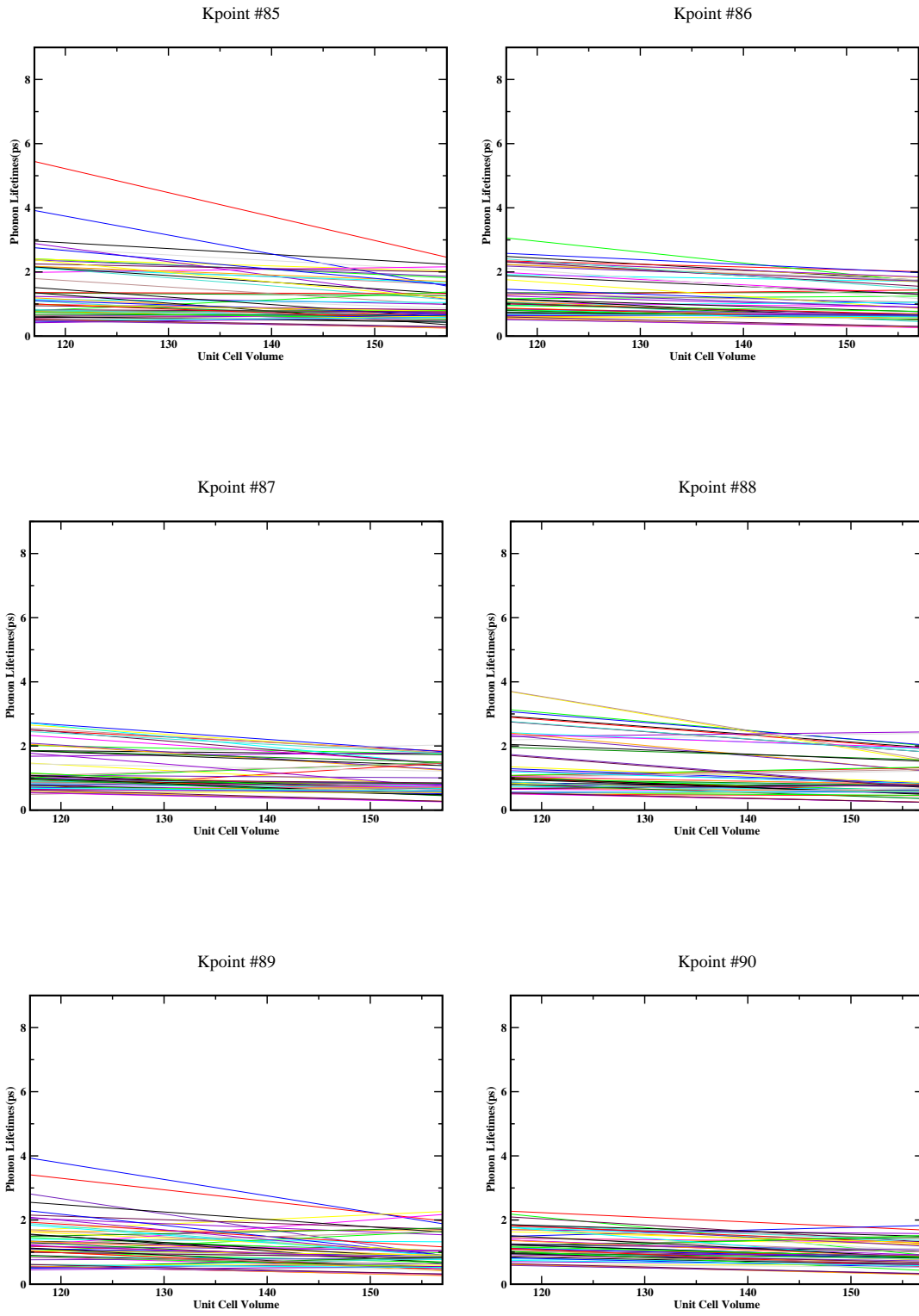


Figure E.15: Density dependence of phonon lifetimes for 60 phonon modes at irreducible K-points #85-90 in BZ

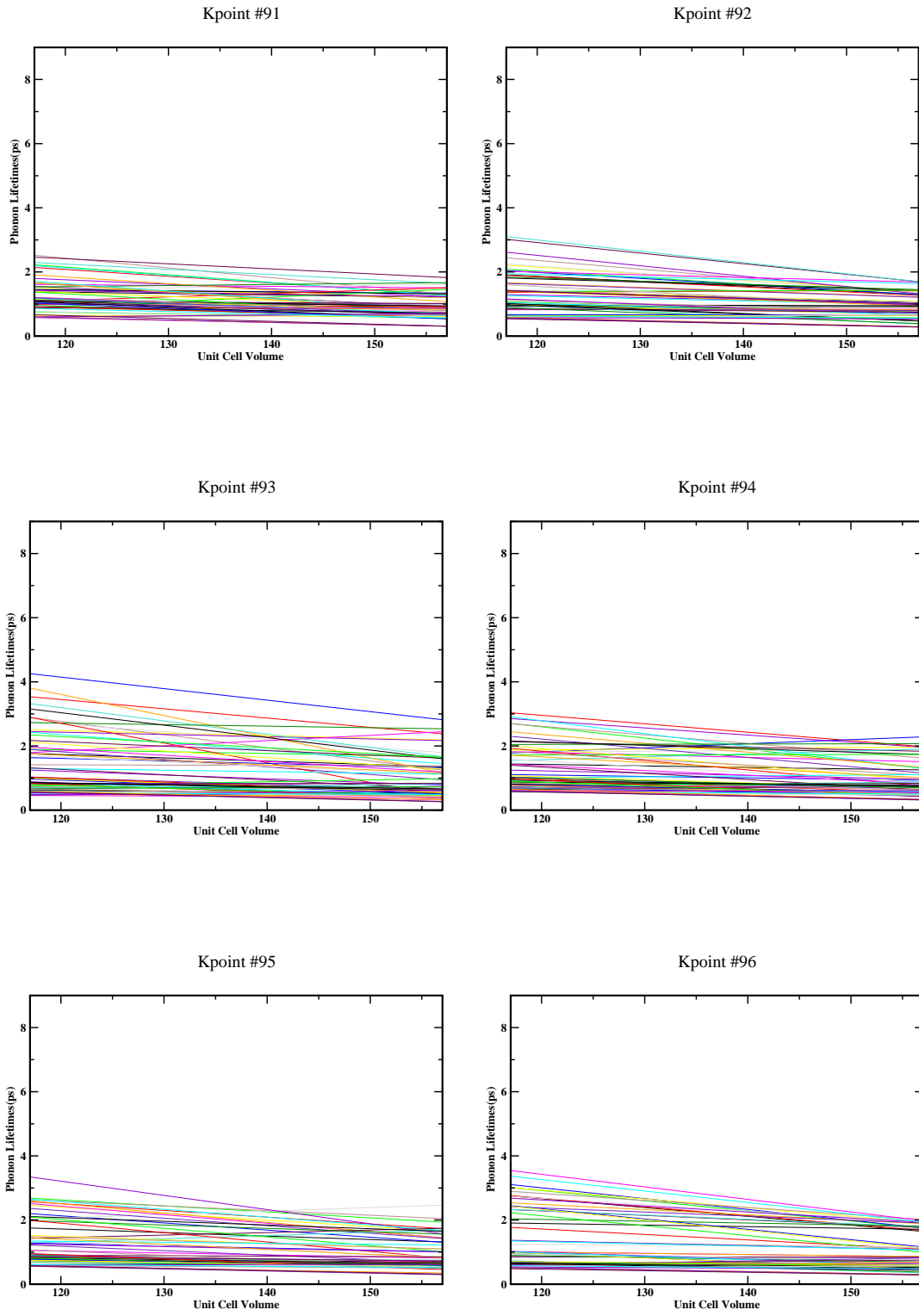


Figure E.16: Density dependence of phonon lifetimes for 60 phonon modes at irreducible K-points #91-96 in BZ

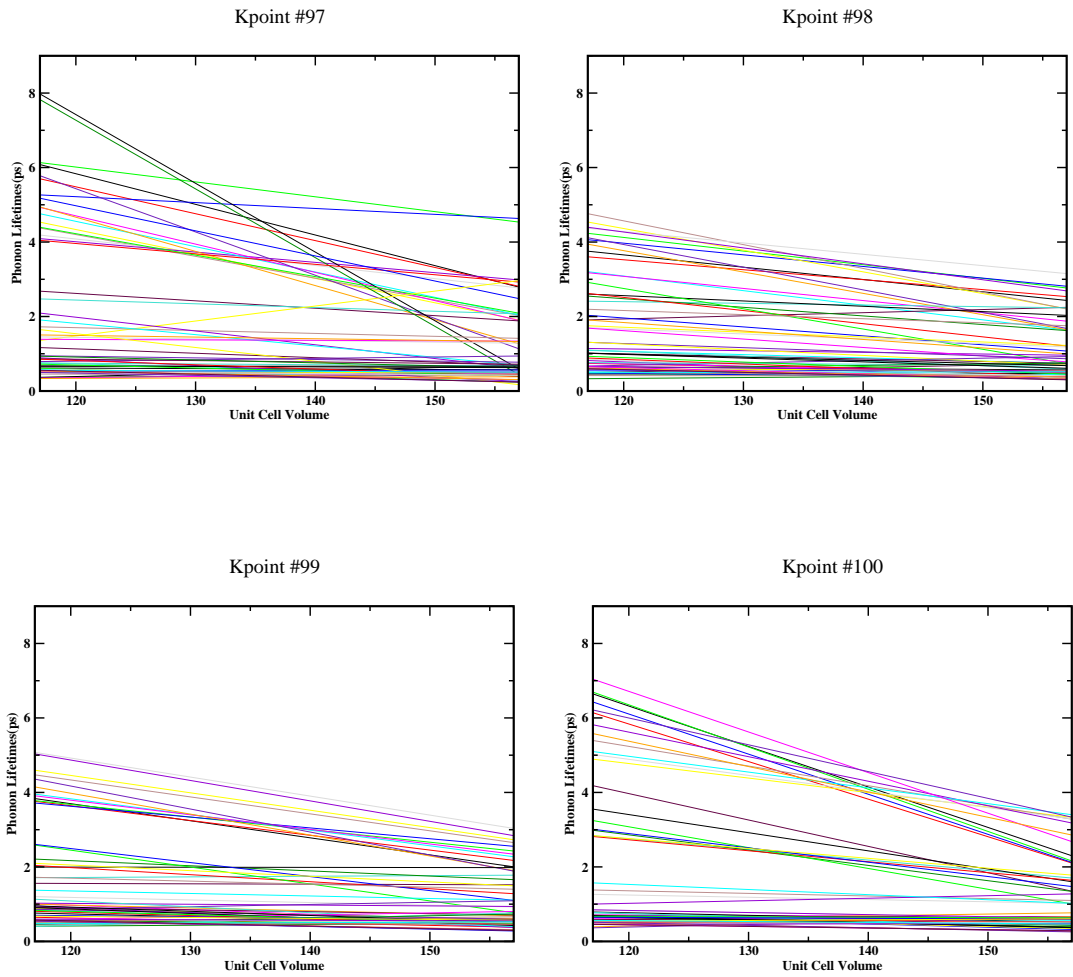


Figure E.17: Density dependence of phonon lifetimes for 60 phonon modes at irreducible K-points #97-100 in BZ